SECONDARY ION EMISSION UNDER KEV CARBON CLUSTER BOMBARDMENT

A Dissertation

by

JAY EDWARD LOCKLEAR

Submitted to the Office of Graduate Studies of
Texas A&M University
in partial fulfillment of the requirements for the degree of

DOCTOR OF PHILOSOPHY

August 2006

Major Subject: Chemistry

SECONDARY ION EMISSION UNDER KEV

CARBON CLUSTER BOMBARDMENT

A Dissertation

by

JAY EDWARD LOCKLEAR

Submitted to the Office of Graduate Studies of
Texas A&M University
in partial fulfillment of the requirements for the degree of

DOCTOR OF PHILOSOPHY

Approved by:

Chair of Committee,	Emile A. Schweikert
Committee Members,	D. Wayne Goodman
	Simon W. North
	Ron R. Hart
Head of Department,	Emile A. Schweikert

August 2006

Major Subject: Chemistry

ABSTRACT

Secondary Ion Emission Under keV Carbon Cluster Bombardment.

(August 2006)

Jay Edward Locklear, B.S., Southwestern Oklahoma State University

Chair of Advisory Committee: Dr. Emile A. Schweikert

Secondary ion mass spectrometry (SIMS) is a surface analysis technique capable of providing isotopic and molecular information. SIMS uses keV projectiles to impinge upon a sample resulting in secondary ion emission from nanometric dimensions. It is well documented that secondary ion emission is enhanced using cluster projectiles compared to atomic projectiles. Previous studies of enhanced secondary ion yields with cluster projectiles have led to the present study dealing with the scope of C_{60} as a projectile for SIMS.

The secondary ion yields (i.e., the number of secondary ions detected per projectile impact) from impacts of 10-26 keV $C_{24}H_{12}^{+}$, C_{60}^{+}, gramicidin S^{+} and $C_{60}F_{40}^{+}$ projectiles were examined to compare the effectiveness of the projectiles. The $[M-H]^{-}$ secondary ion yields from several organic samples varied inversely with the molecular weight. Multiple ion emission decreases monotonically as a function of the number of secondary ions emitted per impact and varies with impact energy such that higher energies produce more multiple ion emission.

The emission of CN^{-} from biological samples as a function of carbon-based projectile characteristics was examined to explore the possibility of using CN^{-} as a

molecular identifier. CN^- emission was found to be the product of both direct and recombination/rearrangement emission.

Re-emitted projectile atoms in the form F^- were found under $C_{60}F_{40}^+$ bombardment. Two forms of re-emitted F^- were found: One form in which F atoms retained a portion of the initial kinetic energy, and a second in which the F atoms deposited most of the initial kinetic energy into the surface before being ejected.

The $[M-H]^-$ secondary ion yield of gramicidin S was increased ~ 15 times by embedding the analyte in a matrix of sinapic acid.

These results show the optimum carbon based projectile for a given sample is dependent upon the signal to be monitored from the surface. The results also show CN^- has potential as a molecular identifier. Additionally, the detection of re-emitted F^- confirms prior predictions of re-emitted projectile atoms.

DEDICATION

To

my parents,

and

Amy, Doug, and Derek

ACKNOWLEDGEMENTS

During my years at Texas A&M University, I have been helped and encouraged by a number people whom I would like to recognize. My deepest gratitude to my advisor, Dr. Schweikert, whose patience during my graduate career is truly appreciated, especially since I know that I tested it on several occasions. I would also like to thank Dr. Stan Verkhoturov for his help with instrument building and data interpretation as well as an introduction into a larger world view of politics and religion. I would like to thank Dr. Christelle Guillermier, who came to my rescue with the final defense preparations and has shown me that a fiery passion for one's work is O.K. Thanks to Dr. Dennis James for keeping the computers up-to-date and house chilled water supply flowing. Thanks to Mike Raulerson for his office camaraderie and the political and sports conversations. Thanks to Charlene Helton, who time and again deciphered Dr. Schweikert's notes for me.

I would also like to thank Dr. Rick Rickman for his patience with me during those first experiments on System 4. I did in fact learn how to keep a CFD working more than a run or two. Thanks to George Hager for years of interesting moments. I never would have thought after being roommates at GVW that six years later we would be finishing graduate school from the same group. I will certainly not forget a night on the town in Manchester any time soon. Thanks to Sara Hager for her help with the proof reading. I wish you good luck keeping George in line in the coming years. Thanks to Zhen Li, who introduced me to many Chinese cultural experiences. I will continue to be

fascinated by your knowledge of computers and technology gismos as well as your ability to find the best deals on everything. I wish you continued success and good health. Thanks to Veronica Pennick for her help with proofreading and being a good sport with the intra-office conversations. To Marcus Sidhartharaja, good luck with graduate school, maybe things will smooth out as time progresses.

My final thanks go to those who have supported me on the home front. To Jeri Wilkerson, who has given her love, understanding and support through the ups and downs of graduate school. To my family, Charles, Jane Ann, Amy, Doug and Derek whose love and support have been the foundation for all my successes.

TABLE OF CONTENTS

CHAPTER Page

LIST OF FIGURES

FIGURE Page

FIGURE Page

FIGURE Page

FIGURE Page

LIST OF TABLES

CHAPTER I

INTRODUCTION

Surface analysis is critical to multiple fields of science and technology [1-3]. Among many surface analysis techniques, secondary ion mass spectrometry (SIMS) is one of the most versatile with a wide range of applications [4-8]. Briefly, the technique is based on the identification of ionized species ejected from a sample surface bombarded with keV to MeV atomic, polyatomic, or cluster ions (Fig. 1-1) [6, 9]. The signal (i.e., the secondary ions) is analyzed via mass spectrometry providing, in principle, a comprehensive analysis from isotopes to molecules. The volume analyzed is defined by the primary ion beam which can be confined or focused to generate secondary ions from a selected surface area. Positional and spatial control of the projectiles has led to the development of chemical imaging in the microscope or microprobe modes. Lateral resolutions in the sub-micrometer range have been achieved [10]. Depth resolution is set by the emission depth of the secondary ions which is < 5nm. The bombardment process erodes the sample surface. This feature can be exploited for depth profiling by applying primary ions doses in excess of 10^{12} ion/cm^2. The tri-dimensional analysis, referred to as dynamic SIMS has until recently been confined to the spatial correlations of isotopes because of the damage (surface roughening, mixing) caused by the atomic beam bombardment [11-13].

This dissertation follows the style and format of the International Journal of Mass Spectrometry.

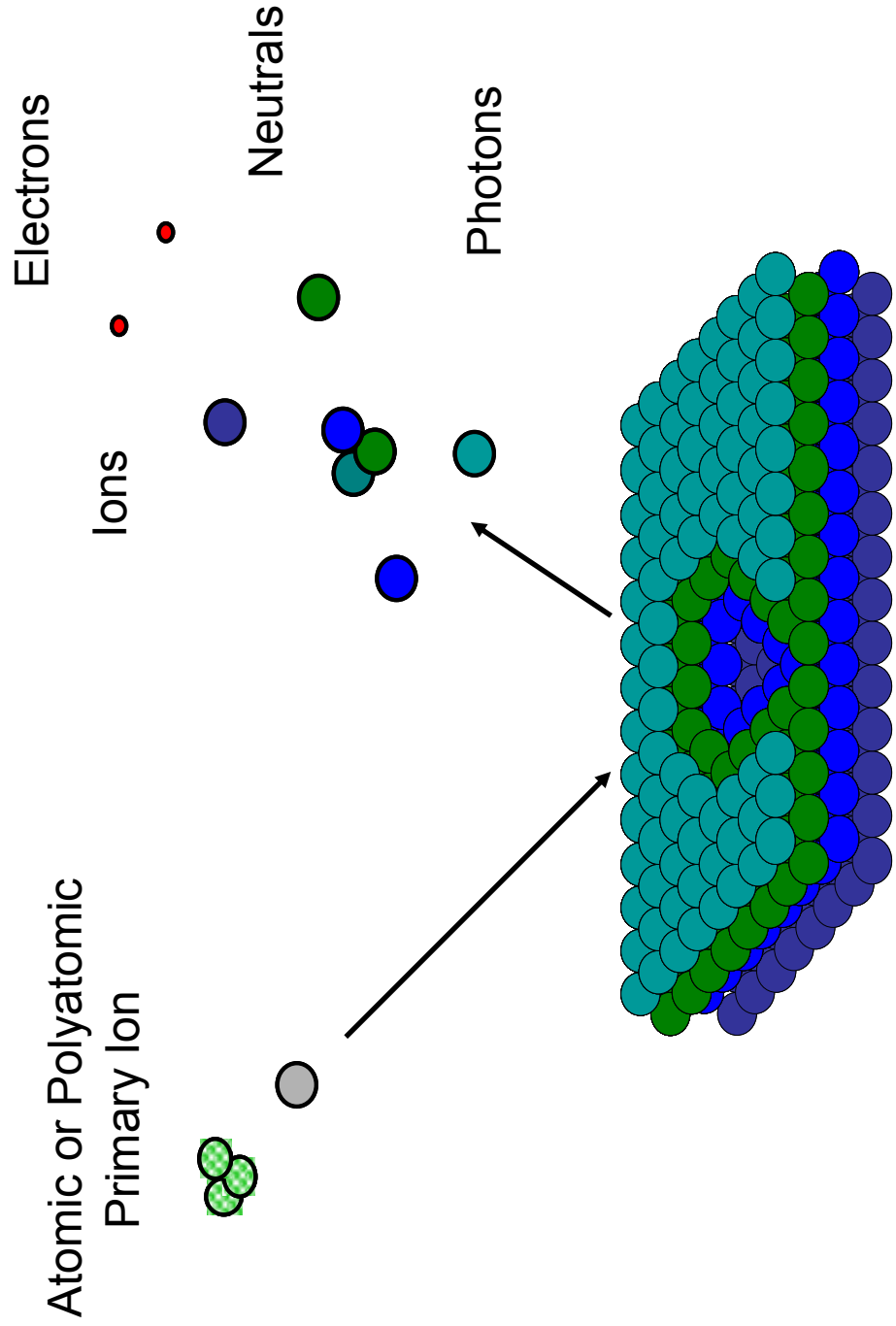

Fig. 1-1: Representation of a desorption event.

Most SIMS work is concerned with planer surface analysis and can be carried out with virtually no damage to the area probed by operating in the static mode. Static SIMS uses a primary ion dose of $<10^{12}$ ion/cm^2. Again, under these conditions, the likelihood of a projectile impacting a damaged area of the sample is small. Secondary ion emission is thought to evolve from a region of the surface ~10 nm in diameter and < 5 nm in depth [14].

The usefulness of the SIMS technique for analysis is determined by the accuracy of the secondary ion signal and the detection limit. Atomic projectiles such as Ga^+, Cs^+, O^+, and Ar^+ produce secondary ion yields in the range of a few hundredths of a percent to a few percent [10]. In order to increase the effectiveness of SIMS, various avenues have been pursued in recent years to enhance the signal, including post-ionization of neutral ejecta, the use of cluster projectiles, and sample preparation techniques.

Post-ionization has been extensively studied [15-18]. Two approaches have been pursued, ionization of a selected atomic or molecular species or nonresonant ionization. The first methodology has been pushed to the limits of selective detection of very small numbers of atoms using resonant ionization schemes. The intrinsic advantage of a "decision limit" of a few atoms is also a limitation in that the analysis is solely for a pre-selected atomic species [16, 17, 19]. The nonresonant scheme, not tailored to the ionization of a specific atom or molecule, has been of limited analytical usefulness due to molecular dissociation inherent with the use of intense photon or electron beams [16, 17].

A breakthrough in obtaining enhanced SI emission occurred with the replacement of atomic projectiles with polyatomic projectiles [20]. For example, the SI yield of the molecular ion of phenylalanine is increased by a factor of 30 when replacing Au^+ with Au_3^+ of equal velocity [20]. The effect is non-linear and increases with the number of constituents in the cluster projectile. These earlier studies led to the present one dealing with the scope of C_{60} as a projectile for SIMS. C_{60} has numerous advantages as a cluster projectile. It has a well characterized and stable structure, its impact geometry is always the same, and it sublimes easily which simplifies the design of a projectile source. The attractive features of C_{60} as a projectile have been recognized by others and documented in recent publications [21-32]

A third approach to the enhancement of secondary ion signal involves sample preparation. Improvements in detection sensitivity have been obtained by encasing an analyte in a chemical environment which promotes ionization (substrate, surface metallization, and matrix) [33-44]. These attempts have been limited to SIMS with atomic projectiles. We have examined, in the present study, the usefulness of analyte dissolution in a matrix in conjunction with the use of large carbon-based projectiles.

A distinctive trait of our experimental approach is the event-by-event bombardment and detection sequence. As the efficiency of the bombarding projectile increases, the number of projectiles can be decreased. In our case, we decreased the frequency of impacts to the level where secondary ion emission from single impacts can be detected and recorded. Our data show that at the rate of ~1000 projectiles per second, we can obtain statistical valid results in ~1000 seconds, given the efficient production of

secondary ions from large carbon cluster impacts. There is an important feature in the event-by-event bombardment and detection method: It allows the recording of secondary ions emitted from single ion impacts i.e., from an emission site of nanometric dimensions. If the same spatial resolution of co-emitted secondary ions occurs in a repeated number of spots probed, we have in fact a test revealing surface micro-homogeneity [45]. This concept has been demonstrated in a series of papers describing "Coincidence Counting Mass Spectrometry" [46-49]. Implicit in Coincidence Counting Mass Spectrometry (CC-MS) is the requirement of multiple secondary ion emission from single impacts. Multiple secondary ion emission was found to increase with projectile size and energy in the case of Au_n^m (n = 1-4, m = 1-2) [49].

These observations prompt several questions. Do carbon cluster projectiles produce multiple ion emission, and if so, is there a relationship between the multiple ion emission and the projectile characteristics as was observed with Au_n^m (n = 1-4, m = 1-2)? Can this multiple ion emission be used to gain further understanding of the emission process?

To address these issues, this study focused on the following objectives:

(i) build a ToF mass spectrometer with a carbon cluster ion source. The source was to be capable of producing a variety of cluster ions and selecting a given cluster ion for subsequent use. The experiments were carried out using C_{60}^+ projectiles as well as two additional carbon projectiles, coronene ($C_{24}H_{12}^+$) and $C_{60}F_{40}^+$, which were used as comparative tools. This instrument was to operate within the event-by-event bombardment and detection protocol, which allows CC-MS to be used. Additionally,

the instrument was to be capable of measuring multiple ions of the same mass-to-charge from a single projectile impact.

(ii) characterize multiple ion emission as a function of the carbon-based cluster projectile parameters. Two aspect of multiple ion emission were examined: trends of multiple ion emission for all secondary ions and trends of multiple ion emission for sample specific ions.

(ii) characterize parameters affecting CN^- emission under cluster projectile bombardment with the purpose of using CN^- for molecular recognition.

(iii) examine the fate of the projectile constituent atoms for carbon-based cluster projectiles as it has been theorized and experimentally shown that constituent atoms from cluster projectiles are reflected back into the vacuum [50-53].

(iv) examine matrix enhancement as a means to increase the secondary ion yields of a labile species under cluster bombardment and gain insight into possible emission mechanisms for this system using CC-MS, since previous studies have shown increases in secondary ion yields under atomic bombardment using matrices [33, 35-44].

CHAPTER II

CLUSTER PROJECTILE BOMBARDMENT:

A BRIEF SUMMATION

The purpose of this summation is to review briefly Secondary Ion Mass Spectrometry (SIMS) as it pertains to this study. Specifically, the use of cluster projectiles for surface bombardment, theories of ion-induced sputtering, molecular dynamics simulations and secondary ion multiplicity are discussed.

Cluster Projectile Bombardment

The first reports using polyatomic (i.e., cluster) projectiles date to the 1960's. Two groups observed similar trends with cluster projectiles. Rol, et al. observed the sputtering yields from a polycrystalline copper produced by KI^+ impacts was higher than the sum of the sputtering yields produced by K^+ and I^+ on the same surface [54]. Grønlung, et al. found the sputtering yields from a silver surface produced by H_3^+ was consistently higher than 3 times the sputter yield produced by H^+ [55]. These studies were the first to suggest a non-linear effect with cluster projectiles. Further investigations with clusters continued with a primary interest in fundamental emission processes [56-58].

In 1987 Appelhans, et al. built a $SF_6^{0,-}$ cluster source for the examination of insulating materials (i.e., Mylar, Teflon®, etc.) demonstrating cluster bombardment for a specific application [59]. The $SF_6^{-,0}$ beam was shown to produce 3 to 4 orders of magnitude increase in SI yield intensity compared to atomic beams. An ensuing study

compared Cs^+ to $SF_6^{-,0}$ on the pharmaceutical compounds: acetaminophen, codeine, dopamine and a mixture of acetaminophen and codeine. The molecular ion intensities using $SF_6^{-,0}$ compared to Cs^+ increased 9-24 times depending on the compound [60].

Groups at Texas A&M and Institute de Physique Nucleaire at Orsay, France, began investigations into SI emission phenomenon with cluster projectiles beginning in the late 1980's and continuing to the present. The initial study examined cluster projectiles of $(CsI)_nCs$ (n = 0-2), coronene ($C_{24}H_{12}$) and phenylalanine ($C_9H_{12}NO_2$) with 5-28 keV of energy on various samples including phenylalanine, CsI, and Au [20]. They observed supralinear enhancement on phenylalanine, CsI, and Au surfaces. Enhancement (ε) for a homonuclear projectile A_n having n constituents was defined as

$$\frac{Y_{An}(E)}{nY_A(E/n)} \geq \varepsilon$$

where $Y_{An}(E)$ is the yield of ejected atoms or ions for the cluster at energy, E, and $Y_A(E/n)$ is the yield for the constituent atom at equal velocity. Values of ε greater than one are considered supralinear enhancement. In this study, enhancements of up to 50 were observed. Within the energy regime examined, the SI yields were proportional to the square of the projectile momentum.

In 1991, Benguerba, et al. extended the study to include Au_n^m (n = 1-5, m = 1-2) projectiles. This study found that the parameter which most affects SI yield is the number of constituents in the projectile. SI enhancement occurred on CsI and Au surfaces using carbon-based, $(CsI)_nCs^+$ (n = 0-2), and Au_n^m (n = 1-5, m = 1-2) projectiles. A saturation effect was observed with carbon-based projectiles on

phenylalanine. The authors suggested that once a cluster reached a certain size (i.e., number of constituents > 7) the ”cluster effect” would level off, but linear increases in SI yield could still be obtained with more constituents [61].

Boussofiane-Baudin, et al. observed a similar trend with 5-30 keV coronene, C_{37}^+, C_{60}^+, and C_{70}^+ on a phenylalanine surface [62]. A second component of the study compared the influence of projectile complexity (i.e., number of constituent atoms in a cluster) on SI yields. The phenylalanine SI yield was found to be higher when bombarded by more complex projectiles at equal velocities (e.g., C_{60}^+ (720 amu) produced higher SI yields compared to Au_4^+ (788 amu)).

Szymczak, et al. examined the SI emission of $(CsCl)_nCs^+$ (n = 0-10) using 24-31 keV Ne^+, Ar^+, Xe^+, F^-, and SF_6^- projectiles [63]. SI yields increased with increased atomic projectile mass. Additionally, the SI yields of $(CsCl)_nCs^+$ (n <3) were enhanced up to a factor of 6 by using SF_6^- compared to Xe^+.

The Texas A&M group conducted a series of experiments evaluating atomic and cluster projectiles (C_{60}^+, $(CsI)_nCs^+$ (n = 0-2), and Ga^+) for surface analysis purposes [64]. These studies suggested that cluster projectiles produced enhancement compared to atomic projectiles. These studies also showed that clusters produce more signal that is not directly representative of the sample (i.e., fragmentation [65] and rearrangement [66]) compared to atomic projectiles.

The Texas A&M group conducted experiments to evaluate the efficiency of atomic and cluster projectiles (C_{60}^+, $(CsI)_nCs^+$ (n = 0-2), $(NaF)_nNa^+$ (n = 0-2) and SiF_5^-) on organic surfaces of an organic acid, phospholipids and alkyl sulfates prepared as

multilayer or monolayer samples [65]. The optimum projectile was found to vary based on the compound as well as the sample thickness. Generally, cluster projectiles increased the secondary ion yields from multilayer samples >10^1 compared to atomic projectiles, while cluster projectiles increased secondary ion yields on the monolayer samples 2-3 times compared to atomic projectiles.

In 1998, Gillen, et al. compared the SF_5^+ bombardment to Ar^+ bombardment on a variety of thin organic films [11]. This study produced several points of interest. Signal enhancements of 10-50 times were observed with SF_5^+ compared to Ar^+ with one exception. An enhancement of ~2 was found on a self assembled monolayer. An increase in non-specific chemical noise under cluster bombardment was observed. The study also examined the possibility of molecular depth profiling using cluster projectiles. In thin films of glutamate, t-butyl ammonium bromide, acetylcholine, and poly methyl-methacrylate (PMMA) on Si wafers, stable molecular ion signals were observed as the depth profile progressed using SF_5^+ while molecular ion signals degraded rapidly with Ar^+ bombardment. It was proposed that SF_5^+ sputtered away any damage produced upon impact in these samples. The study demonstrated the possibility of using cluster projectiles for imaging purposes.

The Texas A&M group conducted a series of studies examining self-assembled monolayers (SAM). SAM surfaces are produced by exposing thiol species to a gold surface. There is a spontaneous reaction between the sulfur and Au resulting in a covalent bond, which produces an organized monolayer on the Au surface. The initial study examined the SI yields from SAM surfaces using $(CsI)_nCs^+$ (n = 0-2),

$(Bi_2O_3)_nBiO^+$ (n = 1, 2), and C_{60}^+ [67]. It was observed that the SI yield of the monolayer species increase by 2-3 times when bombarded by polyatomic versus atomic projectiles, which was observed previously [11].

Subsequent studies focused on using SAM surface as modified surfaces to improve the SI yields of liable molecules. Aminoethanethiol (AET) SAMs were used as anion-exchangers for BF_4^- and $B(Ph)_4^-$. The SI yields from the exchanged samples and from thick targets using 10-26 keV $(CsI)_nCs^+$ (n = 0-2) projectiles. The thick targets exhibited supralinear yield enhancements while the exchanged layers increased by 2-3 times [68]. Further experiments examined SI yields of organic ions (e.g., tetradecylsulfate, cholesterol-3-sulfate, etc.) from AET layers and thick targets [69, 70]. Observations were similar to those seen before: thick targets exhibited supralinear yield enhancements with cluster projectiles while the SI yield of the AET layers increased by 2-3 times. However, in this case the SI yields from the AET SAMs were up to 100 times higher than SI yields from the thick targets.

In 2001, Gillen, et al. developed a negative cesium sputter ion source to generate cluster ion beams [71]. The beam primary ions of C_n^- (n = 1-10) and C_nCs^- (n = 4, 6, 8). Picoampere intensities were reported for the primary ion beams. Non-linear SI yield enhancement on organic targets was found to increase from C_1^- to C_5^- reaching saturation at C_6^- to C_{10}^- (note: non-linear SI yield enhancement was defined at equal kinetic energies; therefore, the primary ion velocity was not considered). Molecular depth profiling was attempted with the carbon projectiles with mixed results. Molecular depth profiling using C_6^- to C_{10}^- was possible on many of the thin films seen in the 1998 study,

but molecular signal degraded more quickly as the size of the projectile decreased (i.e., C_5^- to C_1^-).

In 2003, Vickerman and co-workers introduced a C_{60} primary ion source [72]. The source produced C_{60}^m (m = 1-2) up to 25 keV of energy, nanoampere beam intensities, and ~3 μm lateral resolution. The C_{60} source provided increased SI yields compared to atomic projectiles, in some case up to 10^3 increases.

2003 to present, Winograd and co-workers have used a C_{60} source to carry out experiments focusing on depth profiling and imaging. Depth profiling was achieved on PMMA [12], Langmuir-Blodgett films [22-23], NiCr multilayers [24], water-ice films [25-26], and treholose films [13]. The depth resolution in these studies was found to be equal to or better than those achieved with atomic projectiles. Imaging experiments on materials such as Cu [27], Teflon® [27], polypeptides [28], biological cells [29], and lipids [30] all show 10^1 to 10^3 increases in SI intensity using C_{60} projectiles compared to atomic projectiles.

A group of cluster projectiles much larger than those discussed thus far have also been produced and will be referred to as massive clusters. Mahoney, et al. produced a range of massive glycerol clusters (amu $>10^7$, q > 100) using an electrohydrodynamical source. Massive glycerol projectiles were found to produce lower chemical noise and enhance signal-to-noise ratios [73-74]. Massive projectiles of peptides and proteins (amu = 1.1-66 kdal, z = 1-60) have been produced using an electrospray ion source [75]. Studies conducted with this source have examined secondary ion multiplicity [75], secondary electron emission [76] and gas phase structure and stability of the massive

projectiles based on the shape of the impact craters produced [77]. Yamada and co-workers have produced massive clusters of Ar_n^+ (n = 1-5000). Massive Ar projectiles produce up to 10^2 increases in sputtering yields compared to atomic Ar projectiles [78]. Bouneau, et al. have produced massive gold clusters via a liquid metal ion source [79-81]. Massive gold clusters have increased SI intensities up to 10^3 compared to atomic Au and improved signal-to-noise up to 20 times.

Theories of Sputtering

Sigmund introduced a theoretical model to explain ion induced sputtering in 1969 [82]. In this model, kiloelectron volt atomic particles interact with atoms in the substrate via elastic collisions. These atoms in turn collide with other substrate atoms. In the event that a collision directs a substrate atom toward the surface, the atom can escape if it possesses a kinetic energy greater than the surface binding energy. This model described the sputtering SI emission produced by low mass primary ions. However, significant deviation occurred with higher mass projectiles (e.g., Xe^+ and Hg^+).

In 1974, Andersen and Bay carried out experiments using Te, Se, and Cl projectiles. To examine differences in sputtering yields, the sputtering yields of Te_2^+, Se_2^+, and Cl_2^+ were compared to sputtering yields of Te^+, Se^+, and Cl^+ projectiles at equal energies per atom. Enhancements produced by the diatomic projectile compared to the atomic projectile (i.e., Te_2^+ to Te^+, Se_2^+ to Se^+, and Cl_2^+ to Cl^+) were 1.67, 1.44, and 1.09 respectively on a Ag target [56-57]. The authors explained this increase in sputter yield with a thermal spike model in which areas of overlapping collision cascades

with a high energy density cause additional sputtering of the surface (i.e., localized evaporation of the surface) [56-57]. Sigmund then developed a model using collisional cascade theory to predict the necessary conditions to produce a thermal spike [83-84].

Johar and Thompson examined the sputter yields of Ag, Au, and Pt by atomic and polyatomic ions of P, As, Sb, and Bi with energies of 10-250 keV. Enhancements were again observed using polyatomic projectiles. The result conflicted with the Sigmund thermal spike model, which predicted negligible enhancement for these targets. Therefore, a collisional spike model was proposed in which a highly disrupted surface region resulting from a projectile impact reduces the surface binding energy thereby causing higher sputter yields [58]

Bitensky and Parilis proposed a shockwave model to describe the emission of large intact molecules under cluster bombardment. In this model, sputtering occurred in two parts: a collisional spike which sputtered atoms and small fragments, and a collisional spike induced shockwave which sputters intact molecules from the surface at points where the shockwave intersects the surface [85].

The shockwave model more closely reflects the conditions expected under keV carbon cluster bombardment since it addresses clusters containing large numbers of low mass constituents. However, each model describes only the sputtering of neutral species from surfaces and can not address the ionization process.

Molecular Dynamics Simulations

Molecular dynamics (MD) simulations are computer models based on the above theories that show the evolution of a desorption event in time. MD simulations have

improved over time incorporating larger, higher energy systems as well as more complex particle-particle interaction scenarios [14, 86-89]. However at this time, MD simulations can not produce models of ionized species. Even with this limitation, MD simulations can offer insight into the desorption process.

In 1998, Zaric, et al. simulated Cu_n (n = 1-4) projectile impacting a Cu surface with a biphenyl overlayer at 50-100 eV. The simulations showed a higher number of biphenyl molecules ejected with higher energy more complex projectiles (i.e., a cluster effect) [86].

Postawa, et al. simulated 15 keV Ga and C_{60} on Ag {111} surface [14]. The simulations showed the C_{60} sputter yield to be ~10 times higher than Ga. C_{60} was found to have equivalent impacts (i.e., each impact sputtered approximately the same amount of material from the surface), while Ga did not produce equivalent impacts. This was explained based on the sizes of the respective projectiles. Ga (diameter 1.3 Å) can penetrate deep into the Ag surface before any interactions result in energy deposition thereby leaving a small amount energy in the surface region to cause sputtering, while C_{60} (diameter ~0.7 nm) interactions occurred at the first layer of Ag causing the majority of the energy to be deposited in the surface region causing greater sputtering. The simulations also suggested that ~53 of the 60 carbon atom introduced to the surface by the C_{60} impact would be self-sputtered. In a subsequent study, additional parameters such as impact energy and impact angle were examined [31]. The sputter yield with C_{60} was found to be linearly dependent upon the impact energy (5-20 keV), and sputter yields with C_{60} were found to have little dependence on impact angle from $0\text{-}30^0$.

However, beyond 30^0 significant sputter yield decreases were observed. This decrease was explained by decreased energy deposition in the surface at oblique angles.

Aoki and co-workers simulated 1.2 – 120 keV C_{60} impacts on diamond surfaces. They found increased penetration of the surface as the energy per carbon atom increased [32].

Webb, et al. simulated impacts of 0.1- 20 keV C_{60}, C_{100} and C_{300} on graphite surfaces [87-88]. The simulations showed that projectiles of equal momentum per atom penetrate surfaces to the same depth (i.e., equal velocity C_{60} and C_{100} penetrate to the same depth). Additionally, increased fragmentation of a benzene overlayer occurred with 0.5 keV C_{300} compared to 0.1 keV C_{60}.

A review of MD simulations is available covering a range of projectiles and samples [89]. Similarities in trends have been observed between experiments measuring secondary ions and MD simulations for neutral species.

Secondary Ion Multiplicity

Secondary ion multiplicity is defined as the emission of multiple secondary ions from a single projectile impact. In literature, the secondary ions may be of the same or different masses. Increased secondary ion multiplicity can be useful in SIMS analysis. An increase in multiple ion emission from single ion impacts should result in an increase in analytically significant ion emission from the surface. Previous studies have shown that co-emitted ions can be used to determine surface homogeneity [45], chemical species associations on surfaces [46-49, 90] as well as provide information about fundamental emission processes [49].

Cluster projectiles have been shown to increase SI multiplicity. Zubarev, et al. measured the multiplicity (in this case defined as the number of secondary ions with different masses detected per impact) produced from a variety of biomolecules projectiles over a range of impact energies. It was found that the multiplicity increase with projectile mass when compared at equal velocities [75].

Rickman and co-workers conducted a series of experiments using keV Au_n^m (n = 1-4, m = 1-2) to examine multiple ion emission [49]. The initial experiment examined a specific type of SI multiplicity, the co-emission of two molecular ions of phenylalanine from single ion impacts. The experiment used a specialized surface to recognize two molecular ions. The surface consisted of 50% phenylalanine and 50% D_8-phenylalanine homogeneous mixture. The mass difference in the molecular ions provided sufficient flight time difference for both ions to be detected in a time-of-flight pulse counting configuration. The study showed yield enhancement of two co-emitted molecular ions with increasing projectile complexity. The study also suggested the fundamental mechanisms for SI production differ between atomic and cluster projectiles. In subsequent studies, the instrument was modified to include an 8 anode SI detector [91-92]. This allowed the detection of up to 8 ions of the same mass-to-charge ratio from a single ion impact and removed the necessity for a specialized surface to recognize multiple co-emitted ions of the same mass-to-charge ratio. These studies were carried out with 26-134.6 keV Au_3^+, Au_9^+, Au_{400}^{4+} bombardment of phenylalanine and $(HfO_2)_{0.6}(SiO_2)_{0.4}$ surfaces [91-92]. In general, the studies found that larger projectiles and higher energies increased multiple ion emission.

CHAPTER III

INSTRUMENTATION AND ELECTRONICS

The following chapter describes the two instruments and electronics with which the data described in Chapters IV-VIII were taken. Each instrument consists of two time-of-flight (ToF) regions: a primary ion ToF region and a secondary ion ToF region. Each instrument (^{252}Cf based source and effusion based source) has advantages and disadvantages with respect to the other. The ^{252}Cf based source is capable of producing a variety of projectiles (i.e., Cs, C_{60}, gramicidin S, bradikinin, etc.), but the throughput of the instrument is dependent on a radioactive source which has a half-life of ~2.65 years (i.e., decreased throughput with the evolution of time). The effusion based source produces projectiles from materials that can be sublimed and ionized intact in vacuum. A small percentage of the sublimed vapor is ionized and used as projectiles leaving the remaining vapor to be evacuated through the pumping system or to condensate on the cooler areas of the source region (i.e., electrostatic lenses, insulators, etc.). Over time, this condensation causes the failure of the insulators, which then requires instrument shutdown and cleaning.

^{252}Cf Mass Spectrometer

The ^{252}Cf based ToF instrument (Fig. 3-1) was used to conduct the experiments in chapter IV [64-65]. Primary ions are produced from a sputtering source using ^{252}Cf fission fragments. ^{252}Cf decays via spontaneous fission and alpha particle emission with MeV fission fragments accounting for approximately three percent of the activity. The

fission fragments are emitted about 180 degrees from each other with a distribution of masses (95-160 amu) and charge states (18-22) [93-94]. One fission fragment starts the timing electronics by passing through a negatively biased conversion foil. The conversion foil serves two purposes: production of electrons to impact a microchannel plate (MCP) assembly, and act as a barrier to the alpha particles to reduce false starts. The complementary fragment causes desorption/ionization of a source material coating an aluminized Mylar foil. The desorbed ions are used as primary ions for SIMS. The primary ions are accelerated in two steps up to a maximum of 21 keV. First, 3.5 – 14.5 keV primary ions separate in a ~14 cm primary ToF region. The positively charged primary ions are accelerated a second time as they approach a sample target biased at – 6.5 kV at 30^{o} from normal. Once a primary ion impacts the surface, secondary electrons and ions are ejected and accelerated through a second ~48 cm ToF region. The secondary electrons are steered to a second MCP assembly by a weak magnetic field (< 150 gauss) to signal the impact of a primary ion. Finally, any secondary ions produced by primary ion impacts are detected on a third MCP assembly.

The activity ^{252}Cf source (Isotope Products, Burbank, Ca) was 25 μCi at the time of purchase (January 1996). ^{252}Cf has a half life of ~2.65 years which rendered a useable activity of ~200 fission fragments per second at the time of the experiments. All primary ions made by a fission fragment on the source foil impact the sample surface at different times based on the m/z of the primary ion. For example, a fission fragment produces a C_{60}^{+} ion and the complementary fission fragment starts the electronics. Secondary electrons signal (Stop 1) the arrival of C_{60}^{+} at the sample target as well as the beginning

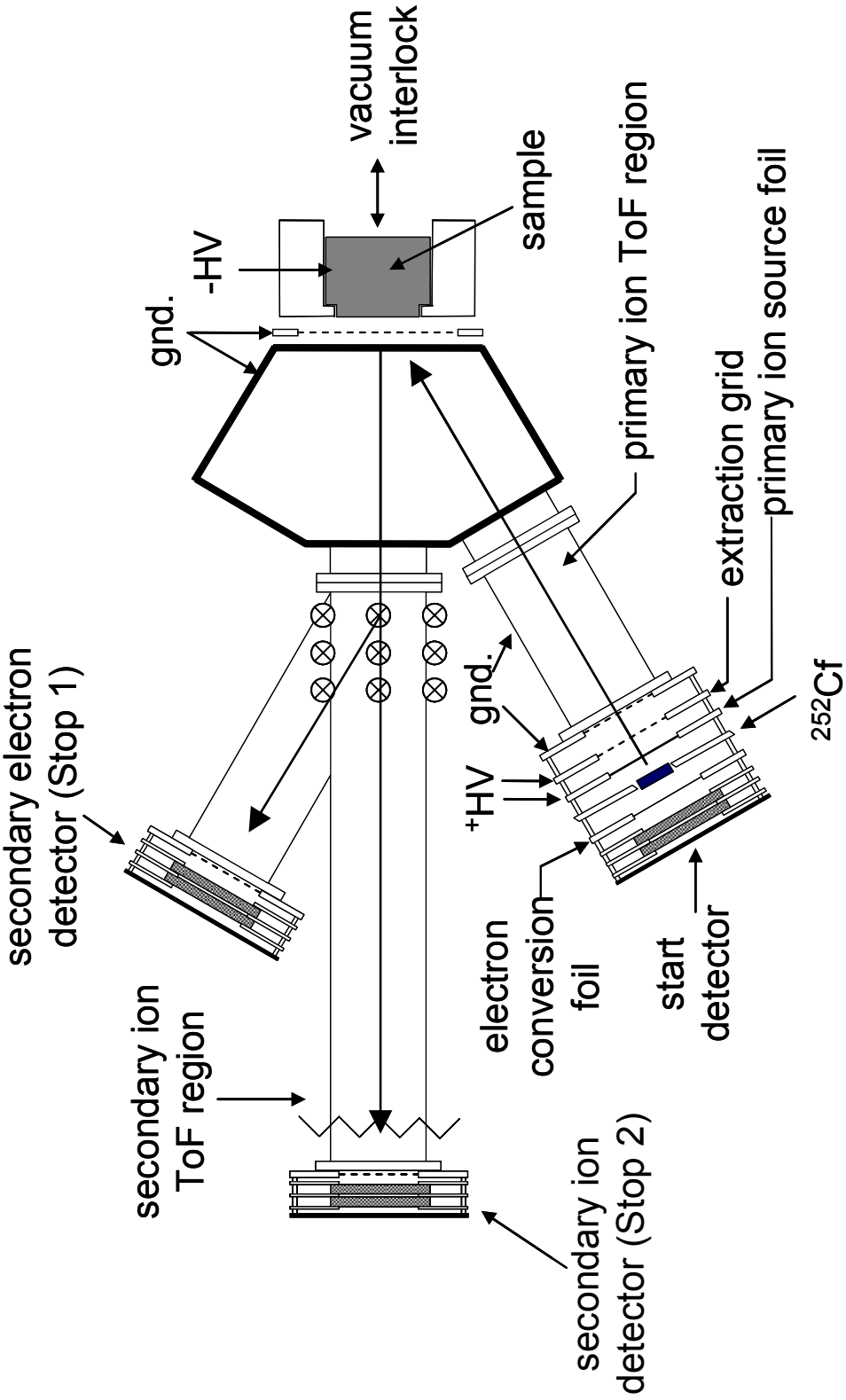

Figure 3-1: Schematic of ^{252}Cf source time-of-flight mass spectrometer (not to scale).

of the secondary ToF stage. Any secondary ions originating from the impact are detected (Stop 2). In instances where both secondary electrons and ions are detected from an impact a SI spectrum can be made. This spectrum is the sum of all primary ions impacting the sample (Fig. 3-2). A window is set around the C_{60}^+ peak in the primary ion spectra yielding a secondary ion spectrum produced by C_{60}^+ projectiles. The secondary ion spectrum is convoluted due to the impact angle, coupled with a large impact area (~2 cm^2) which produces a time aberration in the arrival time of C_{60}^+. A software function compensates for the time aberration by electronically shifting the arrival times of the primary ions in a selected window to the first channel in the window. The secondary ions associated with each primary ion event are shifted an equal number of channels yielding a secondary ion mass spectrum (seen in the figure on page 50). Coincidental (co-emitted) ions are observed by setting a window around an ion of interest in the secondary ion spectrum (seen in the figure on page 50).

Effusion Source Mass Spectrometer

Primary Ion Region

The primary ion region of this instrument is contained within a custom designed stainless vacuum chamber. The operational vacuum of ~$5x10^{-6}$ torr is maintained by a 60 l/s turbo pump (Pfeiffer Vacuum, Inc.) backed by a 20.5 m^3/hr rotary vain pump (BOC Edwards).

The effusion source mass spectrometer (Fig. 3-3) was used to conduct the experiments described in Chapters V-VIII. Figure 3-4 shows a schematic of the source

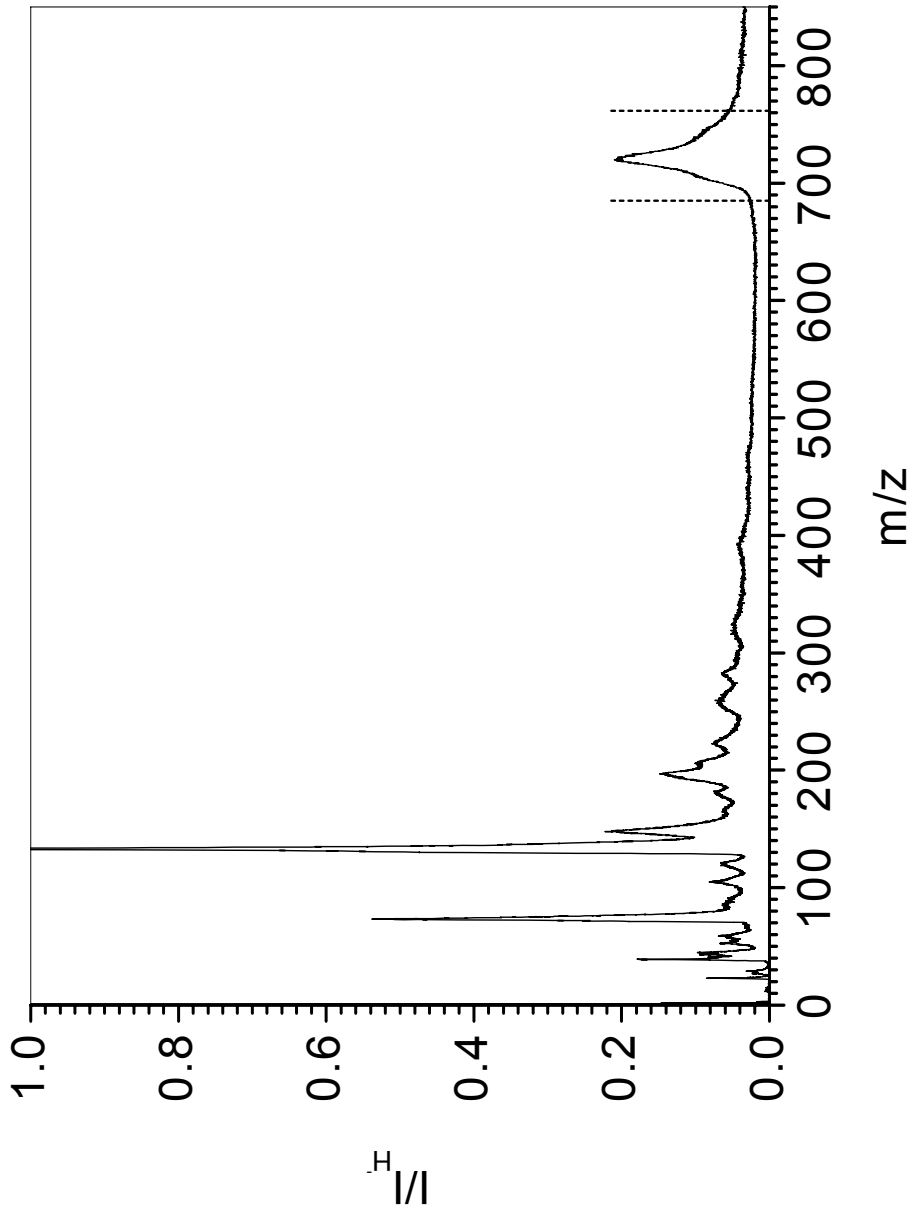

Figure 3-2: Primary ion spectrum of C_{60}^{+} caused by ^{252}Cf fission fragments (dashed lines identify the primary ion window).

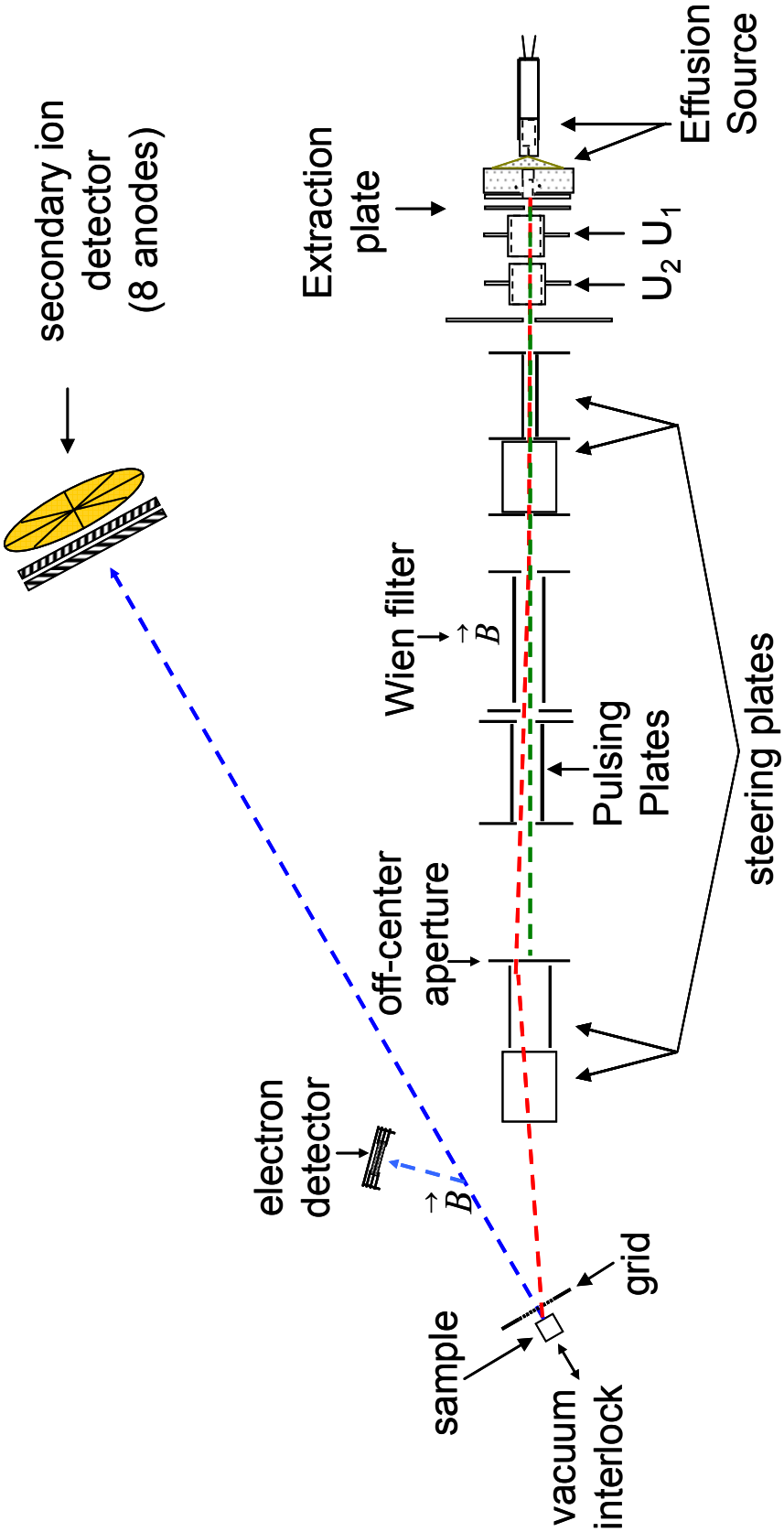

Figure 3-3: Schematic of the effusion source time-of-flight mass spectrometer (not to scale).

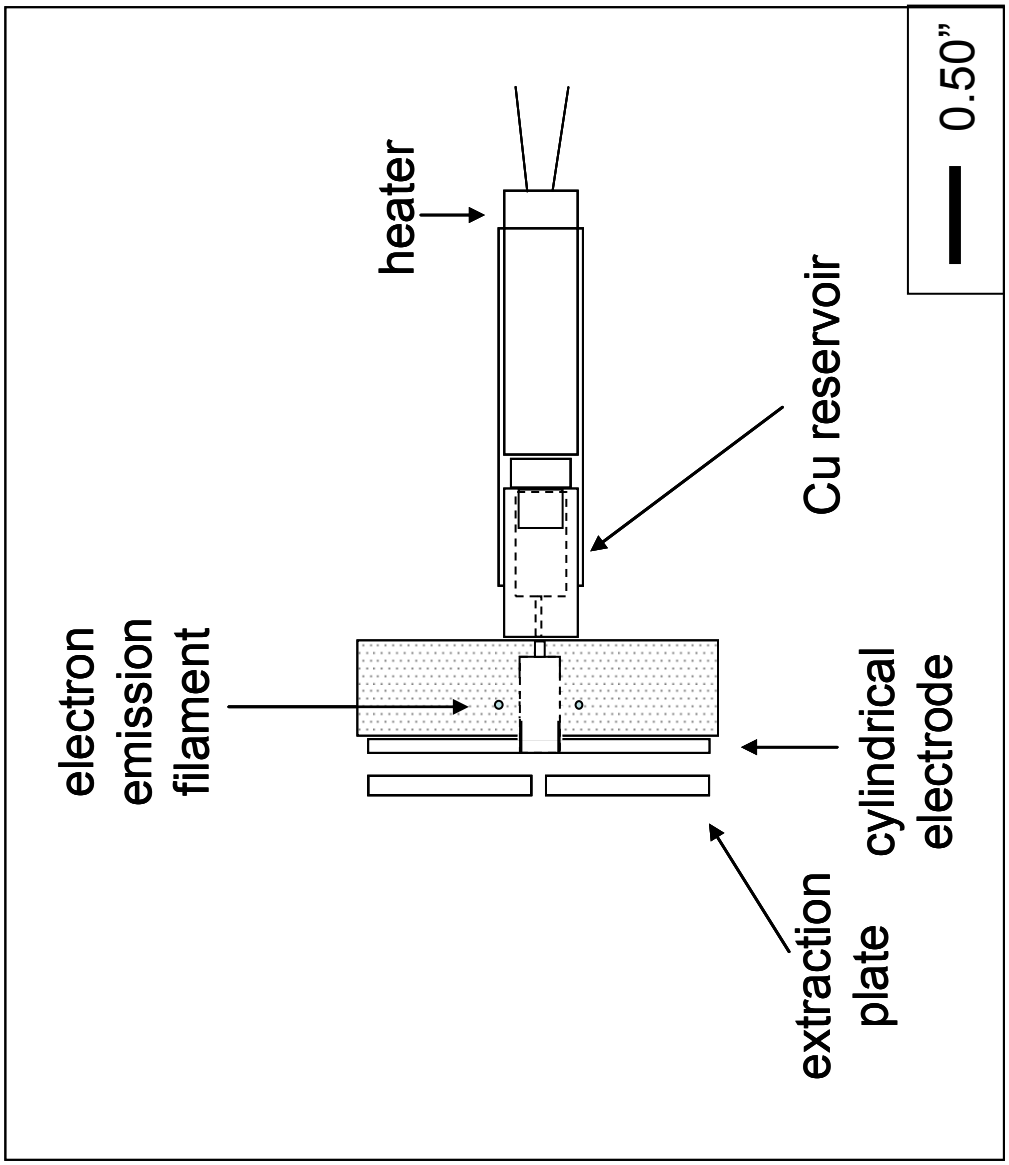

Figure 3-4: Schematic of the effusion source (Drawn to scale).

region, which is similar to other effusion-based sources seen in literature [72, 95-97]. A chosen material placed in the copper reservoir and heated in vacuum to its sublimation temperature (Watlow). The resulting vapor effuses into the cylindrical electrode area of the vacuum. The cylindrical electrode consists of a stainless steel cylinder in which approximately 80% of the surface is cut away and replaced with a grid of 0.01" tungsten wire (Alfa Aesar). This grid region allows penetration of electrons into the sublimed material causing ionization. The thermally emitted electrons are accelerated on the cylindrical electrode via a 30-100 V potential gradient between the cylindrical electrode and a heated tungsten filament. The ionization process produces numerous cations ranging from hydrogen to the molecular ion of the sublimed material.

The resulting ions are extracted by applying a voltage gradient between the cylindrical electrode and the extraction plate. The ions are accelerated toward a ground potential through a set of electrostatic lenses (U_1 and U_2), which are used to focus the extracted ions.

A Wien filter selects the ions of choice and steer them toward an off-centered aperture. A Wien filter consists of an electric field perpendicularly crossed with a magnetic field with ion selection being based on the ion velocity. The velocity of ions passed straight through the filter are described by

$$v = (10^8 \frac{V_d}{dB}) \qquad \text{Eq. 3-1}$$

where v is velocity in cm per second, V_d is the potential applied between the electric plates (V), d is the distance between the electric plates (cm), and *B* is the magnetic field strength (gauss). Combining Equation 3-1 with the kinetic energy equation yields the

following equation which specifies the difference in potential for the Wien filter electric plates for an ion of a given mass and kinetic energy:

$$V_d = K_1\sqrt{\frac{E_K}{m}} \qquad \text{Eq. 3-2}$$

where K_1 is a constant that includes the Wien filter parameters, E_K is the kinetic energy (volts), and m is the mass (amu) [98].

After ionization, some ions undergo meta-stable decay producing high velocity neutrals which are not affected by electric or magnetic fields. However, these high velocity neutrals cause secondary emission if allowed to impact the sample. This presents two problems: the type of projectile impacting the sample is unknown because primary mass selection may not occur, and the energy of the projectiles is unknown because the neutral may be formed prior to attaining the full kinetic energy supplied by the applied bias. Therefore the neutrals produced by the ion source are removed by allowing them to impact a barrier, an off-centered aperture. The ions are deflected slightly to pass through the aperture while the neutral are unaffected by the deflection fields and impact the solid portion of the aperture.

Two sets of steering plates are used in this instrument: one set to center the extracted ions on the opening of the Wien filter; the second, to align the mass selected primary ions onto the target such that the resulting secondary ions are centered on the 8 anode detector. The applied voltage necessary to center the selected primary ions on the 8 anode detector shows a linear dependence with respect to the source voltage (Fig. 3-5).

This dependence allows timely centering of the selected ions onto the sample with changing source potential.

Verification of the mass selection is accomplished using ToF. The mass selected ions are rastered across the 1 mm diameter off-center aperture by a set of pulsing plates. One plate is grounded while the other alternates between positive and negative potential. The later plate is driven by a high frequency MOSFET switch, which is capable of switching ±15 kV at 10 kHz (Belkhe, HTS). High voltage is provided to the switch by two 3 kV, 10 mA power supplies run at ±350 V (ORTEC), and driven by a Hewlett-Packard pulse generator at a frequency of 6 kHz. As the ions are swept across the aperture only a few have the appropriate trajectory to impact the target. Those ions impacting the target produce prompt electrons which signal the arrival of the ion at the sample. Using the start and stop signals, the mass-to-charge of the selected ion is verified (Fig. 3-6). Once the mass selection is verified, pulsing is stopped for the duration of the secondary ion acquisition.

Secondary Ion Region

The secondary ion region is contained within a custom-build stainless steel vacuum chamber. An operational vacuum of ~ $8*10^{-7}$ torr is maintained by a 760 l/s diffusion pump (BOC Edwards) backed by a 10.8 m^3/hr rotary vain pump (Welch).

The sample cube (7/8 in. x 7/8 in. x 7/8 in.) made of stainless steel or brass. The cube is placed in vacuum through a vacuum interlock. A vacuum of ~10^{-3} torr is obtained in the interlock chamber by a small rotary vain pump (Welch). Once this pressure is obtained, the rotary pump is closed off from the interlock chamber via a

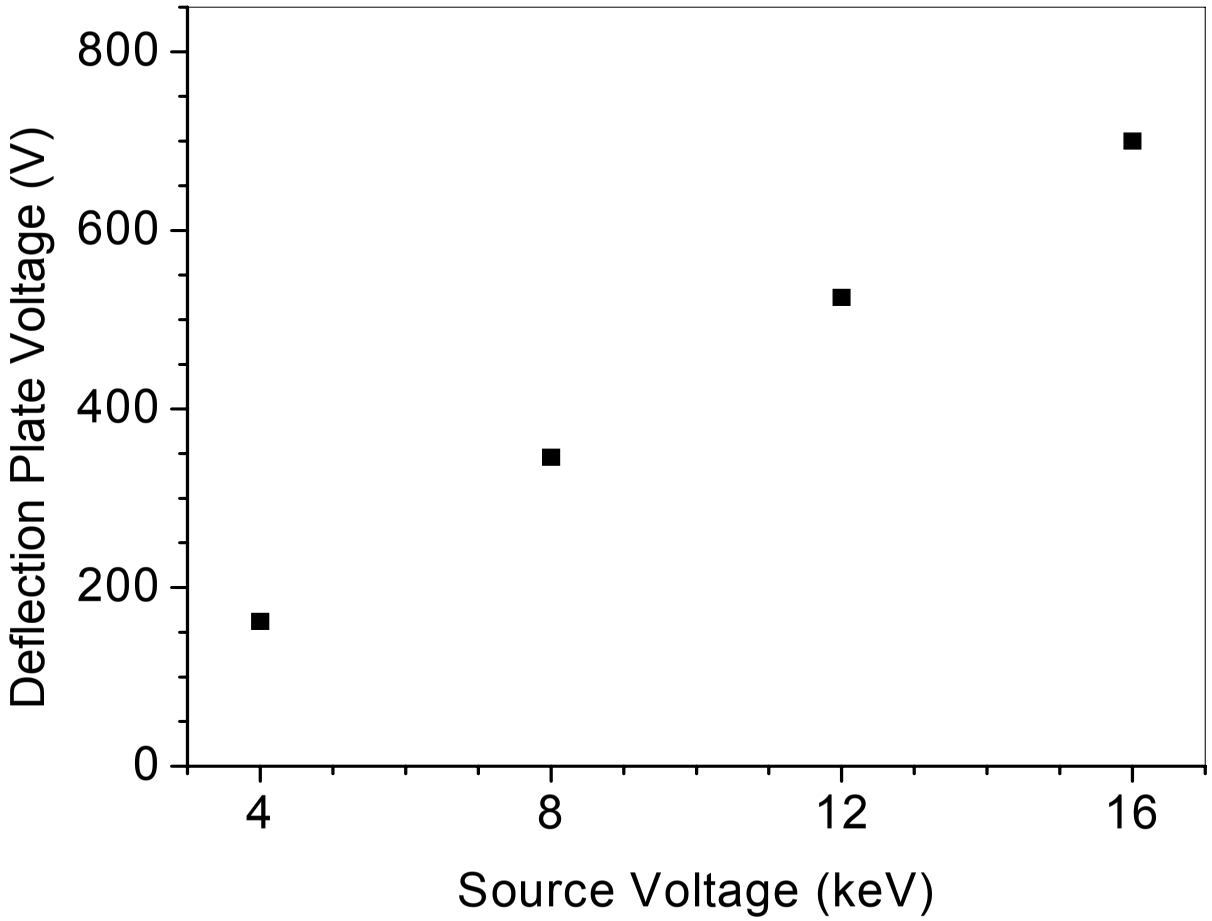

Figure 3-5: Steering plate voltage with respect to the total source voltage.

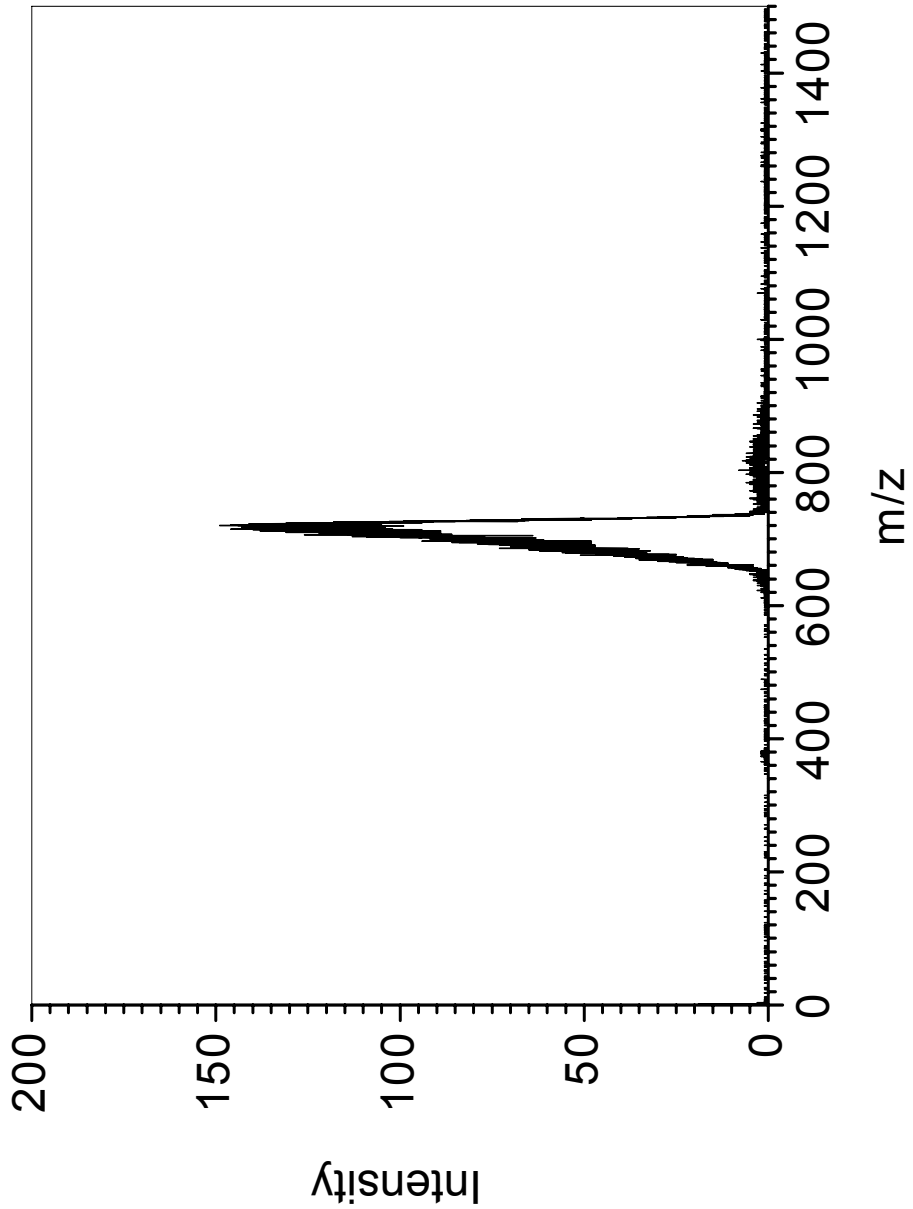

Figure 3-6: Mass selected primary ion spectrum of 8 keV C_{60}^{+} from the effusion source.

pop-up valve (Keys High Vacuum). Simultaneously, a gate valve to the main chamber is opened, which further reduces the pressure in the interlock chamber. The cube is inserted into the Teflon® holder by a liner-rotary feedthrough (MDC). The cube is negatively biased and separated by 0.375 in. (0.9525 cm) from a grounded 90% transmission grid (Precision Eforming, LLC.).

The potential gradient accelerates the secondary electrons and anions produced from primary ion bombardment away from the sample cube. Secondary electrons are steered towards a microchannel plate (MCP) assembly by a weak magnetic field (<100 gauss) and used as a start signal for the secondary ion ToF measurement. The secondary ions pass through the magnetic field with minimal effect and impact an 8 anode MCP assembly, which acts as a stop for the secondary ion ToF measurement.

Event-by-Event Bombardment and Detection

The experiments are conducted in the event-by-event bombardment and detection mode. In this method, individual projectile impacts and the resulting secondary ions are recognized as singular events resolved in time and space. For example, a single projectile impacts the sample causing secondary emission. The secondary particles are detected and recorded prior to the impact of another primary ion. Since each primary ion impact produces few secondary ions (~1 ion per impact on average for 26 keV C_{60}^{+} on Gly), the results of multiple impacts (~10^6) are summed to produce analytically significant data.

Principles of Time-of-Flight Mass Analysis

The secondary ions in the following experiments are analyzed by time-of-flight (ToF) mass spectrometry. The secondary ions proceed through three distinct regions between formation and detection: acceleration region, drift (field-free) region, post acceleration region (Fig. 3-7) [99]. The total time of flight (t_{tot}) an ion takes to traverse this distance is described by

$$t_{tot} = t_a + t_{dr} + t_p \qquad \text{Eq. 3-3}$$

where t_a is the time in the acceleration region, t_{dr} is the time in the field-free region, t_p is the time for post acceleration and detection region in seconds. The parameter, t_a, is calculated from

$$F = ma = zE \quad \text{and} \quad E = V_a / d_a \qquad \text{Eq. 3-4}$$

where F is the force (Newtons), m is the ion mass (kg), a is the acceleration (meters/sec^2), z is the charge of the ion, E is the electric field strength (V/meter), V_a is the applied bias to the sample (V), and d_a is the distance the ion travels through the electric field (meter). Making substitutions, yields the following

$$ma = z(V_a / d_a) \qquad \text{Eq. 3-5}$$

Since a = dv/dt and v = dx/dt integration yields:

$$v(t) = (zV_a / md_a)t + v_o \qquad \text{Eq. 3-6}$$

and

$$x(t) = (zV_a / md_a)t^2 + v_o t + x_0 \qquad \text{Eq. 3-7}$$

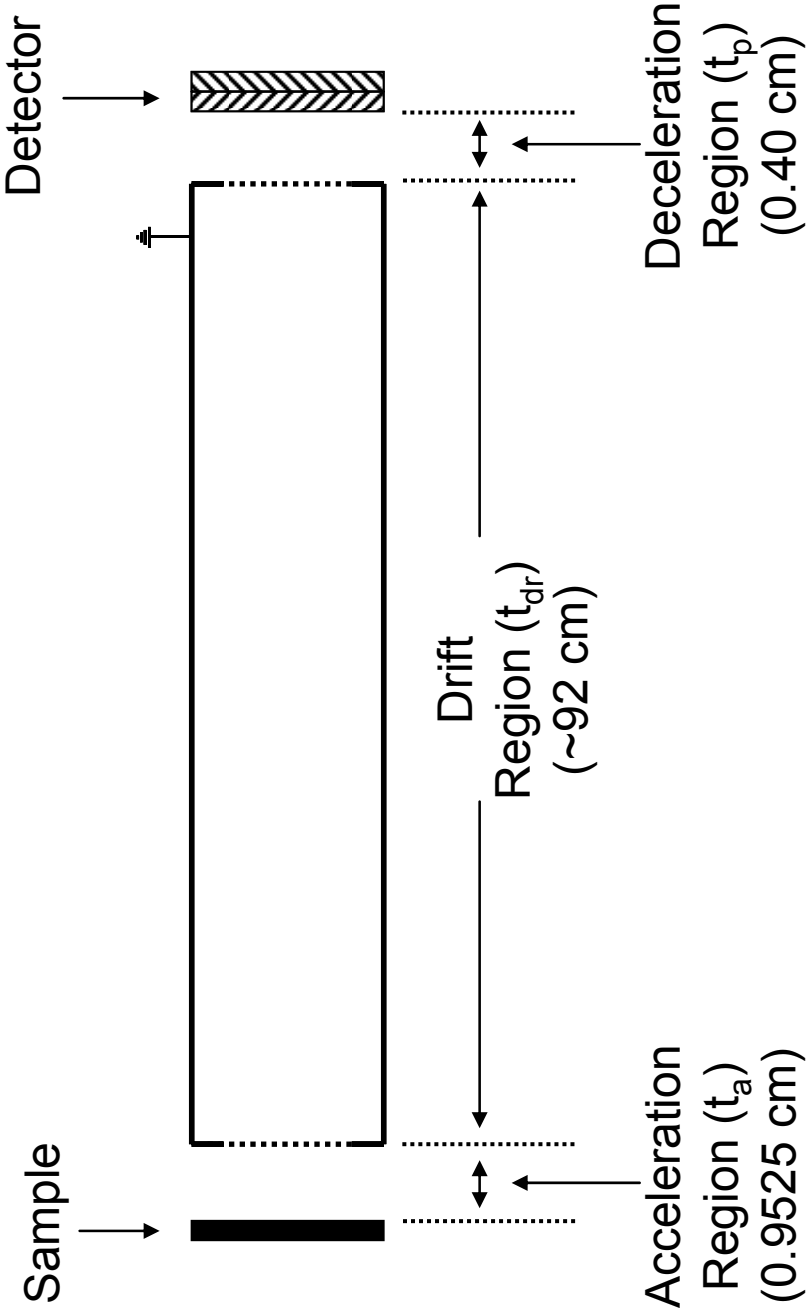

Figure 3-7: Time-of-flight schematic.

where v is the velocity of the ion in m/sec, t is time in sec, v_o is the initial velocity and x_o is the initial position. If v_o and x_o are negligible then Eq. 3-7 reduces to

$$x(t) = (zV_a / md_a)t^2 = d_a \qquad \text{Eq. 3-8}$$

Solving for t gives t_a, the flight time in the acceleration region:

$$t_a = (2md_a^2 / zV_a)^{0.5} \qquad \text{Eq. 3-9}$$

Since there are no external forces acting on the ions in this region, the flight time is the product of the ion velocity and the length of the drift region. The ion velocity is calculated by

$$E_K = mv^2 / 2 = zV_a \qquad \text{Eq. 3-10}$$

where E_K is the ion kinetic energy. Solving for v yields:

$$v = (2zV_a / m)^{0.5} \qquad \text{Eq. 3-11}$$

Therefore:

$$t_{dr} = (md_{dr}^2 / 2zV_a)^{0.5} \qquad \text{Eq. 3-12}$$

where d_{dr} is the length of the drift region.

Calculation of t_p is similar to t_a with the exception that initial velocity must be accounted for which yields:

$$t_p = (d_p^2(2m)^{0.5}[(V_a + V_p)^{0.5} \pm V_a^{0.5}]) / z^{0.5}V_p \qquad \text{Eq. 3-13}$$

Substituting Eqs. 3-9, 3-12, and 3-13 into Eq. 3-3 yields:

$$t_{tot} = (2md_a^2 / zV_a)^{0.5} + (md_{dr}^2 / 2zV_a)^{0.5} + (d_p^2(2m)^{0.5}[(V_a + V_p)^{0.5} \pm V_a^{0.5}]) / z^{0.5}V_p \qquad \text{Eq. 3-14}$$

This equation can be used to calculate the ToF of each ion provided the exact distances and voltages are known.

ToF Mass Calibration

In practice, the mass calibration is produced using the equation:

$$(m/z) = [(t_{tot} - C_2)/C_1]^2 \qquad \text{Eq. 3-15}$$

where C_1 is a constant depending on distances and voltages within the instrument and C_2 is constant determined by the speed of the electronics [45]. Two equations are generated from Eq. 3-15 by filling in flight times and mass-to-charge of two known ions (e.g., H^- and C_2H^-). The values for each constant can be determined by simultaneously solving the two equations.

Resolving power is a common term found in mass spectrometry. This term is described as the ability of an instrument to separate adjacent peaks from another. Resolving power is expressed as

$$\frac{m}{\Delta m} = \frac{t}{2\Delta t} \qquad \text{Eq. 3-16}$$

Since t is proportional to the channel number, Ch#, then:

$$\frac{m}{\Delta m} = \frac{Ch\#}{2\Delta Ch\#} \qquad \text{Eq. 3-17}$$

Microchannel Plate Detectors

Secondary ion and electron detection is achieved using microchannel plate (MCP) detectors (Burle Electro-optics). The MCPs are non-imaging quality with 10 μm diameter channels at 12° from normal. A gain of ~10^3 is produced by each MCP giving a gain of ~10^6 for two MCPs. The MCPs are arranged in a chevron configuration (Fig. 3-8). The detection efficiency of MCPs is velocity dependent. Therefore, the kinetic energy and mass of the ion influence detection efficiency [100-101]. A voltage divider

is used to apply voltage to the MCP assembly. The voltage divider arrangement is different for the electron detector and the secondary ion detector.

The voltage distribution on the electron detector (Fig. 3-8) is assembled such that the voltage increases from the front to the back. This configuration leaves the front of the assembly at ground keeping the field-free region intact. The voltage divider produces a voltage gradient of ~1000 V across each MCP with the highest voltage being applied to anode. The input high voltage (Tennelec, 3 kV, 10 mA) is transferred through a high pass filter, C_1 and R_1. The high pass filter reduces the low frequency noise emanating from the power supply. The signal produced on the anode is extracted via a low pass filter, C_2 and R_4 and serves as a start signal.

The voltage distribution on the secondary ion detector (Fig. 3-9) is assembled such that the voltage decreases from the front to the back. In order to maintain the field-free region a grid is installed before the first MCP. This region decelerates anions before impacting the MCP because of the bias applied to the MCPs. The voltage divider produces a voltage gradient of ~ 1000 V across each MCP with the highest voltage being applied to front MCP. Again, the input high voltage (Tennelec, 3 kV-10 mA) is transferred through a high pass filter, C_1 and R_1. The secondary ion detector anode is segmented into eight independent sections in a pie-shaped configuration (Fig. 3-9). Each segment produces an independent signal, which is used as a stop for the secondary ion ToF measurement. A more detailed explanation of the 8 anode detector is available elsewhere [102]. As mentioned previously, the ToF instruments use a pulse counting

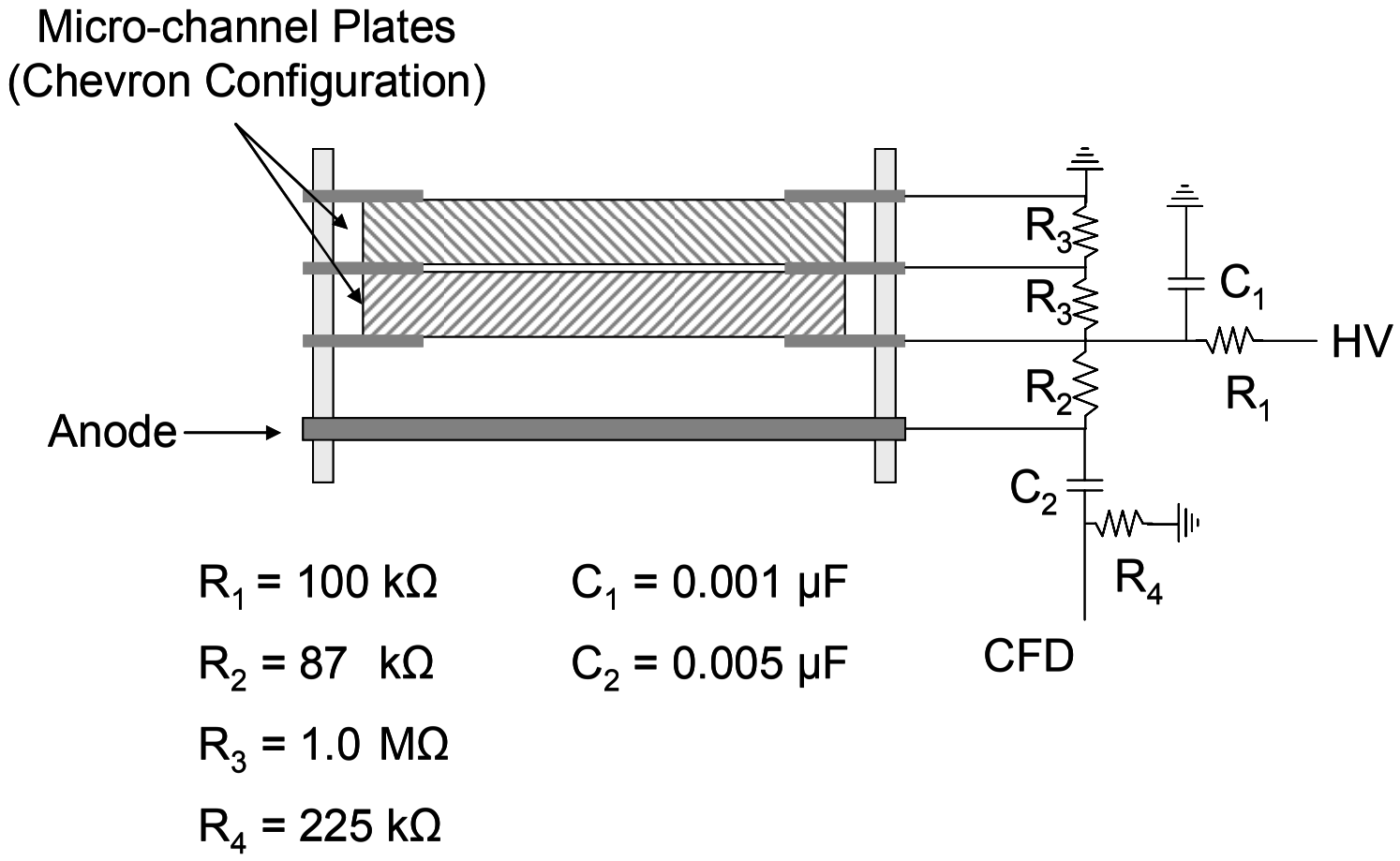

Figure 3-8: Schematic of the microchannel plate detector assembly for the electron start detector with a 25 mm active area (not to scale).

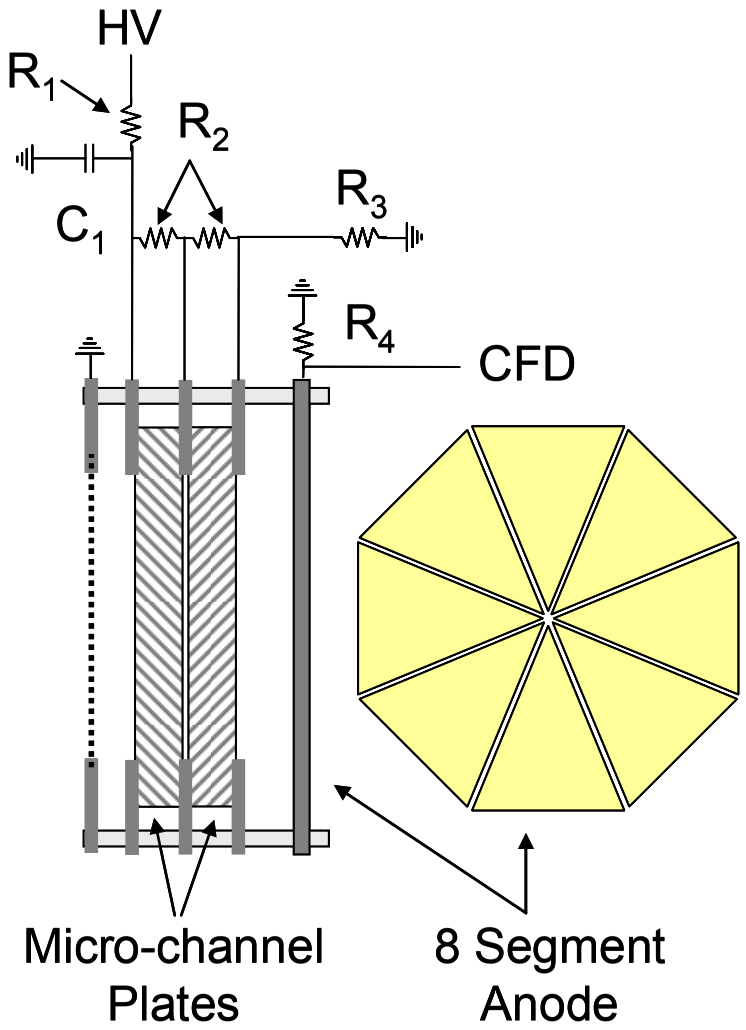

R_1 = 100 kΩ

R_2 = 1.0 MΩ

R_3 = 87 kΩ

R_4 = 20 kΩ

C_1 = 0.001 μF

Figure 3-9: Schematic of the microchannel plate detector assembly for the secondary ion stop detector with a 40 mm active area (not to scale).

arrangement and thus can not distinguish between two or more ions of the same mass-to-charge arriving simultaneously at a single anode detector. By segmenting the anode into eight independent sections, up to eight ions of the same mass-to-charge can be detected at once, thereby minimizing signal loss.

Detector Optimization

The pulse amplitude is used to distinguish between a true start signal and false starts due to detector noise. Signal above a given amplitude (threshold) is deemed a true start signal. The removal of false starts reduces the noise in the mass spectra by removing uncorrelated secondary ion signals. The minimum threshold is established empirically. The start signal threshold is increased systematically until the yield (i.e., the number of secondary ions divided by the number of primary projectiles) reaches a plateau signaling the elimination of the false starts. Raising the threshold beyond the minimum plateau value discards true starts, which reduces the instrument duty cycle. Figure 3-10 depicts an example threshold optimization. The yield of I^- from a CsI sample increases as a function of the start threshold reaching a plateau at ~ 22.5 mV.

The secondary ion thresholds are placed a minimum so that true signal is not missed. The secondary ion detector is optimized by establishing the highest signal-to-noise (S/N) ratio. The MCP bias is systematically increased while monitoring the S/N of a given secondary ion. Figure 3-11 shows the S/N dependence of CsI_2^- from a CsI sample with the secondary ion detector bias. Initially, the S/N rises with the bias as the detection efficiency is increase reaching a maximum. Beyond this maximum, further voltage increases reduce the S/N because of bias induced noise ("ringing").

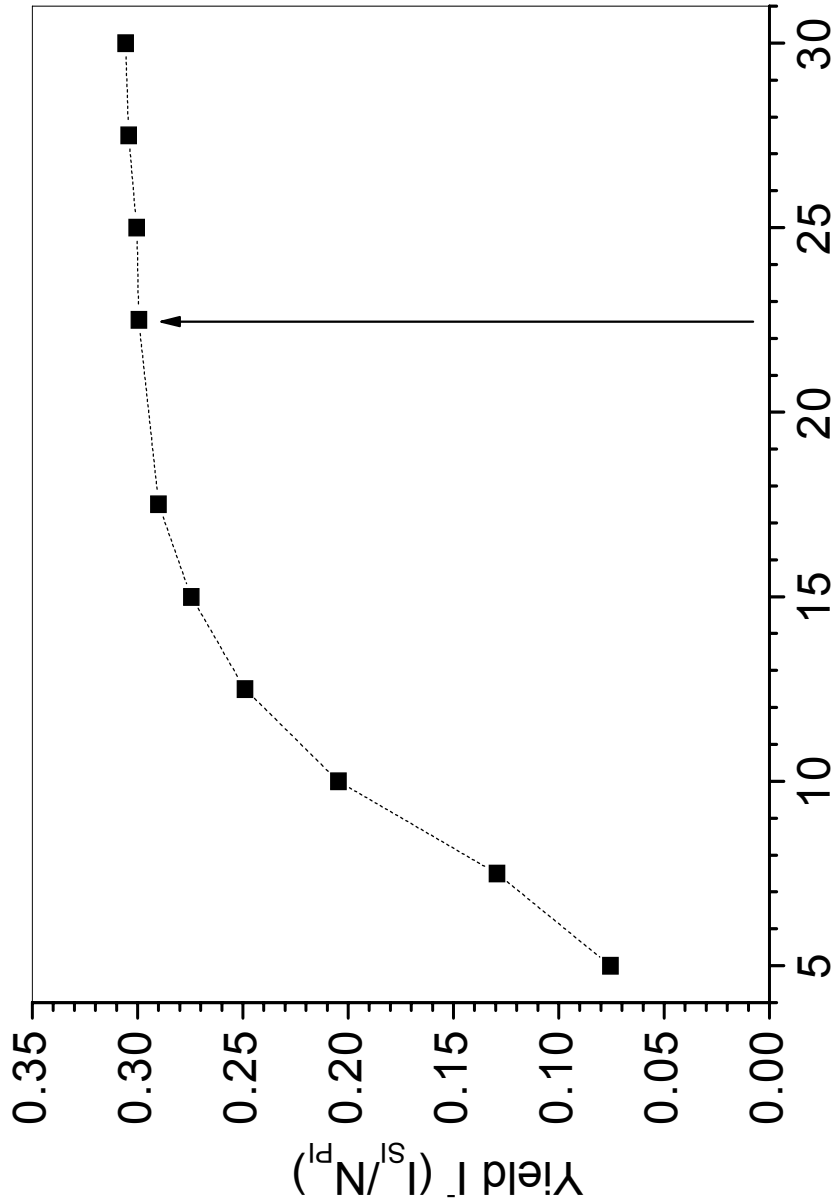

Figure 3-10: Yield of I⁻ from a CsI sample as a function of the CFD threshold for the start detector. The bias on the start and stop detectors as well as the CFD thresholds on the stop detector are constant.

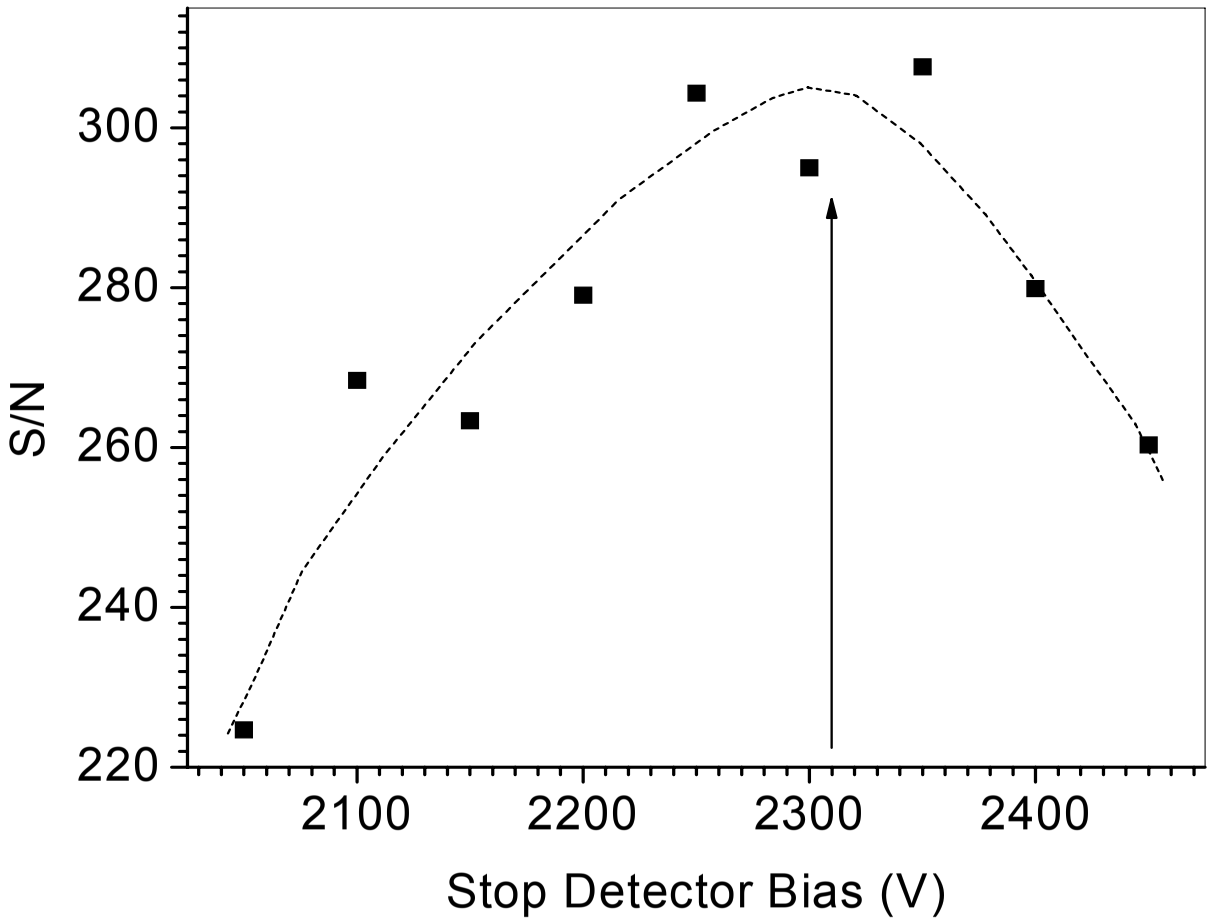

Figure 3-11: Signal-to-noise ratio for CsI_2^- from a CsI sample as a function the stop detector bias. The start detector bias and the start CFD threshold are constant.

The detectors slowly degrade over time. Therefore, detector optimization is done periodically to insure the uniformity of measurements over extended time periods. Additional optimization must be performed after instrument maintenance (i.e., MCP replacement and/or cleaning, and when MCPs are exposed to air) as the detection efficiency may be affected.

Signal Processing

The output from the pulse generator and electron detector are shuttled through a 4 port constant fraction discriminator, CFD (Tennelec). The output from the secondary ion detector is shuttled through an 8 port constant fraction discriminator, CFD (Ortec). The incoming signals have variation in there arrival time due to differences in the pulse amplitude (i.e., signal walk). The CFD compensates for this phenomenon by splitting a unipolar input signal into two paths. In one, the signal is inverted and attenuated. In the other, the signal is not attenuated, but delayed. The attenuated and delayed signals are then combined producing a bipolar pulse. This bipolar pulse is independent of the pulse amplitude. The discriminator threshold sets minimum input pulse amplitude that will activate the process described above. The CFD has a third parameter called "blocking width". This controls the width of the output signal and is adjustable from <10 ns to >500 ns. For the start signal, this value should be as large as possible not exceeding the total analysis time. For the stop signal, a minimal width should be used. This reduces probability of signal loss due to ions being less than a blocking width apart. The CFD output is transferred to a Time-to-Digital Converter (TDC) (Ins. Phys. Nucl., Orsay, France). The TDC converts the analog signal to a digital signal and passes the data to a

personal computer. The data is stored and processed by a program known as "Total Matrix of Events", TME. This program is described in detail elsewhere [103]. Figure 3-12 shows the signal processing schematic from the effusion-based ToF instrument. The primary ion ToF start signal is produced by the output of the pulse generator (A), which is routed through a CFD to TDC 1. The impact of the primary ion causes the emission of secondary electrons which are steered towards a MCP assembly (B). This signal has two purposes: the primary ion stop signal is routed through a CFD to TDC1 providing primary ion verification, while the second is routed through a CFD to TDC2 providing a start signal for the secondary ion ToF analysis. The secondary ions impact an 8 anode MCP assembly producing 8 independent signals which are shuttled to an 8 port CFD followed by TDC2. Each of the 8 signals produced is correlated to a single projectile impact. In practice, only one TDC is used since the primary and secondary ion ToFs are not acquired simultaneously.

Secondary Ion Yields

Secondary ion yield refers to the number of ejected secondary ions of interest per projectile impact. The secondary ion yield (Y_{SI}) is defined as:

$$Y_{SI} = ((I_{SI} - I_{BG})/N_{PI}) \qquad \text{Eq. 3-18}$$

where I_{SI} is the experimental secondary ion yield, I_{BG} is the background noise, and N_{PI} is the number of primary ion impacts. A background subtraction is done to remove counts from a peak of interest which originate primarily from meta-stable decay and random noise.

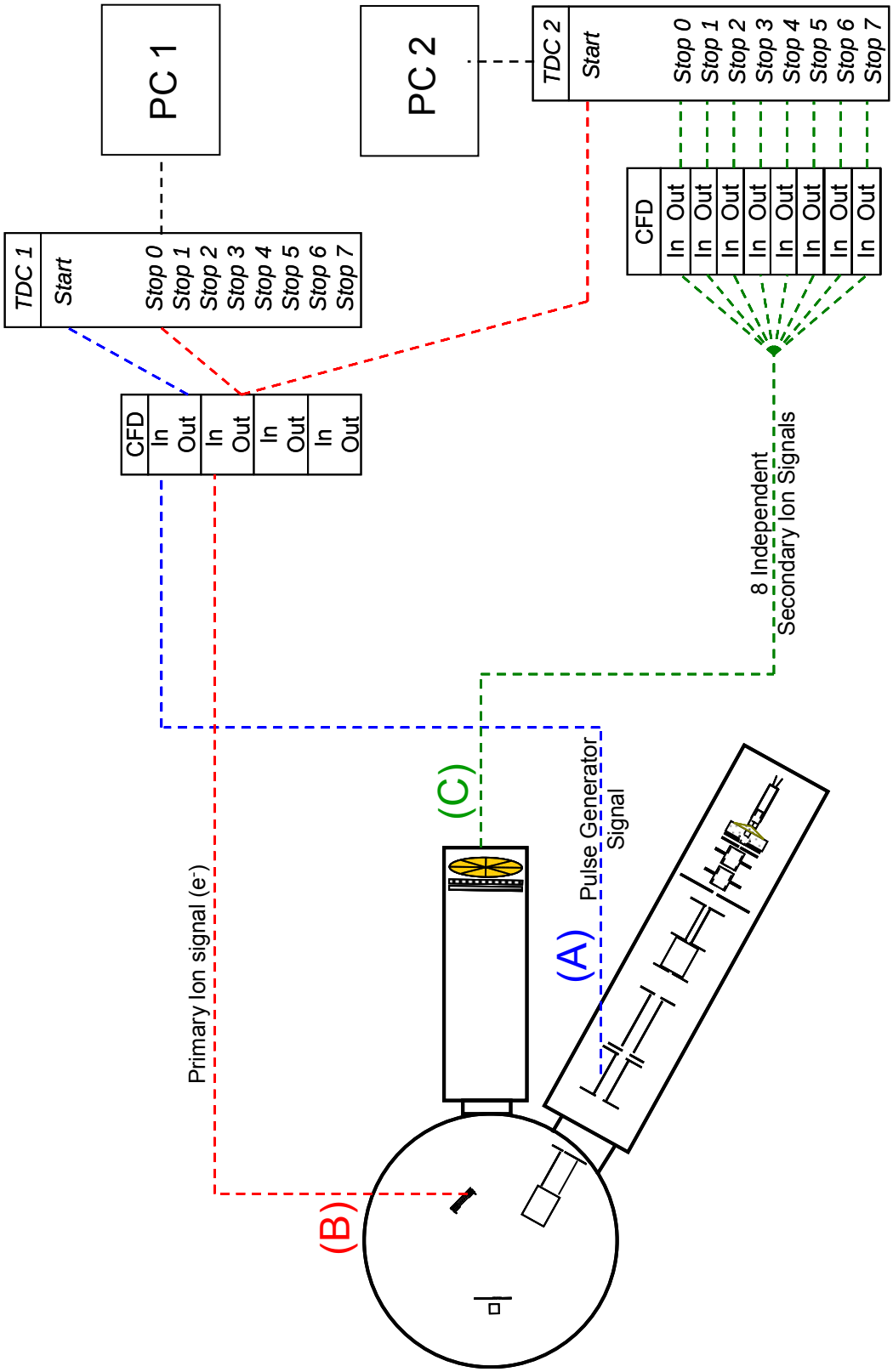

Figure 3-12: Signal processing schematic of the effusion source ToF mass spectrometer.

^{252}Cf Mass Spectrometer Source Foil Preparation

Primary ion source materials were obtained from Sigma-Aldrich. Coronene and C_{60} were vapor deposited on Mylar® foil (described in detail later). One hundred microliters each of saturated solutions of gramicidin S and 3, 5-dimethoxy-4-hydroxy-cinnamic acid in methanol were mixed. Forty microliters of the mixture was deposited on an aluminized Mylar® foil and dried leaving a thin deposit of analyte and matrix.

Effusion Source Mass Spectrometer: Source Material Preparation

Coronene and C_{60} were obtained from Sigma-Aldrich. $C_{60}F_{48}$ was obtained from Term-USA. Coronene and C_{60} are formed into small pellets (~0.1" diameter x ~0.1 height) by compressing to ~ 10,000 psi with a Carver laboratory press. The pellets are loosely bound and crumble along the edges when handled. Making the materials into pellets reduces the surface area. This helps control the sublimation process. $C_{60}F_{48}$ forms large crystals when dissolved in chloroform or dichloromethane and therefore was not pressed. The mass-to-charge of the ionized species resulting from the ionization of $C_{60}F_{48}$ is 1480. This corresponds to the removal of 8 fluorine atoms resulting in the ion, $C_{60}F_{40}^{+}$.

Sample Preparation

Sample preparation in these experiments is divided into two categories: vapor deposition and solution deposition. Vapor deposition is the preferred manor of preparation because of the high reproducibility and uniformity of the resulting sample. However, not all samples can be vapor deposited because of thermal degradation occurs during the heating process (i.e., gramicidin S).

Vapor depositions were performed in a small rectangular vacuum chamber (~ 3”x 9” 5”) (fig. 3-1). Vacuum conditions of ~10^{-5} torr were maintained during the depositions by a 240 l/s turbo pump (Pfeifer-Balzers) backed by 12 cfm rotary vane mechanical pump (BOC Edwards). The compound to be vapor deposited is placed in an Al boat which is heated using a 0-20V, 0-45 amp DC power supply.

The vapor deposition procedure is similar for glycine, phenylalanine, proline, histidine, guanine and coronene deposition. The system is allowed to pump down for ~ 5 min (~10^{-5} torr). The Al boat is increasingly heated in five minute increments until vapor deposition of the material occurs. For example, glycine is heated for five minutes at ~0.5 V and ~4 A, and then the current is increased to ~8 A for five minutes. At the end of this time glycine is generally been heated to a point where vaporization deposition is occurring on the sample. However if deposition is not occurring, the current is increased 1 A per minute until deposition occurs. Heating is done in stages to avoid thermal degradation of the materials prior to sublimation.

The vapor deposition procedure varies only slightly for C_{60}. Again, the system is allowed to pump down for ~ 5 min (~10^{-5} torr). The boat is increasingly heated in 4 stages. The current to the boat increased ~4 A every 5 minutes up to 16 A. If deposition is not occurring, the current is increased 1 A per minute until deposition occurs. The deposition of C_{60} corresponds to the temperature at which the Al boat begins to emit in the far red region of the visible spectrum such that in a completely dark room a faint red glow is observed from the boat.

In instances where isotopic mixtures were used, the target material was prepared by mixing the molar amounts of labeled and non-labeled glycine and phenylalanine in solution. This produces a homogeneous mixture of the materials. The dried mixture is then vapor deposited on a sample cube.

The solution deposition procedure is used with the peptides arginine-phenylalanine, tryptophan-tryptophan, gramicidin S and mixtures of gramicidin S and sinapic acid. The deposition process is dependent on two factors: the matrix/analyte ratio and the uniformity of the dried matrix/analyte film. To deposit uniform dried matrix/analyte films, the total mass of the dried matrix/analyte film deposited on the surface was considered. Uniform films were produced by depositing approximately 7.5 micrograms of material. This is described by the following equation:

$$m_T = m_{GS} + m_{SA}$$

where m_{GS} and m_{SA} are deposited mass of gramicidin S and sinapic acid, respectively, and m_T is the deposited film mass. The matrix/analyte ratio is described by:

$$(m_{SA} / M_{SA}) : (m_{GS} / M_{GS})$$

where M_{SA} and M_{GS} are the molecular weights of sinapic acid and gramicidin S, respectively. The matrix/analyte ratio is varied while maintaining a constant deposited film mass.

Al_2O_3, Cu, and Ag samples were prepared by adhering foils of the respective metal onto the sample cube via double sided tape. Cu and Ag foils (Sigma-Aldrich) were sanded with 600 grit sandpaper to remove any oxide layer present, cleaned with methanol, dried by compressed N_2 gas, and inserted immediately into chamber for

analysis. Al foil was cleaned with methanol, but not sanded in order to preserve the native oxide layer.

Au samples were prepared by adhering gold coated Si wafers onto the sample cube via conductive paint. The Au wafer was cleaned with methanol, dried by compressed N_2 gas, and inserted into chamber for analysis.

BN and NaCl samples were prepared by adhering powdered material via double-sided tape to the sample cube. Excess powder was remove by contact with a gloved finger using a circular motion with light pressure followed by tapping of the powdered sample to remove lose particles.

CHAPTER IV

COINCIDENTAL EMISSION OF MOLECULAR IONS FROM KEV CARBON CLUSTER IMPACTS*

As discussed in Chapter II, cluster projectiles greatly increase secondary ion yields compared to equal velocity atomic projectiles. Furthermore, ion bombardment with small Au clusters has shown increases in multiple ion emission with increasing primary ion complexity [49]. Ions emitted from a single projectile impact (i.e., co-emitted or coincidental ions) are useful for surface analysis if the ions are representative of the surface. The effectiveness of using co-emitted ions for surface analysis has been demonstrated [45-48]. Non-imaging characterization using the event-by-event technique was used to analyze the relative abundance of a dopant on nano-sized objects [90]. The effectiveness of this nano-characterization depends on the occurrence of multi-ion events. Therefore, projectiles that produce more analytically significant co-emitted ions would increase the effectiveness this technique.

Since higher yields of Phe $[M-H]^-$ have been observed when comparing keV carbon-cluster projectiles to small Au cluster projectiles [62] and multiple ion emission has been shown to occur with small Au clusters [49], it is of interest to examine the yield

*Reprinted excerpts and figures from the International Journal of Mass Spectrometry, vol. 238, J. E. Locklear, S. V. Verkhoturov, and E. A. Schweikert, Coincidental emission of co-emitted of molecular ions from keV carbon cluster impacts, pg. 59, Copyright 2004 with permission from Elsevier.

ions from keV carbon projectiles to assess their potential for non-imaging nano-domain analysis.

We report here the first experimental data for the co-emission of two phenylalanine (Phe) molecular ions from keV coronene ($C_{24}H_{12}$), C_{60}, and gramicidin S ($C_{60}N_{12}O_{10}H_{92}$) projectile impacts as a function of projectile characteristics. The secondary ion and coincidental ion spectra produced by carbon cluster projectiles are shown in Fig 4-1.

The experimental secondary ion yields are influenced by the nature of the target surface. The following equations describe the experimental ion yield for a specific case (i.e., a surface composed of one-half Phe_H and one-half Phe_D)

$$Y(\mathrm{Phe})_{\mathrm{exp}} = Y(\mathrm{Phe_H})_{\mathrm{exp}} + Y(\mathrm{Phe_D})_{\mathrm{exp}} = \frac{I(\mathrm{Phe_H})}{N} + \frac{I(\mathrm{Phe_D})}{N} \qquad \text{Eq. 4-1}$$

where $Y(\mathrm{Phe})_{\mathrm{exp}}$ is the experimental ion yield of all $[M\text{-}H]^-$ phenylalanine ions, $Y(\mathrm{Phe_n})_{\mathrm{exp}}$ is the experimental ion yield for $[M\text{-}H]^-$ phenylalanine ions of a specific fraction (n = H or D), I is the number of detected ions of a specific target fraction, and N is the number of primary ion impacts. Each species represents 50% of the surface (ρ = 0.5), therefore

$$Y(\mathrm{Phe_H})_{\mathrm{exp}} = Y(\mathrm{Phe_D})_{\mathrm{exp}} \qquad \text{Eq. 4-2}$$

and

$$Y(\mathrm{Phe})_{\mathrm{exp}} = Y(\mathrm{Phe_D})_{\mathrm{exp}} / \rho \qquad \text{Eq. 4-3}$$

where ρ is the relative concentration.

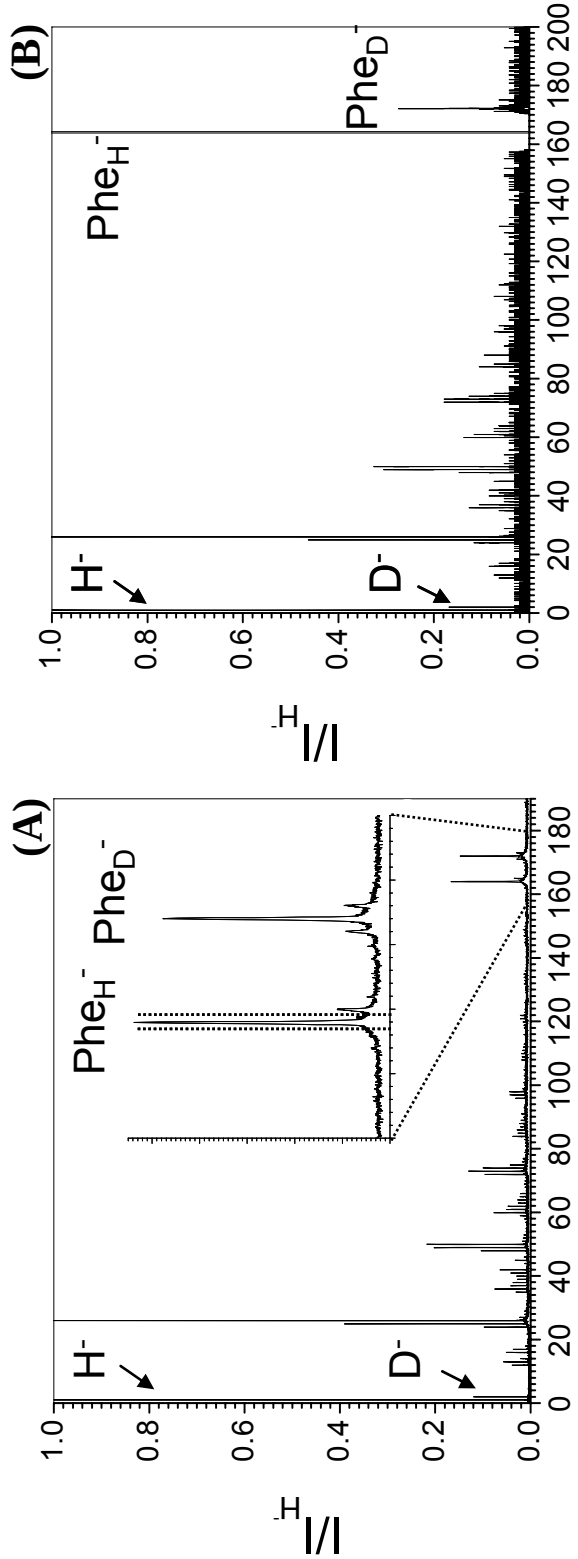

Figure 4-1: Negative secondary ion ToF spectrum produced by 21 keV C_{60}^+ bombardment on (A) 50/50 phenylalanine/d_8-phenylalanine vapor deposited sample. The inset is an enlarged view of the molecular ion region (dashed lines identify the coincidental ion window), (B) coincidental ion spectrum (all ions co-emitted with 164 m/z).

The impact velocities of the projectiles are considerably different at identical impact energies. For example at 21 keV, the impact velocities of coronene, $C_{60,}$ and gramicidin S are approximately 116.1 km/s, 75.0 km/s, and 59.6 km/s, respectively. In order to compare the projectiles at equal impact energies per constituent atom (neglecting hydrogen), the impact energies are divided by the atomic mass of the respective projectile. The SI yield is divided by atomic mass to compare the SI yields per constituent of the projectiles.

There is a linear relationship between the yield and the energy per projectiles atom (Figs. 4-2, 4-3). The yield/amu of Phe is approximately the same for coronene and C_{60} projectiles at equal velocity (Fig. 4-3). A similar trend was previously observed while bombarding an organic surface with carbon clusters having a few hundred eV per atom [61-62]. This behavior is in contrast to what is observed in bombardment with atomic ion and small cluster with kinetic energies of thousands of eV where the sputtering yield depends on the elastic stopping power. The case of massive projectiles with impact energies of hundreds of eV per atom has been modeled by Bitensky [104-105]. In this model, the dependence of the yield (Y^-) versus energy (E) for negatively charged secondary ions is expressed as follows

$$Y^- \propto E \cdot f(x) \qquad \text{Eq. 4-4}$$

where *f(x)* is a complex power function [75]. The variable x is a function of the following parameters

$$x = \beta \cdot E^{1/3} / \exp(-z/\lambda) \qquad \text{Eq. 4-5}$$

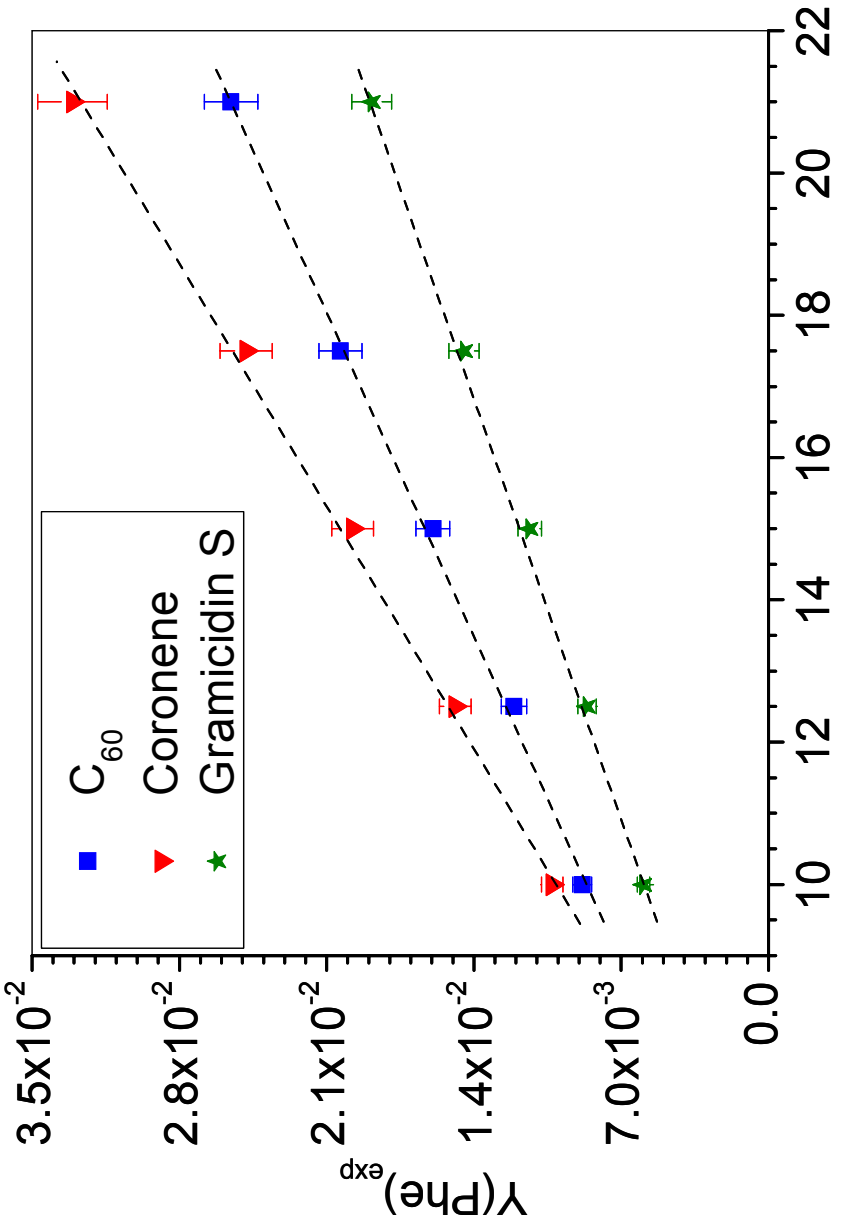

Figure 4-2: Negative secondary ion yields of Phe per projectile impact as a function of impact energy (note: the SI yields of Phe are the sum of peak areas of Phe_H^- and Phe_D^-). The error bars for the data are < ± 5% (dashed lines are to guide the eyes).

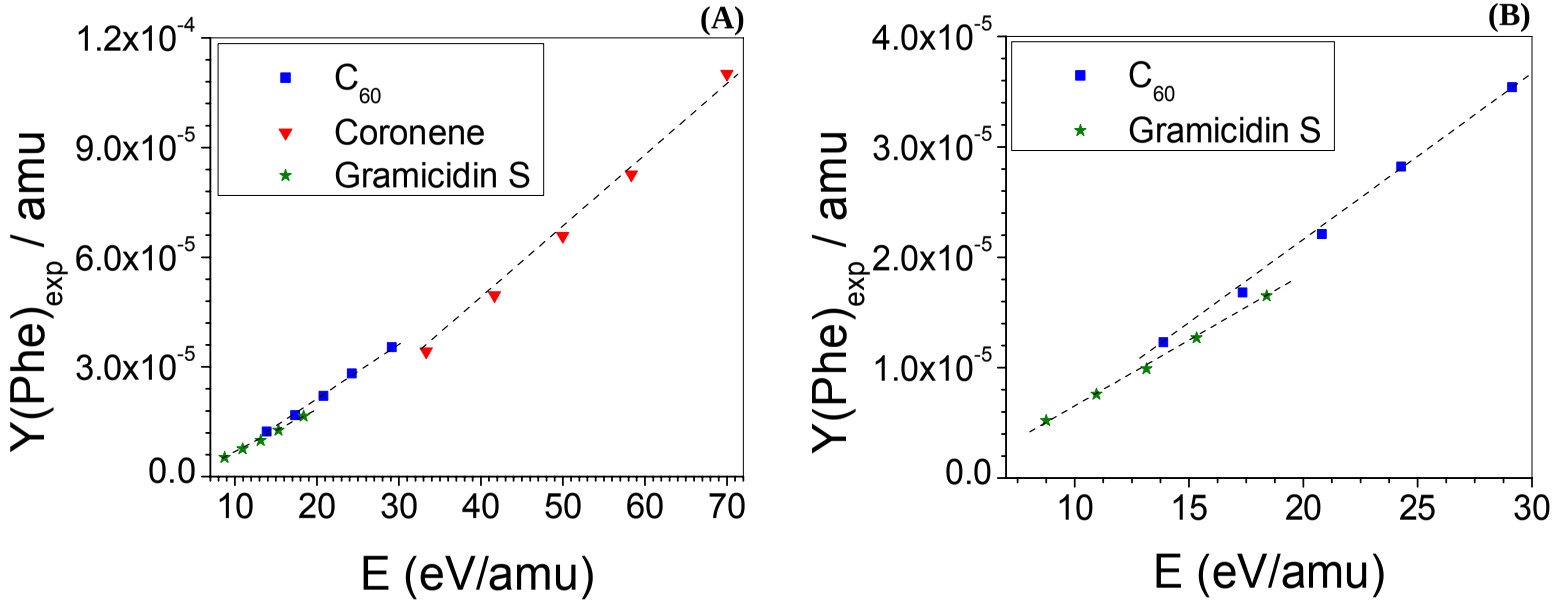

Figure 4-3: (A) Negative secondary ion yield per amu of Phe as a function of impact velocity, (B) enlarged view of the secondary ion yield per amu of Phe as a function of impact velocity (note: the SI yields of Phe are the sum of peak areas of Phe_H- and Phe_D-). The error bars for the data are < ± 5% (dashed lines are to guide the eyes).

where β is a projectile shape factor, which is highest for spherical projectiles; z is the ion formation depth inside the crater created by the projectile, and λ is the mean free path of the secondary ion before neutralization. In the case of a high survival probability for the secondary ion ($x << 1$), the ions are emitted from the total crater volume and Equation 4-4 reduces to

$$Y^- \propto E \qquad \text{Eq. 4-6}$$

The experimental ion yield dependences reported here are well approximated by Eq. 4-6 within the experimental energy range (Figs. 4-3, 4-5). The Equations 4-4 and 4-6 are valid at impact conditions where crater formation occurs. Molecular dynamics (MD) simulations show cluster emission from the entire volume of the craters perturbed by low energy C_{60} impacts [53]. Specifically, a distribution of clusters is emitted with smaller clusters (i.e., fragments) emanating from the center of the desorption volume with progressively larger clusters (i.e., fragments and intact molecules) emanating farther from the center. Our observations show high secondary ion yields for Phe molecular ion and its fragments, which is in agreement with Bitensky's model and MD simulations.

The comparison of SI yields of H and D per constituent produced by equal velocity projectiles reveals several differences. The relative positions of D ion yields to the H ion yields from C_{60} and gramicidin S bombardment are inverted from one data set to the other. The SI yields of H from coronene and C_{60} impacts are not in alignment in the H data (Fig. 4-4), while the SI yields of D from coronene and C_{60} are similar at equal velocity (Fig. 4-6). This difference in the relative orientation of H and D secondary ion yields from C_{60} and gramicidin S is directly related to the origin of the ions. The D ions

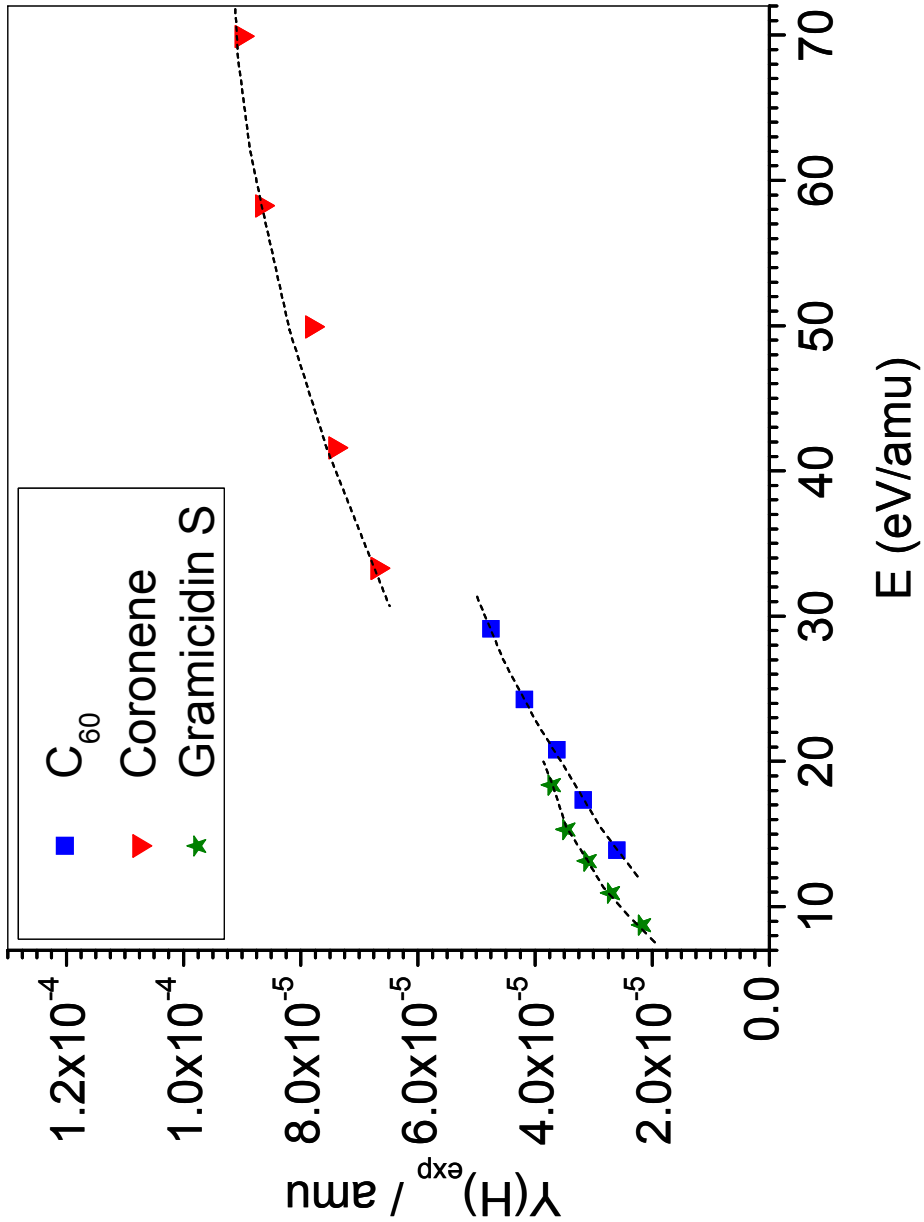

Figure 4-4: Secondary ion yield per amu of H^- as a function of projectile impact velocity from a phenylalanine sample (dashed lines are to guide the eyes).

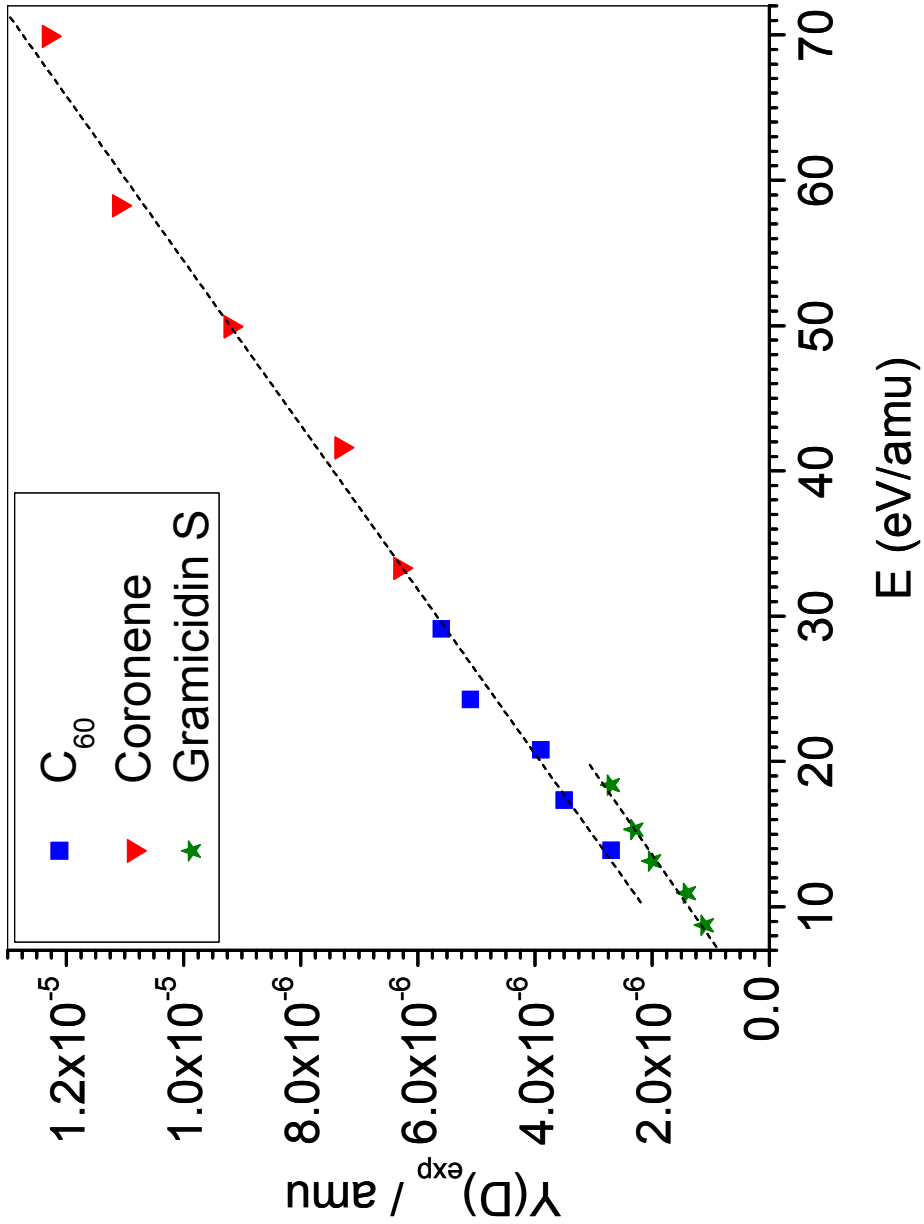

Figure 4-5: Secondary ion yield per amu of D^- as a function of projectile impact velocity from a phenylalanine sample (dashed lines are to guide the eyes).

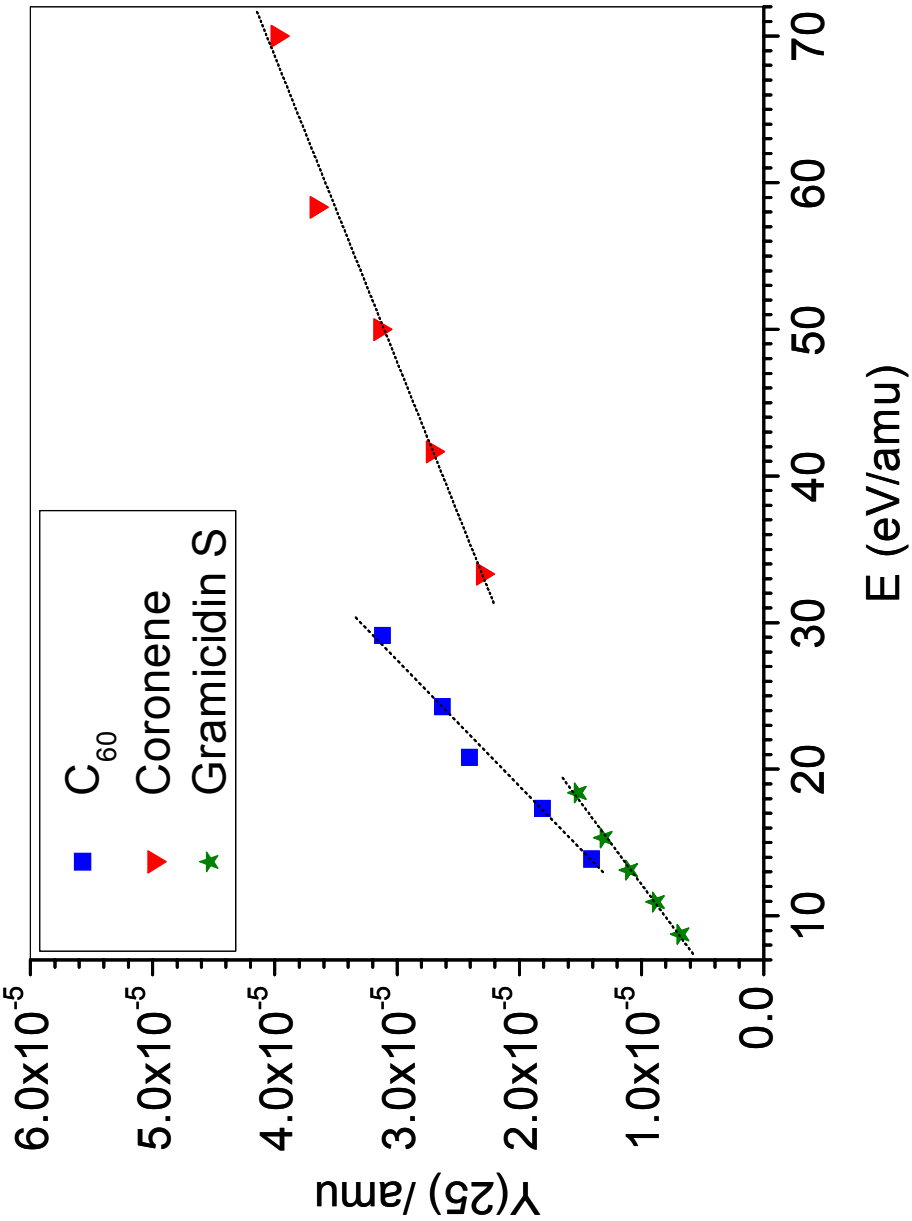

Figure 4-6: Negative secondary ion yield per amu of m/z = 25 as a function of projectile impact velocity from a phenylalanine sample (dashed lines are to guide the eyes).

must originate from the phenylalanine volume. However, hydrogen has three possible sources: the phenylalanine volume, surface contamination and the primary projectiles (coronene and gramicidin S). Recoiled hydrogen from gramicidin S increases the SI yield of H for this projectile which inverts the relative positions of the SI yields of D and H (i.e., for yields of H, gramicidin S has a higher yield than C_{60} while the yield of D is higher for C_{60} than gramicidin S at equal velocities). Similar observations of recoiled ions have been observed [106]. These additional hydrogen sources may account for the deviation of hydrogen yields (Fig. 4-4) from the behavior described by Eq. 4-6.

The yields of Phe caused by C_{60} impacts is ~20 percent higher than the yields of Phe caused by gramicidin S impacts at equal velocities (Fig. 4-3). This is also observed in the yields of deuterium (Fig. 4-5). The primary projectile structure may influence the SI yields as explained by the Bitensky model [104]. According to this model, one parameter affecting the sputtering yield is the projectile shape factor (β). The structural differences in the projectiles (i.e., C_{60} is a rigid, covalently bonded, sphere, while gramicidin S is a comparatively flexible, hydrogen-bonded, quasi-spherical structure) may influence the emission of secondary ions from C_{60} and gramicidin S impacts.

A second explanation for the higher yield produced by C_{60} compared to gramicidin S may be attributed to changes in the ionization process due to the direct deposition of oxygen into the desorption volume. It is well documented that many factors, such as surface work function, ionization potential and electron affinity of the emitted ions affects the ionization probability. The importance of each factor varies depending on the ionization process [107]. Several studies have shown increases in the

SI yields of both anions and cations from single crystal surfaces in the presence of oxygen [108-110]. More relevant to our experiment are observations made involving carbide surfaces. It was observed that oxygen absorption decreased the emission of most carbon containing ions on carbide surfaces [10]. The depression of D and Phe yields produced by gramicidin S may be attributed to changes in the ionization process due to the presence of oxygen in gramicidin S (Figs. 4-3, 4-5).

The yields of m/z = 25 and m/z = 26 (CN^-), which are fragments produced on primary ion impact, show a similar difference in yields between C_{60} and gramicidin S as seen in the yield of Phe (Figs. 4-3, 4-6, 4-7). This adds further evidence that a significant difference is observed when using these molecules as projectiles.

An additional observation can be drawn when comparing the yields of m/z = 25 and CN^- to the yield of Phe (Figs. 4-6, 4-7). As mentioned earlier the yields of Phe produced by C_{60} and coronene are approximately the same at equal velocities. This trend is not observed in the yields of m/z = 25 and CN^-. This suggests that while the overall production of Phe is the same at equal velocities, the introduction of a more complex species (C_{60} vs. coronene) as a projectile increases the number of these detected fragment ions at equal velocities. This may be due to a change in the ionization efficiency in the fragmentation region caused by the presence of projectile fragments.

The coincidental (co-emitted) ion yields are also influenced by the nature of the target surface. The following equations describe the experimental ion yield for a specific case (i.e., a surface composed of one-half Phe_H and one-half Phe_D)

$$Y(\mathrm{Phe_H},\mathrm{Phe_D})_{\exp} = \frac{I(\mathrm{Phe_H},\mathrm{Phe_D})}{N} \qquad \text{Eq. 4-7}$$

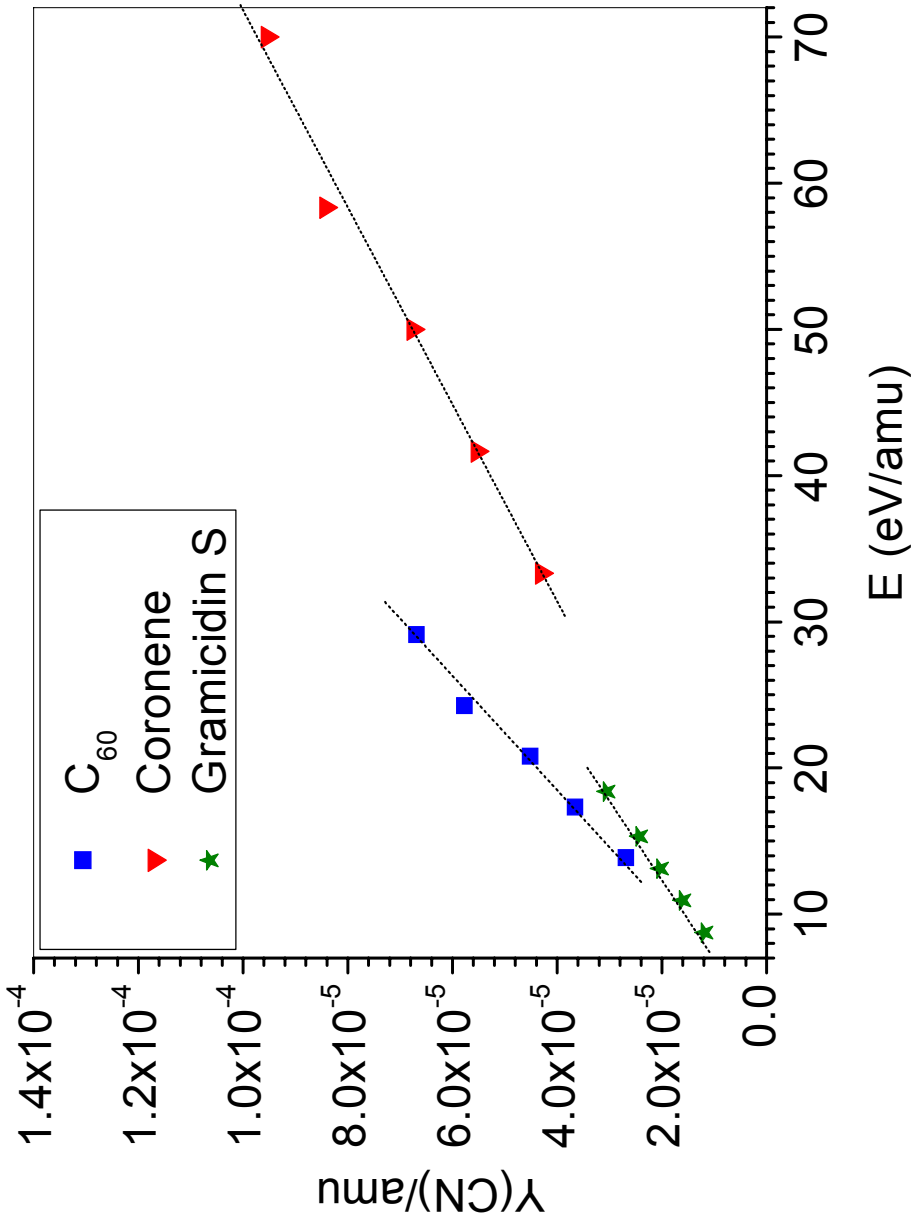

Figure 4-7: Secondary ion yield per amu of CN^- as a function of projectile impact velocity from a phenylalanine sample (dashed lines are to guide the eyes).

where $Y(\mathrm{Phe_H}, \mathrm{Phe_D})_{exp}$ is the ion yield of $\mathrm{Phe_D}$ co-emitted with $\mathrm{Phe_H}$, $I(\mathrm{Phe_H}, \mathrm{Phe_D})$ is the measured number of events when $\mathrm{Phe_D}$ co-emitted with $\mathrm{Phe_H}$, and N is the number of primary ion impacts. The coincidental yield corresponds to a mixed Phe target surface ($\rho = 0.5$), therefore

$$Y(\mathrm{Phe,Phe})_{exp} = Y(\mathrm{Phe_H,Phe_D})_{exp} / \rho^2 \qquad \text{Eq. 4-8}$$

where $Y(\mathrm{Phe, Phe})_{exp}$ is the experimental yield of two co-emitted Phe molecules, $Y(\mathrm{Phe_H}, \mathrm{Phe_D})_{exp}$ is the measured yield of two co-emitted Phe molecules, and ρ is the relative concentration.

Figure 4-8 shows the yield of $\mathrm{Phe_D}$ co-emitted (coincidental) with $\mathrm{Phe_H}$ from coronene, C_{60} and gramicidin S vs. impact energy. The yield for co-emitted ions and impact energy are divided by the atomic mass of the respective projectiles (neglecting hydrogen) for reasons previously mentioned. The coincidental ion (CI) yields per constituent for C_{60} and gramicidin S are comparable at the impact energies examined (Fig. 4-9).

In contrast to the linear dependence $Y(\mathrm{Phe})_{exp}$ vs. energy for single Phe ion emission, the dependence $Y(\mathrm{Phe,Phe})_{exp}$ vs. energy for two Phe ions emissions is nonlinear. Significant differences in projectile efficiencies emerge when comparing the CI yields of coronene and C_{60}. The trend for C_{60} suggests that at equal velocities this projectile is intrinsically more effective for the co-emission of two Phe ions than coronene. This evidence supports a collective collision cascade mechanism, which has been examined with molecular dynamics (MD) simulations. MD simulations examining

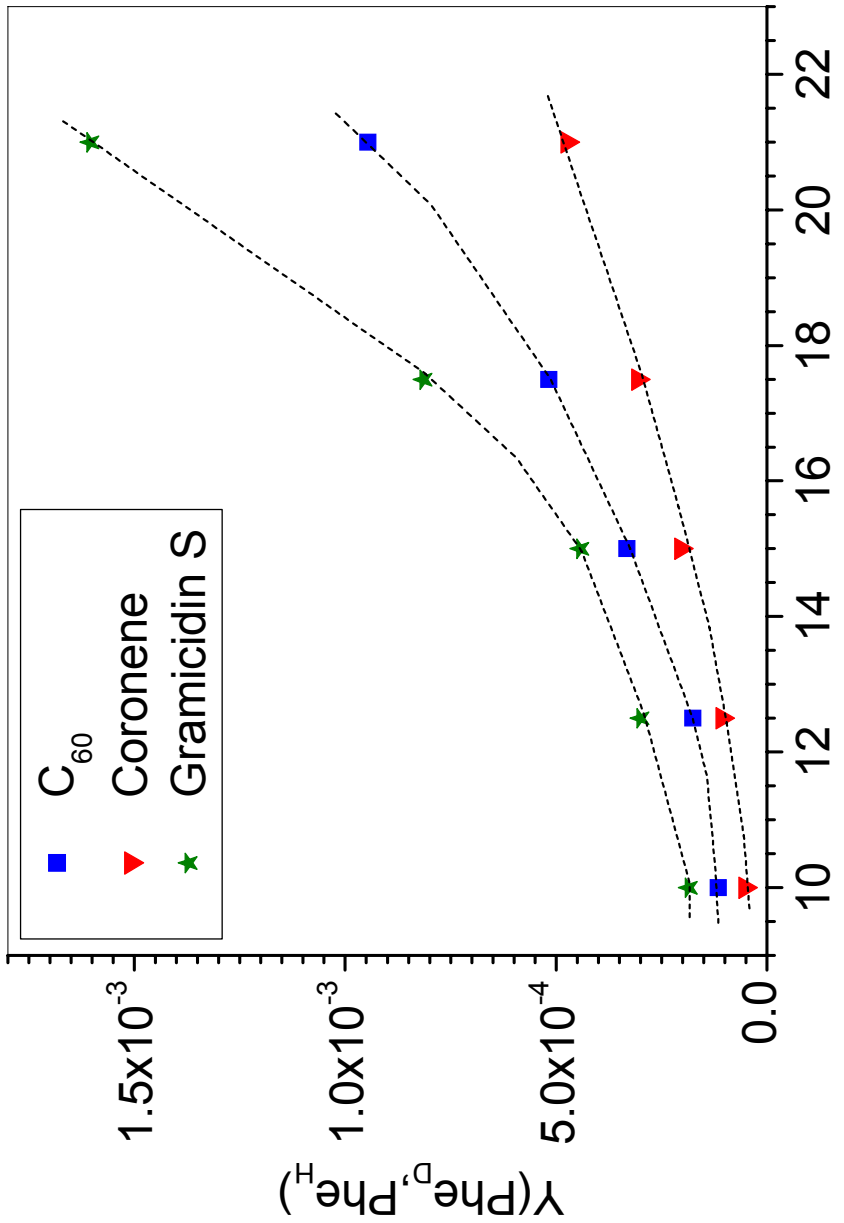

Figure 4-8: Secondary ion yields of Phe_D co-emitted with Phe_H per projectile impact as a function of impact energy. The error for the data varies between ± 12% at 10 keV impact energy to ± 5% at 21 keV impact energy (dashed lines are to guide the eyes).

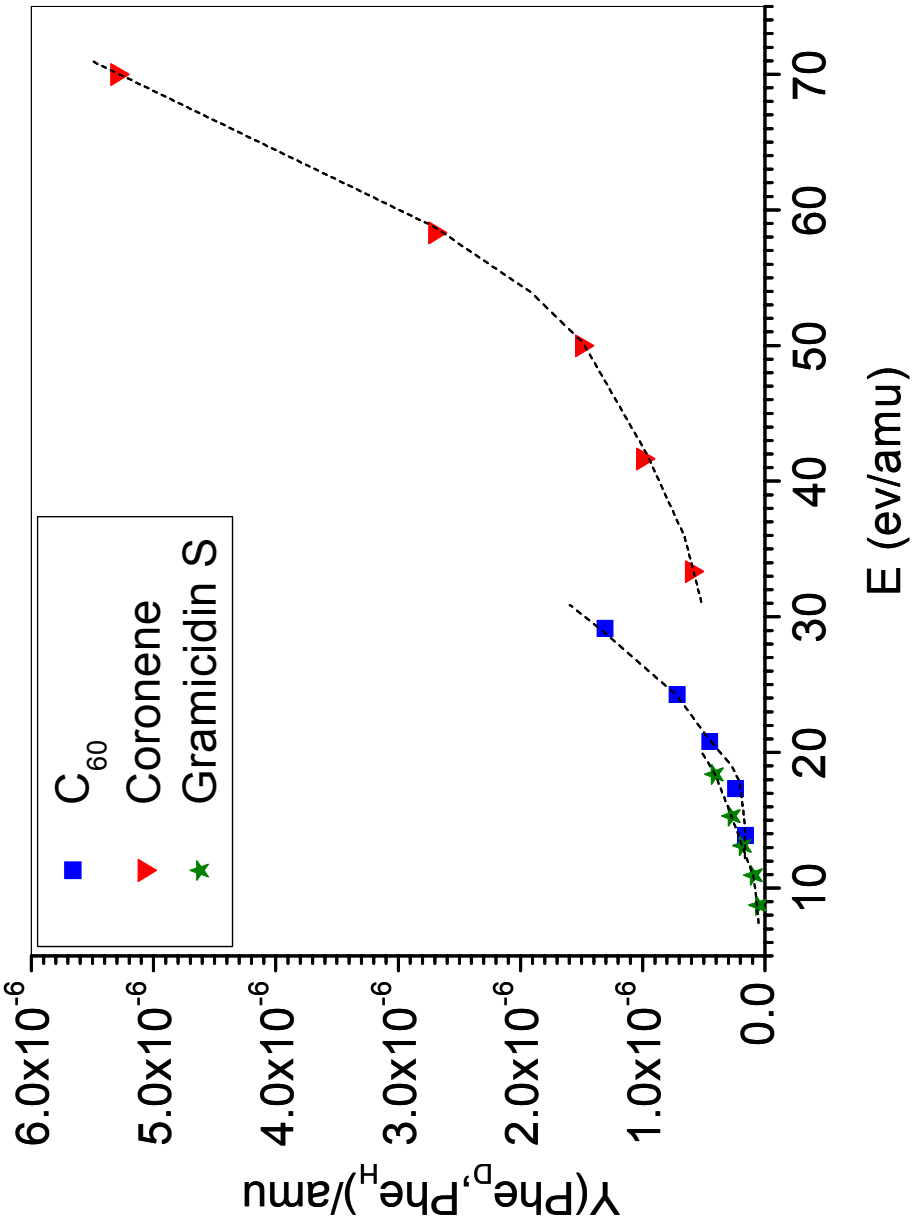

Figure 4-9: Secondary ion yields of Phe_D co-emitted with Phe_H per amu as a function of projectile impact velocity. The error for the data varies between ± 12% at 10 keV impact energy to ± 5% at 21 keV impact energy (dashed lines are to guide the eyes).

keV C_{60} sputtering have shown that the impacts produce multiple overlapping cascades in a relatively shallow volume resulting in the emission of many particles [53].

CHAPTER V

MULTIPLE ION EMISSION

As discussed in Chapter II, increased multiple ion emission has the potential to improve the nano-domain analysis using the event-by-event method. Multiple ion emission from single projectile impacts has been documented in the case of Au_n^m (n = 1-400, m = 1-4) projectiles [92] and massive peptides (amu = 1.1 to 66 kdal, z = 1 – 66) projectiles [75]. In order to measure multiple ion emission with carbon-based projectiles, an effusion-based ion source (described in detail in Chapter III) was built and fitted with an 8 anode secondary ion (SI) detector so that multiple ions of the same mass-to-charge could be detected from single projectile impacts. This chapter examines multiple ion emission from glycine (Gly) with the carbon-based projectiles coronene ($C_{24}H_{12}^+$), C_{60}^+, and $C_{60}F_{40}^+$. The negative secondary ion (SI) mass spectra of glycine produced by 26 keV C_{60}^+ impacts is shown in Figure 5-1 with the representative sample peaks (i.e., CN^-, $[M-H]^-$, and $[M_2-H]^-$) clearly visible in the spectra.

The glycine $[M-H]^-$ yield has a linear dependence with the projectile impact energy (Fig. 5-2). Secondary ion yield (Y_{SI}) is defined as:

$$Y_{SI} = (I_{SI} / N_{PI}) \qquad \text{Eq. 5-1}$$

where I_{SI} is the experimental ion yield minus background, and N_{PI} is the number of primary ion impacts. The $[M-H]^-$ yield/amu with respect to projectile velocity shows a linear increase in yield (i.e., the effectiveness of a constituent atom to produce

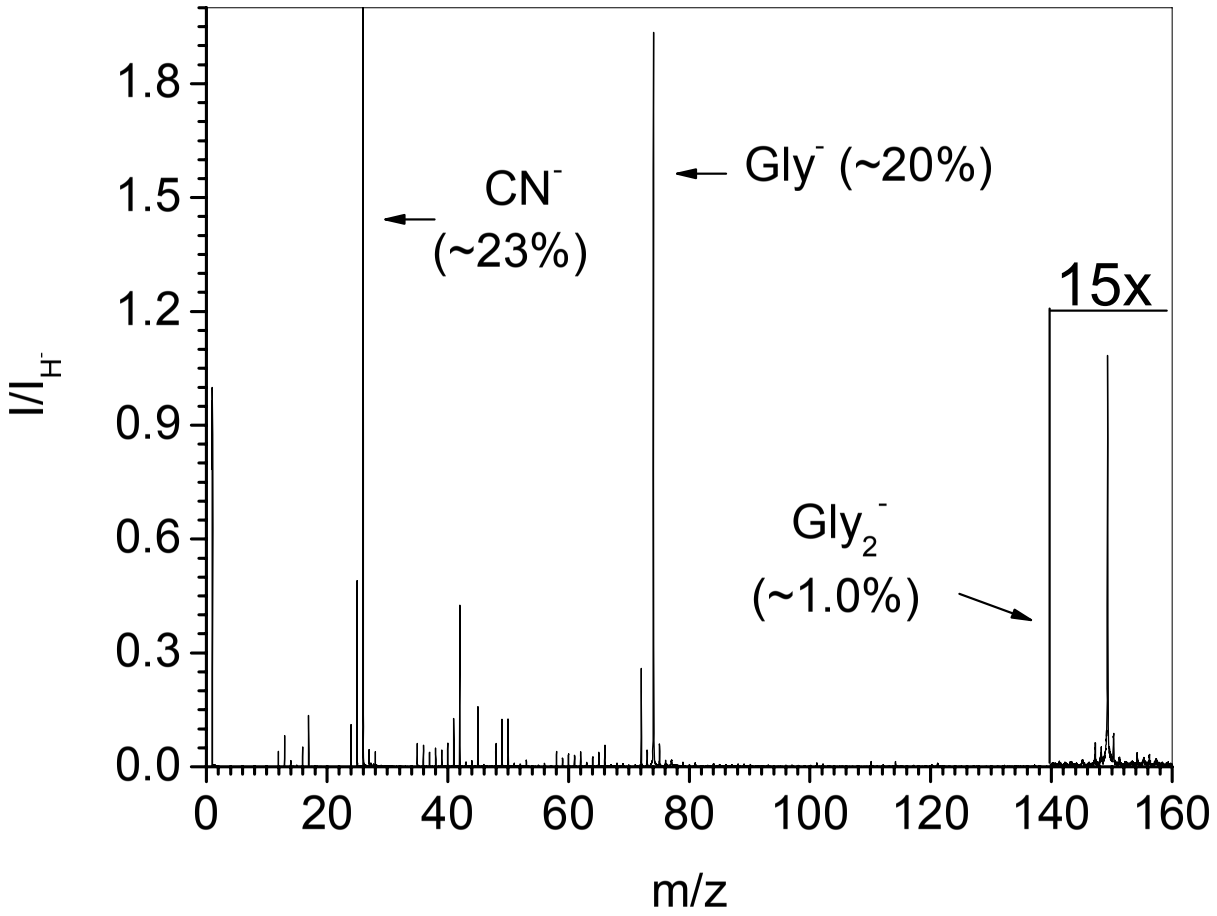

Figure 5-1: Negative secondary ion ToF spectrum produced by 26 keV C_{60}^{+} bombardment on a vapor deposited sample of glycine. The dimer region has been multiplied by a factor of 15 so that the dimer peak may be clearly observed.

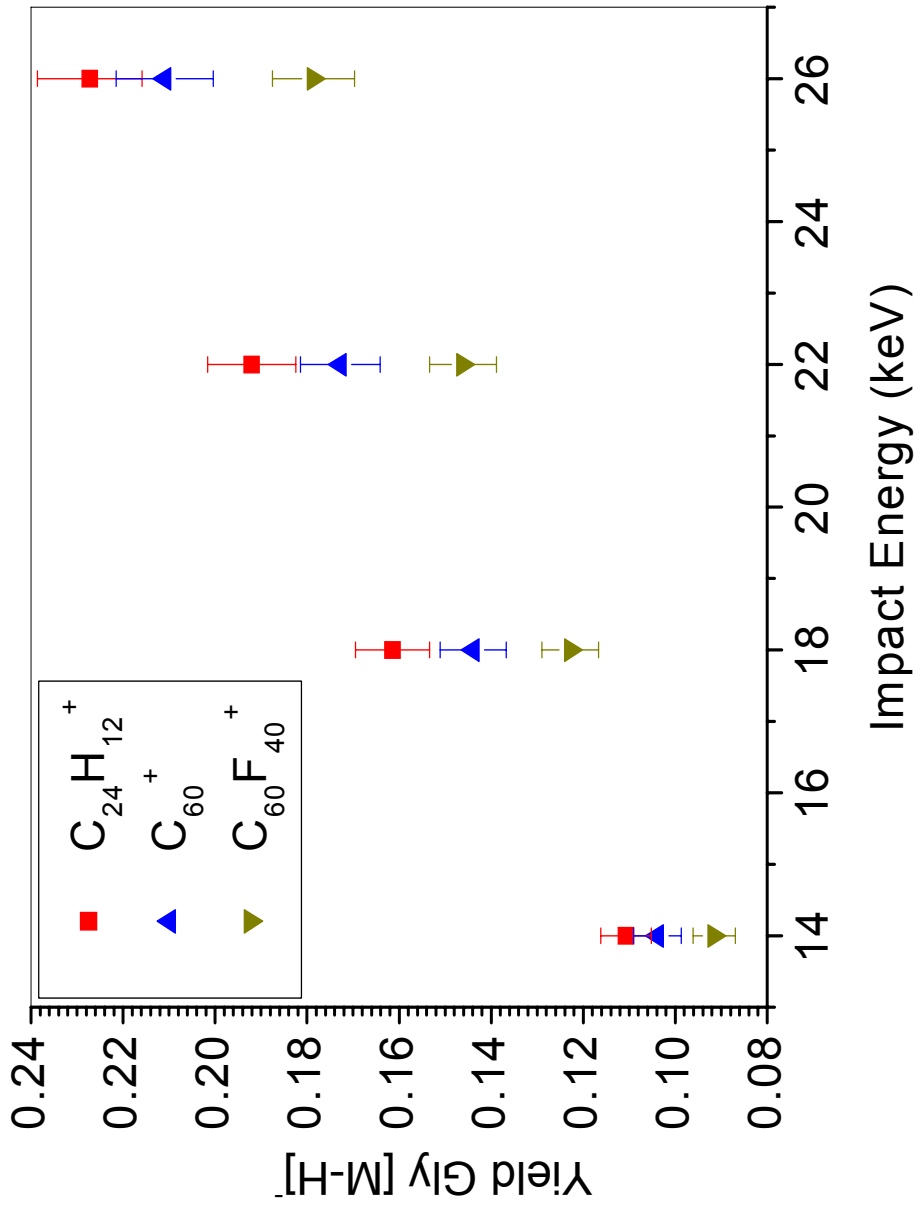

Figure 5-2: The yield of Gly $[M-H]^-$ as a function of projectile impact energy. The relative error is ≤5%.

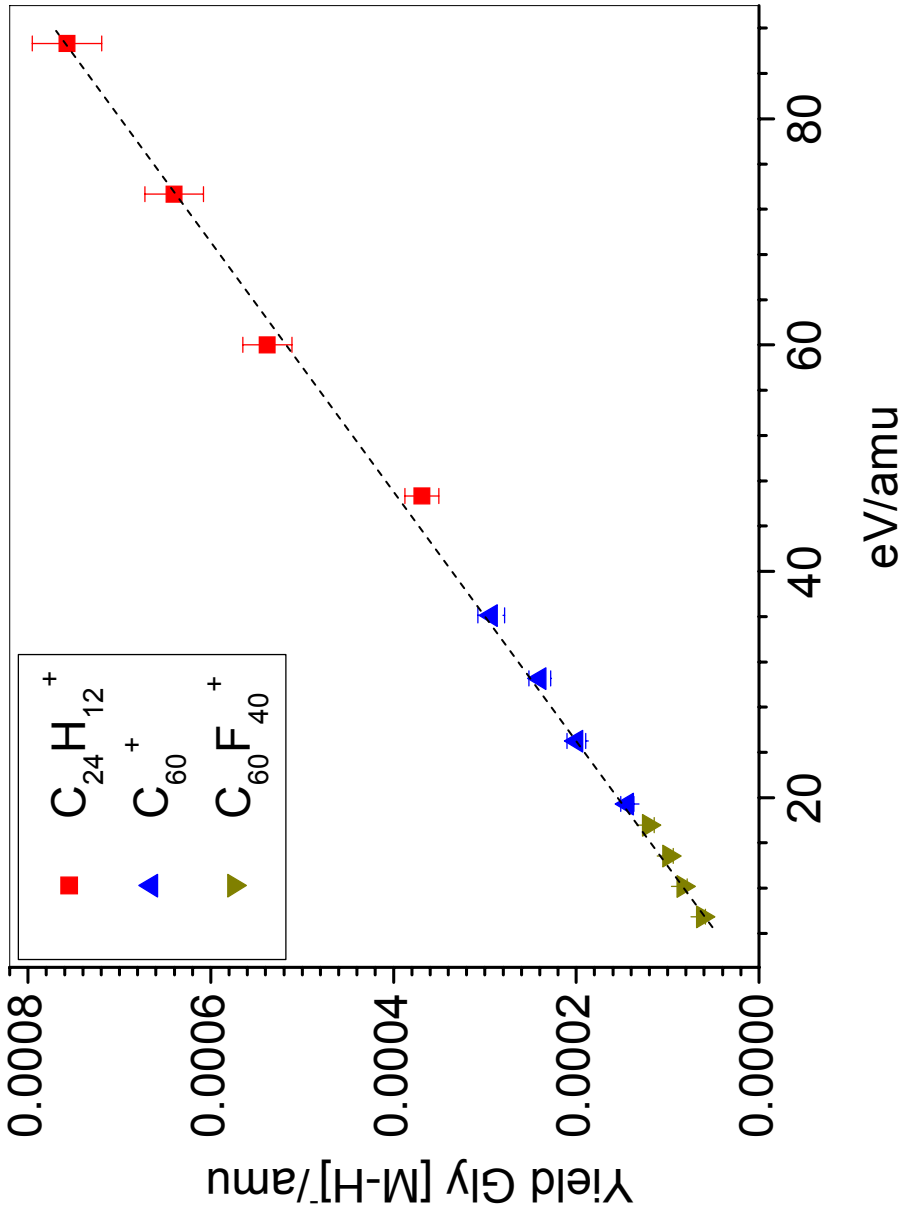

Figure 5-3: The yield of Gly $[M\text{-}H]^-$/amu as a function of projectile velocity. The relative error is ≤5% (dashed line is to guide the eye).

Gly $[M-H]^-$ increases linearly with the projectile velocity) (Fig. 5-3). Similar trends have been observed previously [61-62].

Multiple ion emission occurs with the carbon-based projectile bombardment of glycine. The distribution of the number of any detected secondary ions per projectile impact is referred to as a multiplicity report. Figure 5-4 shows the secondary ion multiplicity reports for four projectiles: coronene ($C_{24}H_{12}^+$), C_{60}^+, $C_{60}F_{40}^+$, and Au^+. The x-axis indicates the number of secondary ions detected per primary ion impact, while the y-axis indicates the probability of detecting SI events with a specific number of secondary ions upon projectile bombardment. For example, the probability of detecting 2 secondary ions under 26 keV C_{60}^+ is ~0.20. The ions can be any combination of 2 ions such as H^- and Gly^-, 2 CN^-, 2 Gly^-, etc. 26 keV carbon-based projectiles produce similar multiplicity reports even though the constituent atoms have different energies (e.g., coronene: ~1 keV/carbon, C_{60}: ~433/carbon, $C_{60}F_{40}$: ~210/carbon and ~333/fluorine). The multiplicity report of 25 keV Au^+ is shown as a reference for atomic projectile bombardment (note: the Au data was taken in a separate system with a similar SI region; therefore, the transmission and detection efficiencies may be different) [111]. The probability of producing 1 secondary ion per event is approximately the same for all the projectiles. However, the cluster projectiles produce 3-4 times more multiple ion emission events compared to the atomic projectile at equal impact energy.

Multiple ion emission is also dependent on the impact energy of the projectile. Figure 5-5 shows the SI emission probability increasing with impact energy. SI events

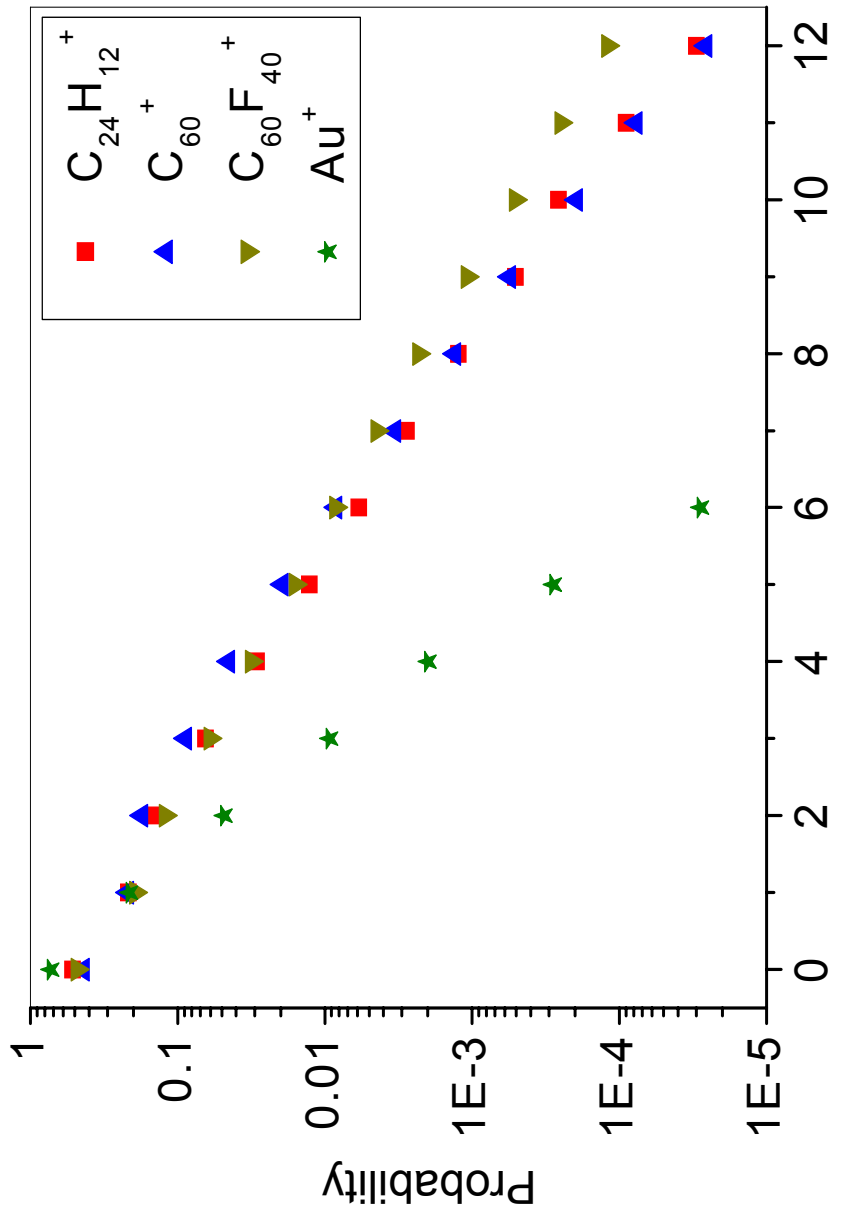

Figure 5-4: Secondary ion multiplicity report (the number of all detected secondary ions per projectile impact) from a glycine target under 26 keV impact energy for coronene ($C_{24}H_{12}^{+}$), C_{60}^{+}, and $C_{60}F_{40}^{+}$. 25 keV Au^{+} is shown as a reference for an atomic projectile (note: the Au data was taken in a different system; therefore the transmission and detection efficiencies may be different from the carbon-based projectiles [111]).

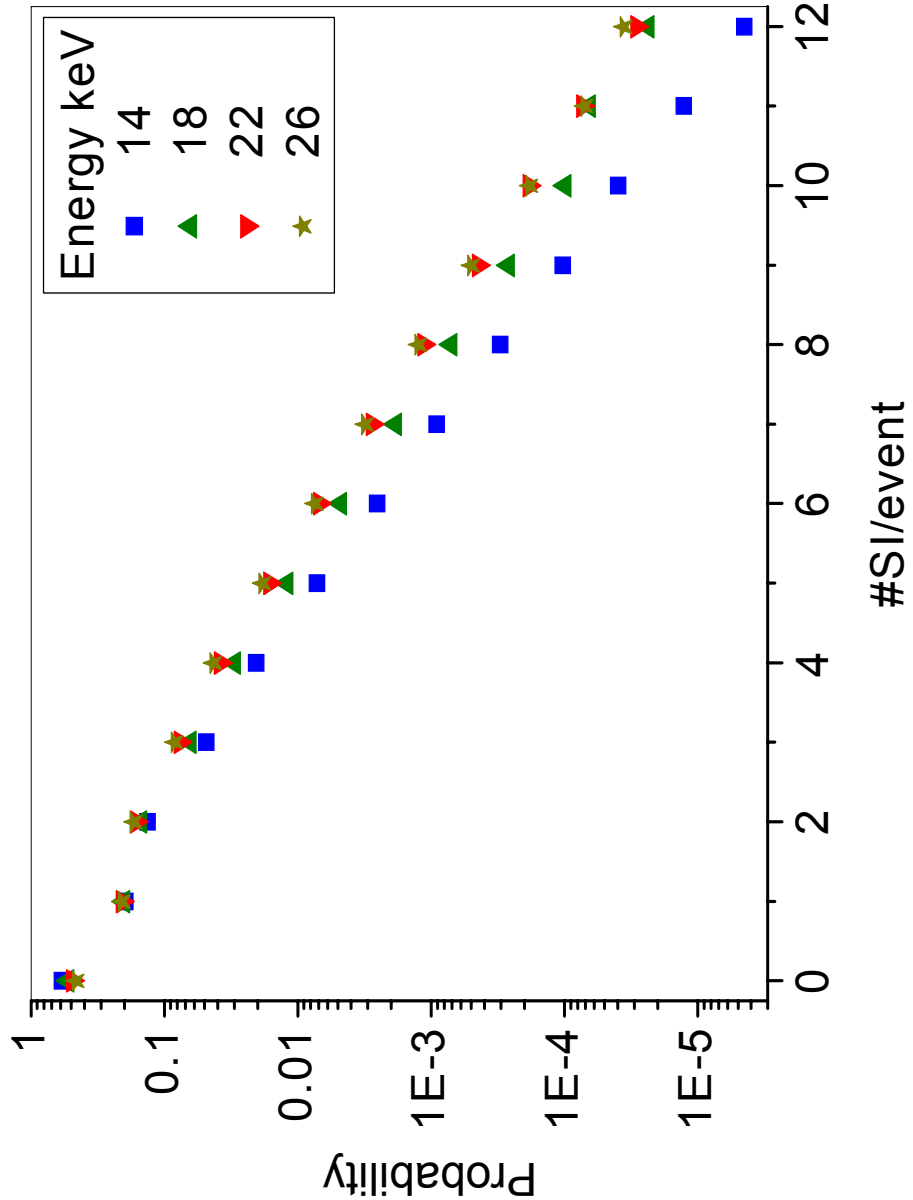

Figure 5-5: Secondary ion multiplicity report (the number of all detected SI per C_{60}^{+} impact) from a glycine sample at various impact energies.

in which multiple secondary ions are emitted compose ~21% of the 14 keV C_{60}^+ bombardment events compared to ~33% of 26 keV C_{60}^+ bombardment on glycine.

Nano domain analysis using the event-by-event method is only practical if the co-emitted ions are representative of the surface. Therefore, multiple ion emission of representative ions is examined. The SI distribution for glycine $[M-H]^-$ produced by C_{60}^+ at various impact energies and 25 keV Au^+ is shown in Figure 5-6. The x-axis shows the number of glycine detected per projectile impact, while the y-axis shows the probability of detecting glycine emission events. The trend is similar to the SI multiplicity reports for all ions, a monotonic decline with increasing numbers of glycine per event. Higher impact energies, increase the probability of multiple glycine $[M-H]^-$ emission, particularly when three or more glycines per event are detected. Over the energy range examined (14-26 keV), the probability of detecting events in which 1 glycine ion per event increases by ~ 60%, while the probability of detecting 7 glycine ions per event increases by ~ 7 times. 26 keV C_{60}^+ impacts produce ~3 times more events in which glycine molecules are emitted than 25 keV Au^+ impacts. Additionally, 26 keV C_{60}^+ impacts produce ~40 times more events in which multiple glycine molecules are detected than 25 keV Au^+ impacts.

The total material disturbed by the projectile in the sample (i.e., sputtered, fragmented, or shifted material [14]) further illustrates the increased efficiency of cluster projectiles over atomic projectiles. A 25 keV Au^+ projectile perturbs a volume ~5 times greater than a 26 keV C_{60}^+ projectile based on the following criteria: the volume disturbed by 26 keV C_{60}^+ is approximated by a half sphere with a radius of ~5 nm; the

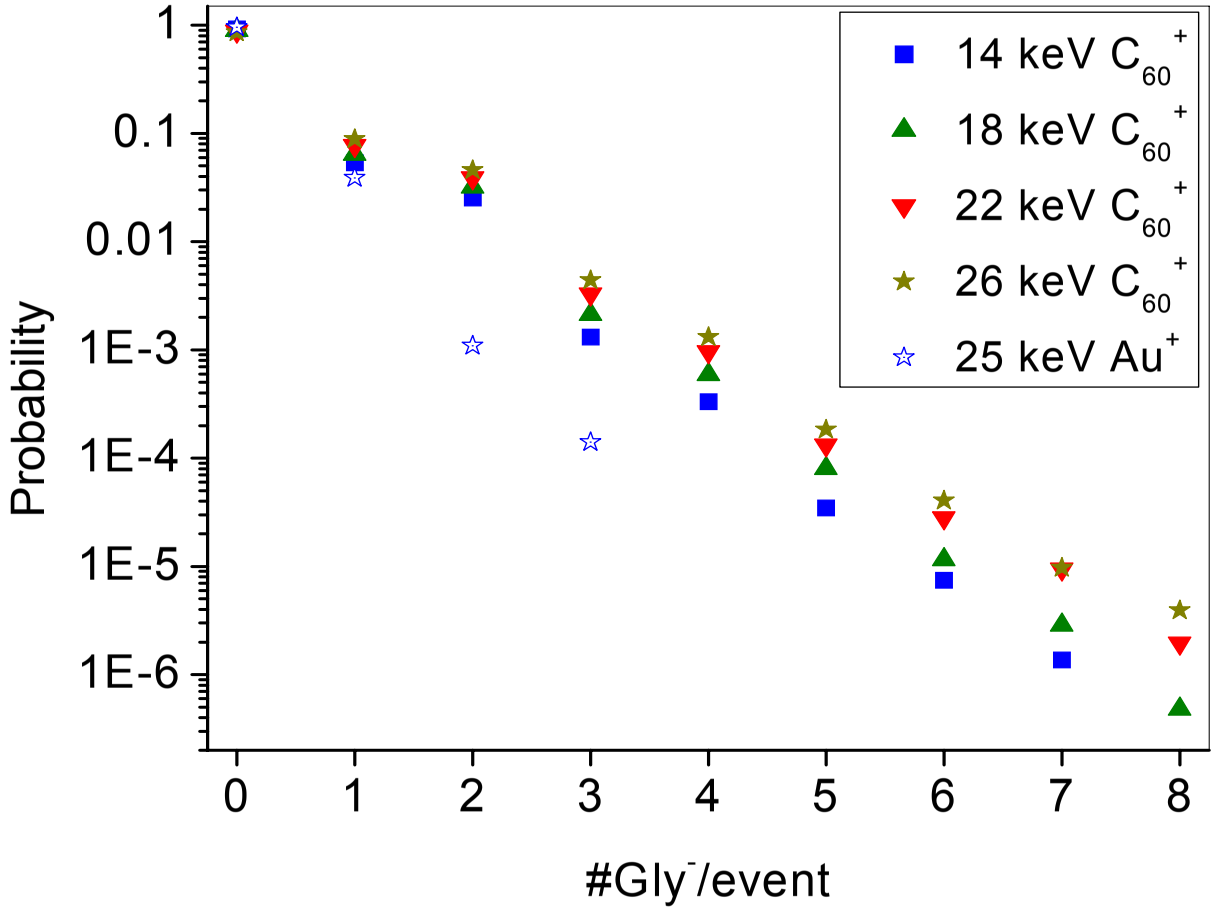

Figure 5-6: Secondary ion distribution for glycine $[M-H]^-$ (the number of glycine $[M-H]^-$ detected per projectile impact) at various impact energies on a glycine sample from 14, 18, 22, and 26 keV C_{60}^+ and 25 keV Au^+ bombardment (note: the Au data was taken in a different system; therefore the transmission and detection efficiencies may be different from the C_{60}^+ projectiles [111]).

volume disturbed by 25 keV Au^+ projectile is approximated by a cylinder with a 5 nm radius and 20 nm height (note: height is based on a TRIM calculation of the average penetration depth of 25 keV Au^+ on an glycine surface with a density of 1.6 g/cm^3). The estimated number of glycine molecules perturbed by a 26 keV C_{60}^+ projectile and 25 keV Au^+ projectile are ~3 e3 ± 3e2 and ~2e4 ± 2e3, respectively. With a detection limit of 10 counts under the glycine $[M-H]^-$ peak, ~50 projectiles of 26 keV C_{60}^+ are necessary to reach the detection limit, while ~250 projectiles of 25 keV Au^+ are needed. This corresponds to ~25 times the material perturbed by Au^+ projectiles compared to C_{60}^+ projectiles. For multiple glycine emission, the detection limit is reached with ~100 projectiles of 26 keV C_{60}^+, while ~ 1000 projectiles of 25 keV Au^+ are required, which corresponds to ~50 times the material perturbed by Au^+ projectiles compared to C_{60}^+ projectiles.

The SI distribution of the fragment ion, CN^-, is similar to the SI distribution of Gly $[M-H]^-$ (Fig. 5-7). This shows that multiple secondary ion emission of other sample specific ions does occur in addition to the molecular ion.

As discussed earlier, Figure 5-3 shows the yield of Gly $[M-H]^-$/amu as a function of projectile velocity. This figure is a summation of all secondary ion events and shows each projectile to be equivalent at equal velocities. However, by monitoring multiple ion emission, it is possible to unfold additional information about the emission process under carbon cluster bombardment. In Figures 5-8 and 5-9, the yield of Gly $[M-H]^-$/amu as a function of projectile velocity has been plotted in cases where 1, 2, 3, and 4 Gly $[M-H]^-$ are detected per projectile impact. It is evident that differences exist between the

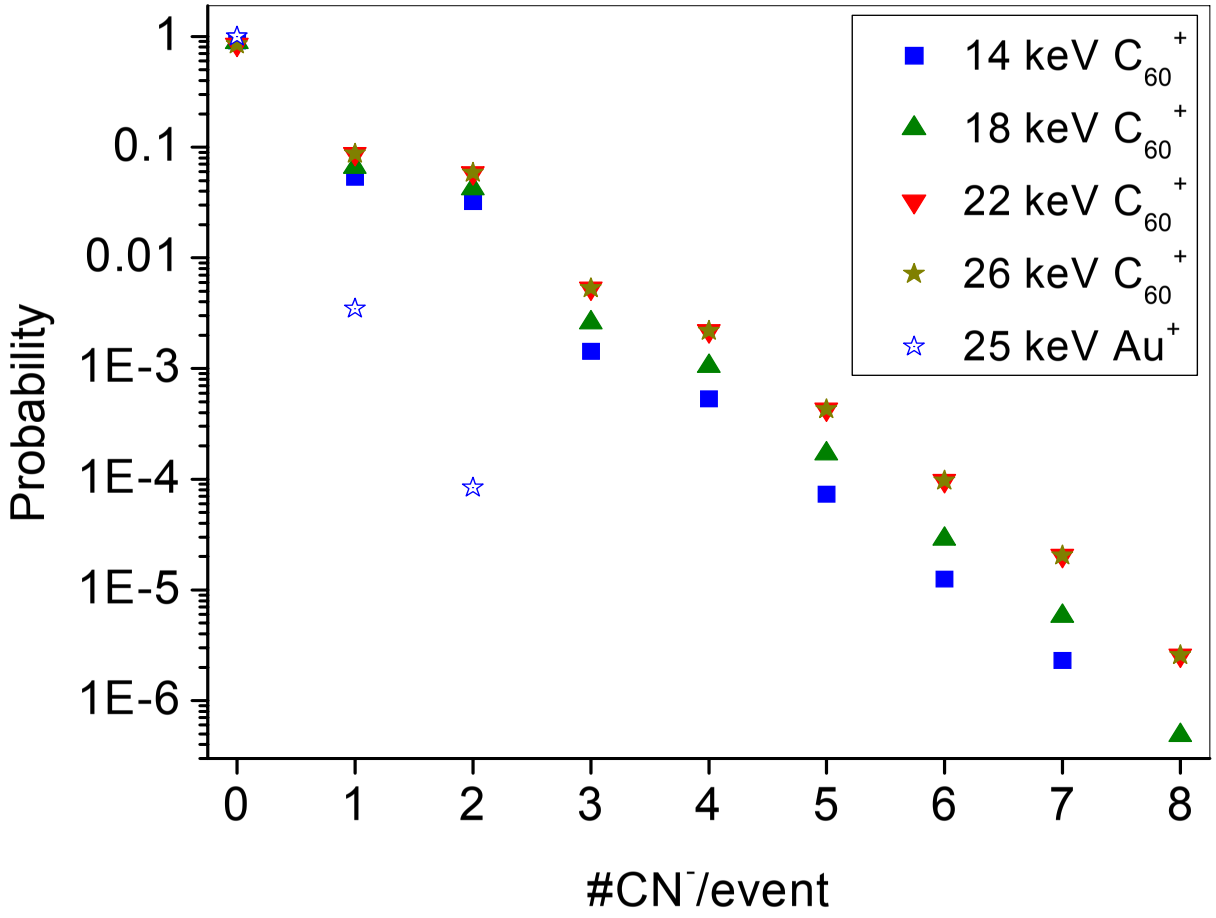

Figure 5-7: Secondary ion distribution of the number of CN^- detected per projectile impact at various impact energies on a glycine sample from 14, 18, 22, and 26 keV C_{60}^+ and 25 keV Au^+ (note: the Au data was taken in a different system; therefore the transmission and detection efficiencies may be different from the C_{60}^+ projectiles [111]).

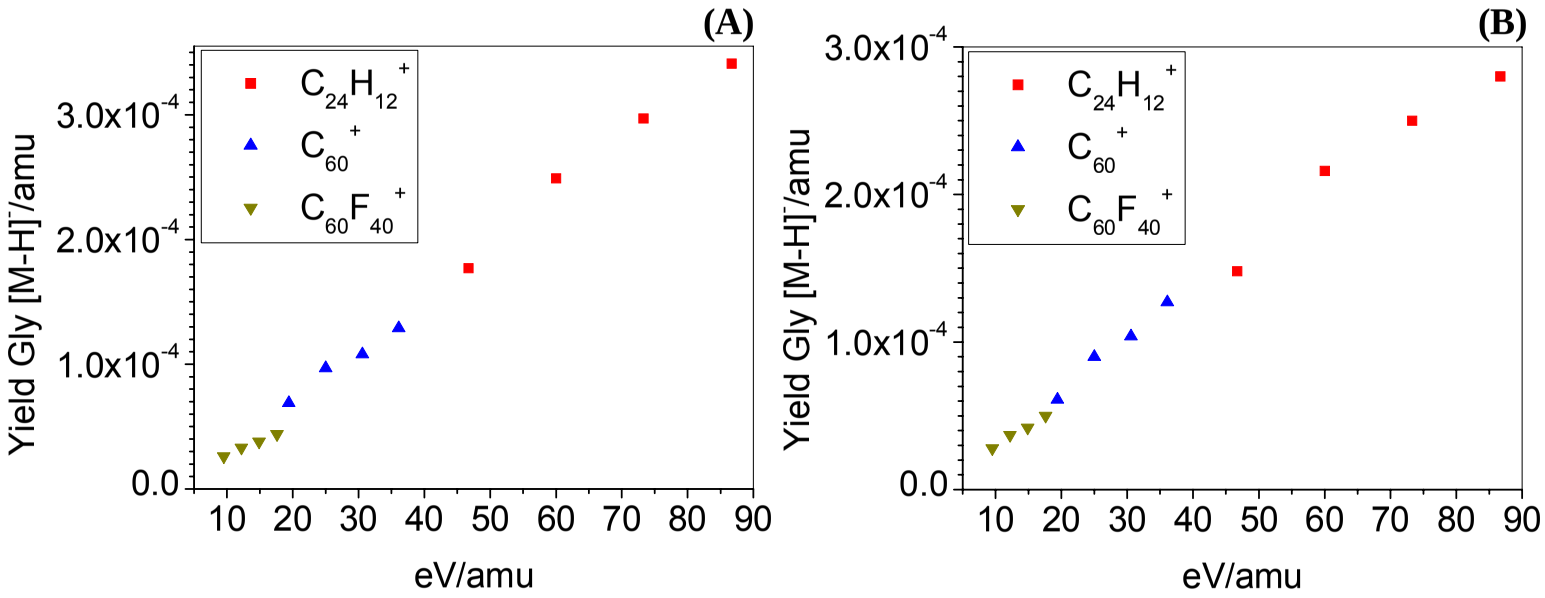

Figure 5-8: The yield of Gly $[M-H]^-$/amu as a function of projectile velocity for (A) events in which 1 Gly $[M-H]^-$ is detected, (B) events in which 2 Gly $[M-H]^-$ are detected.

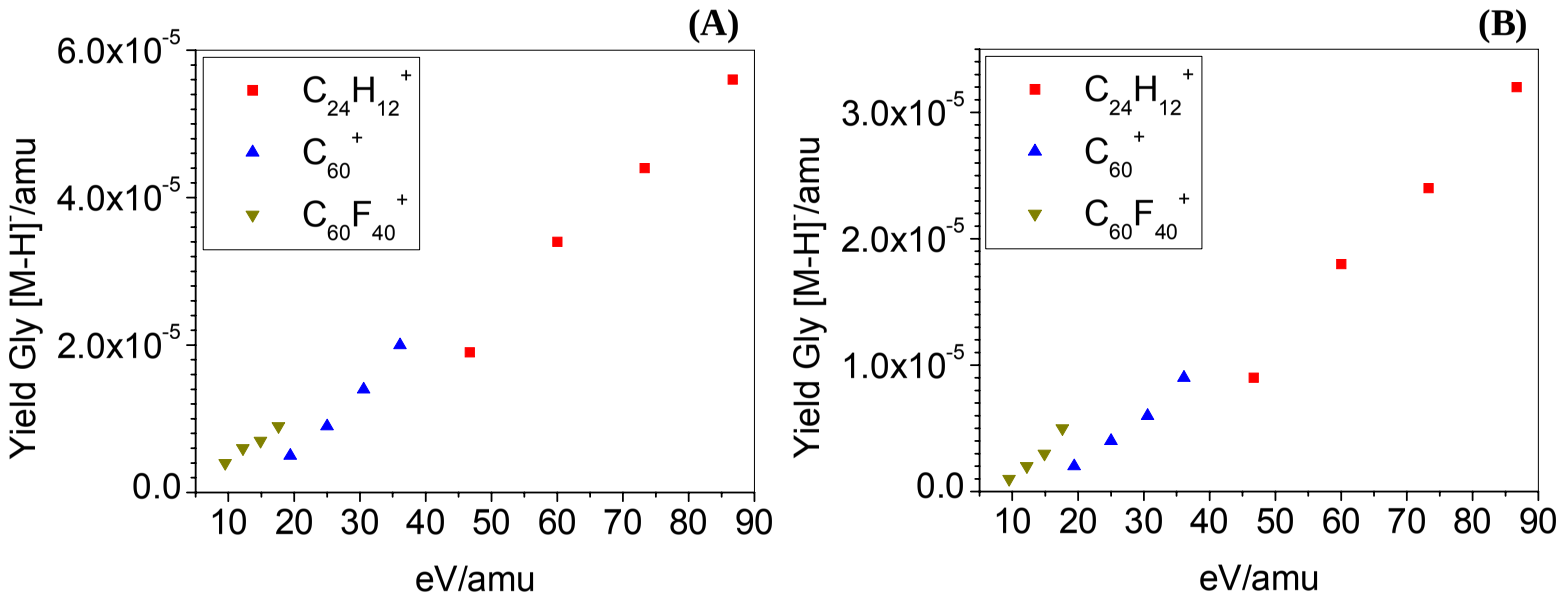

Figure 5-9: The yield of Gly $[M-H]^-$/amu as a function of projectile velocity for (A) events in which 3 Gly $[M-H]^-$ are detected, (B) events in which 4 Gly $[M-H]^-$ are detected.

projectiles as the yield of Gly $[M-H]^-$/amu are not aligned in all four cases, particularly in cases where 3 and 4 Gly $[M-H]^-$ are detected per projectile impact.

Rickman and co-workers examined the emission of the Phe $[M-H]^-$ from a phenylalanine surface using 28.6-134.6 keV Au_9^+ and Au_{400}^{4+}. The flight times of the phenylalanine [M-H] ions shifted towards shorter flight times as the number of co-emitted Phe phenylalanine [M-H] ions per projectile impact increased (i.e., the flight time of Phe $[M-H]^-$ was longer in instances when one molecular ion was detected than when two and three co-emitted molecular ions were detected). The shift in flight times was attributed to a dependence of the ionization probability on the kinetic energy of the emitted particles (i.e., higher kinetic energy particles have greater ionization probabilities) [92].

The efficiency of a cluster constituent atom to produce Gly $[M-H]^-$ when 1, 2, 3, and 4 Gly $[M-H]^-$ are detected is shown in Figures 5-8 and 5-9. The efficiency of a constituent atom from $C_{24}H_{12}^+$, C_{60}^+, and $C_{60}F_{40}^+$ projectiles are approximately equivalent at equal velocities in cases where 1or 2 Gly $[M-H]^-$ are detected (i.e., the yield of Gly $[M-H]^-$/amu from $C_{24}H_{12}^+$, C_{60}^+, and $C_{60}F_{40}^+$ projectiles are aligned). In instances where 3 or 4 Gly $[M-H]^-$ are detected, the constituent atoms are not equivalent at equal velocities (i.e., the yield of Gly $[M-H]^-$/amu from $C_{24}H_{12}^+$, C_{60}^+, and $C_{60}F_{40}^+$ projectiles are not aligned). The differences in efficiency when 1, 2, 3, and 4 Gly $[M-H]^-$ are detected may be the result of a dependence of the ionization probability on the kinetic energy of the emitted particles. The kinetic energy imparted to the Gly molecule appears to increase with the size of the projectile.

The effectiveness of a constituent atom to produce Gly $[M-H]^-$ increases linearly with the projectile velocity for all Gly $[M-H]^-$ events (Fig. 5-3). The collective linear trend (Fig. 5-3) does not show deviations from linearity similar to 3 and 4 Gly $[M-H]^-$ events (Fig. 5-9) because these events comprise <10 % of the total Gly $[M-H]^-$ yield. Therefore, 3 and 4 Gly $[M-H]^-$ events affect the collective linear trend minimally.

CHAPTER VI

CN^- EMISSION UNDER CARBON CLUSTER BOMBARDMENT

Polyatomic primary ion source have expanded the utility of SIMS by improving sensitivity [6, 21]. SIMS analyses have primarily focused on molecular ions or large fragments to identify species present in a sample. However, a smaller fragment, CN^-, is of interest since it is abundantly produced from biological samples. CN^- can be used as a marker if C and/or N are isotopically labeled. Biological SIMS imaging experiments use isotopically labeled species such as ^{13}C or ^{15}N glycine molecules to investigate transport and metabolism characteristics [4, 112-115]. These experiments are carried out using atomic projectiles which do not produce high secondary ion (SI) yields of CN^-. Cluster projectiles could improve this type of analysis.

The $[M-H]^-$ and CN^- yields for various organic molecules produced by 34 keV Au^+ and 23 keV C_{60}^+ are shown in Table 6-1. For atomic projectiles, the CN^- yield can be increased by bombarding the sample prior to analysis (i.e., pre-implantation). The pre-implanted projectiles cause fragmentation of the sample. This produces additional smaller fragments (i.e., CN), which are analyzed, while the molecular ion yields is reduced due to the fragmentation [4, 112].

The $[M-H]^-$ and CN^- yields from Gly samples are increased by ~ 4 and ~ 80 times respectively using 23 keV C_{60}^+ compared to 34 keV Au^+. Under C_{60}^+ bombardment, the $[M-H]^-$ yield decreases with increasing mass of the molecular ion. However, the CN^- yields produced by C_{60}^+ bombardment remain between 10-25 %. For example under 23

Table 6-1: The $[M-H]^-$ and CN^- yields of various samples produced by 23 keV C_{60}^+ or 34 keV Au^+ (note *: the Au data was taken in a different system; therefore the transmission and detection efficiencies may be different from the C_{60} data [118]).

Projectile	Sample	nom. M.W.	[M-H]-	CN-
34 keV Au*	Gly	75	0.0392	0.0026
34 keV Au (implanted)*	Gly	75	0.0152	0.0048
23 keV C60	Gly	75	0.1747	0.2055
23 keV C60	Pro	115	0.1627	0.1541
23 keV C60	His	155	0.1086	0.2724
23 keV C60	Gua	151	0.0678	0.2786
23 keV C60	Arg-Phe	321	0.0029	0.1371
23 keV C60	Trp-Trp	390	0.0462	0.2506
23 keV C60	Gramicidin S	1141	0.0005	0.1698

keV C_{60}^+, the ratio of $CN^-/[M-H]^-$ for Gly is ~1, while the $CN^-/[M-H]^-$ ratio for gramicidin S is ~340. This suggests that in the case of Gly, CN^- or $[M-H]^-$ would be equally affective as sample identifiers, while for gramicidin S, CN^- would be more effective by two orders of magnitude. In the case of gramicidin S, the molecule has 12 possible nitrogen atoms to contribute to the overall CN^- yield. If a single nitrogen is labeled, the molecular marker signal would likely decrease proportionally to $1/12^{th}$ the value displayed in Table 6-1, which is still ~20 times higher than the gramicidin S $[M-H]^-$ yield.

In instances where both CN^- and $[M-H]^-$ are available for analysis, the question arises, why expend additional effort to use labeled molecules when identification can be achieved with the molecular ion? One reason is that CN^- emission may occur independent of matrix effects that influence $[M-H]^-$ emission (e.g., matrix enhanced SIMS). An example of CN^- emission occurring independent of matrix effects will be discussed in Chapter VII. Briefly, CN^- emission from various mixtures of gramicidin S and sinapic acid was found to occur independent of matrix effects. If independent CN^- emission occurs in other matrices, the possibility exists to use CN^- for quantification of analytes in various matrices. However, if CN^- is to be used as a tool for quantification, the emission properties of CN^- under cluster bombardment must be known.

We have carried out experiments with 14-26 keV projectiles of $C_{24}H_{12}^+$, C_{60}^+, and $C_{60}F_{40}^+$ examining various samples to asses the role of nitrogen in CN^- production (i.e., the available number of nitrogen) and the nature of CN^- emission (i.e., direct emission or recombination/rearrangement). Additionally, the role of molecular structure

in other characteristic emission (i.e., $[M-H]^-$ and $[M_2-H]^-$) was examined. The mass spectra of Pro and His produced by 26 keV C_{60}^+ are shown in Figure 6-1. The molecular structures of the samples are shown in Figure 6-2.

The $[M-H]^-$ yields of each sample have a linear dependence with projectile impact energy (Fig. 6-3). Similar linear dependencies have been observed previously under carbon cluster bombardment [61-62]. The order of the $[M-H]^-$ yield (i.e., the yield of $[M-H]^-$ from highest to lowest yield for each sample at a given impact energy) is inversely related to molecular weight for Gly, Pro, and His. The Gua $[M-H]^-$ yield is lower than His $[M-H]^-$ even though the molecular weight of His is larger than Gua. This inversion can be explained by the molecular structure. Glycine, Pro, His molecules readily loose protons from the carboxylic acid moiety to produce anions. Gua does not contain such a site, which may lower the Gua $[M-H]^-$ ionization probability.

Figure 6-4 shows the yield dependence of the molecular dimer $[M_2-H]^-$ with respect to C_{60}^+ impact energy. As with the molecular ions, there is a linear yield increase with increased impact energy. However, the order of the molecular dimer yield is different from the $[M-H]^-$ yield order. The yield for the Pro and Gly dimers are inverted compared to the yields of the monomers. Similarly, the yields of the His and Gua dimers have an inversion in the order of yields for the monomer and dimer. The reason for this change is order is unclear. The dimer ion stability may cause the inversions seen in the dimer yield order.

The yield dependences of CN^- from Gly, Pro, His, and Gua with respect to C_{60}^+ impact energy is shown in Figure 6-5. The CN^- yields are linear over the energy range

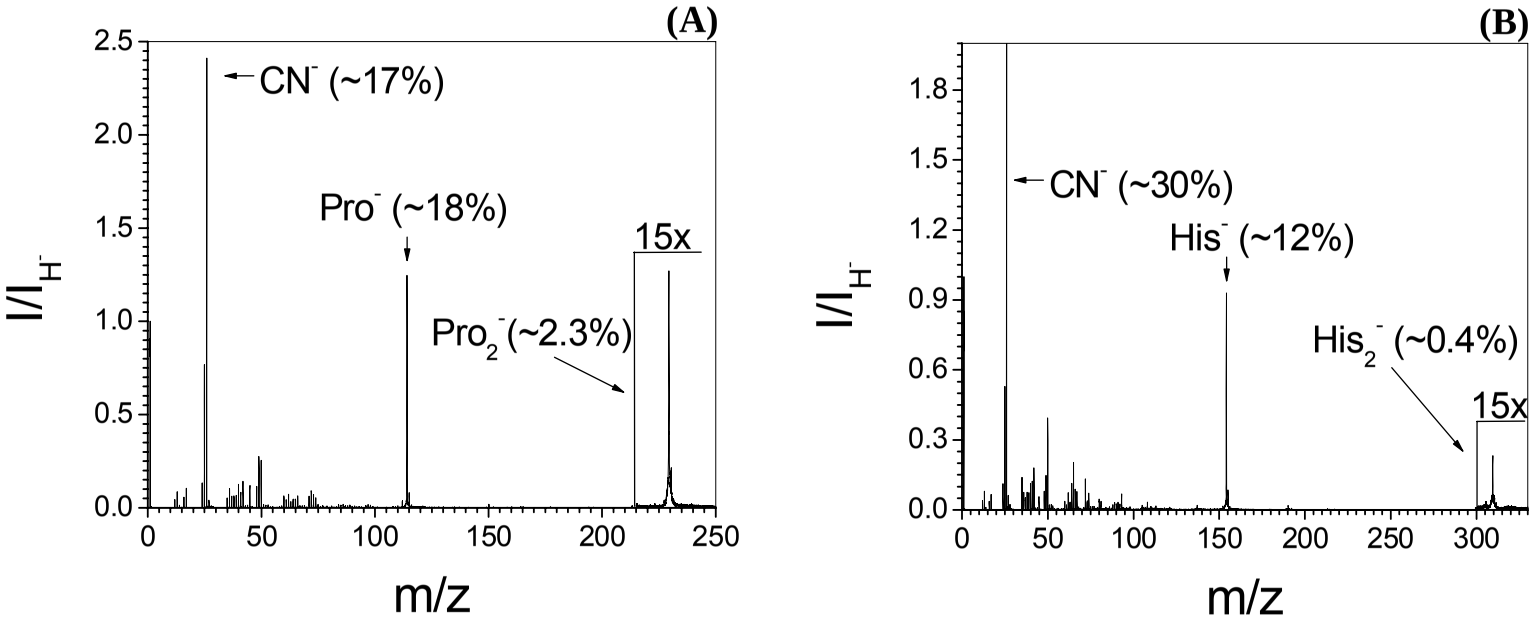

Figure 6-1: Negative secondary ion ToF spectra produced by 26 keV C_{60}^+ bombardment on vapor deposited samples of (A) proline and (B) histidine. The dimer regions of each sample has been multiplied by a factor of 15 so that the dimer peak may be clearly observed.

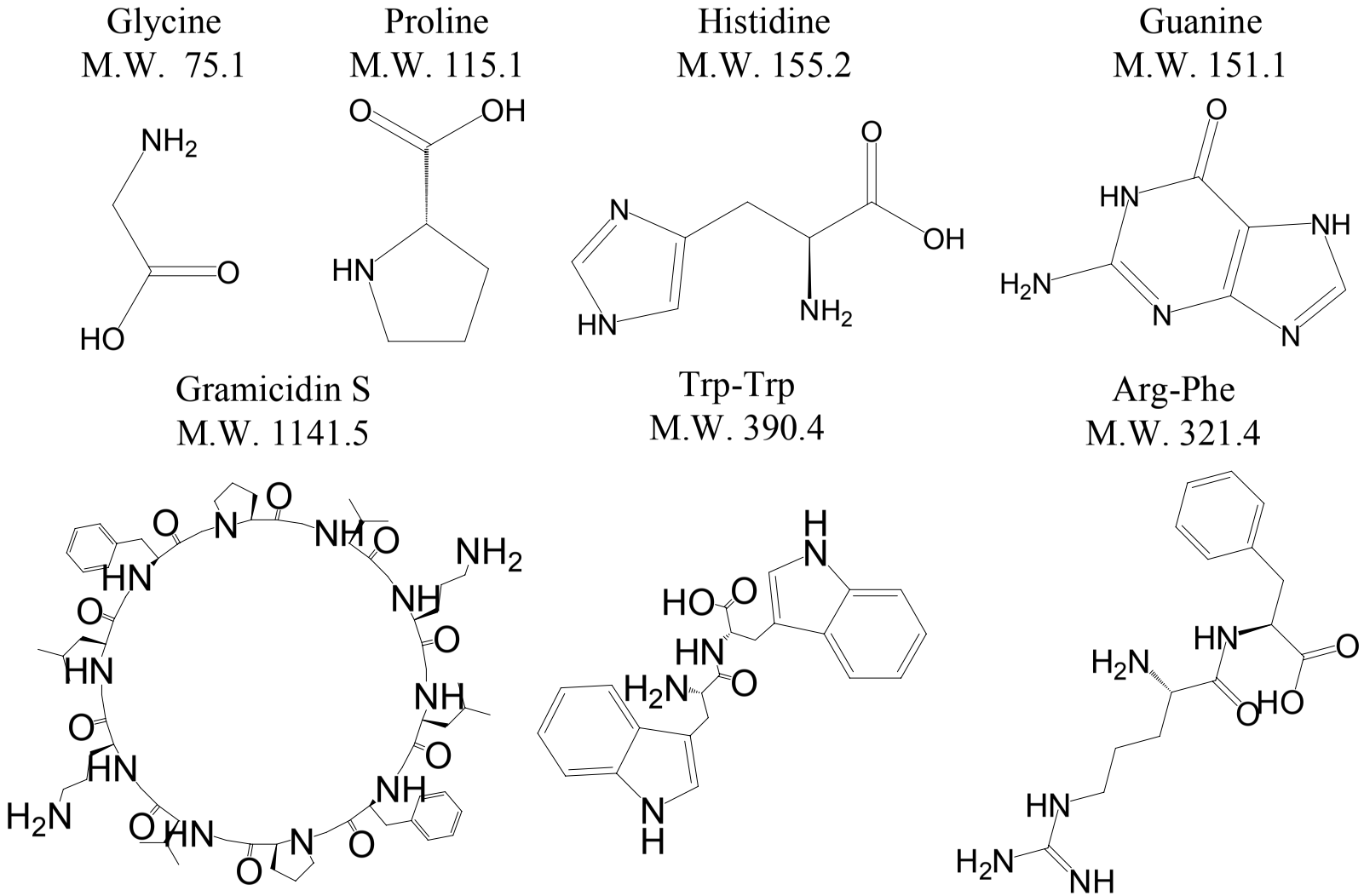

Figure 6-2: The structures and molecular weights of glycine, proline, histidine, guanine, gramicidin S, tryptophan-tryptophan, and arginine-phenylalanine.

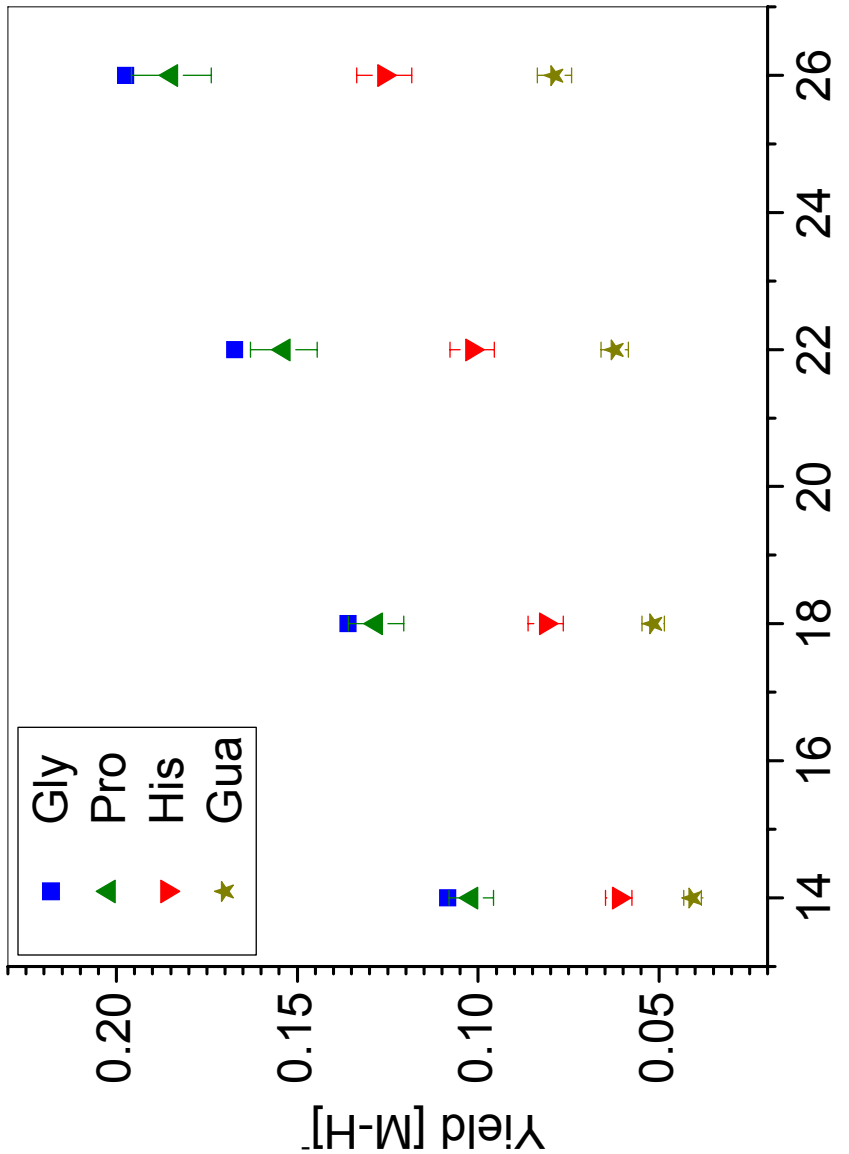

Figure 6-3: The yield of $[M-H]^-$ as a function of the C_{60}^+ impact energy. Error bars are 6% relative error. The error bars for Gly have been removed for aesthetic purposes.

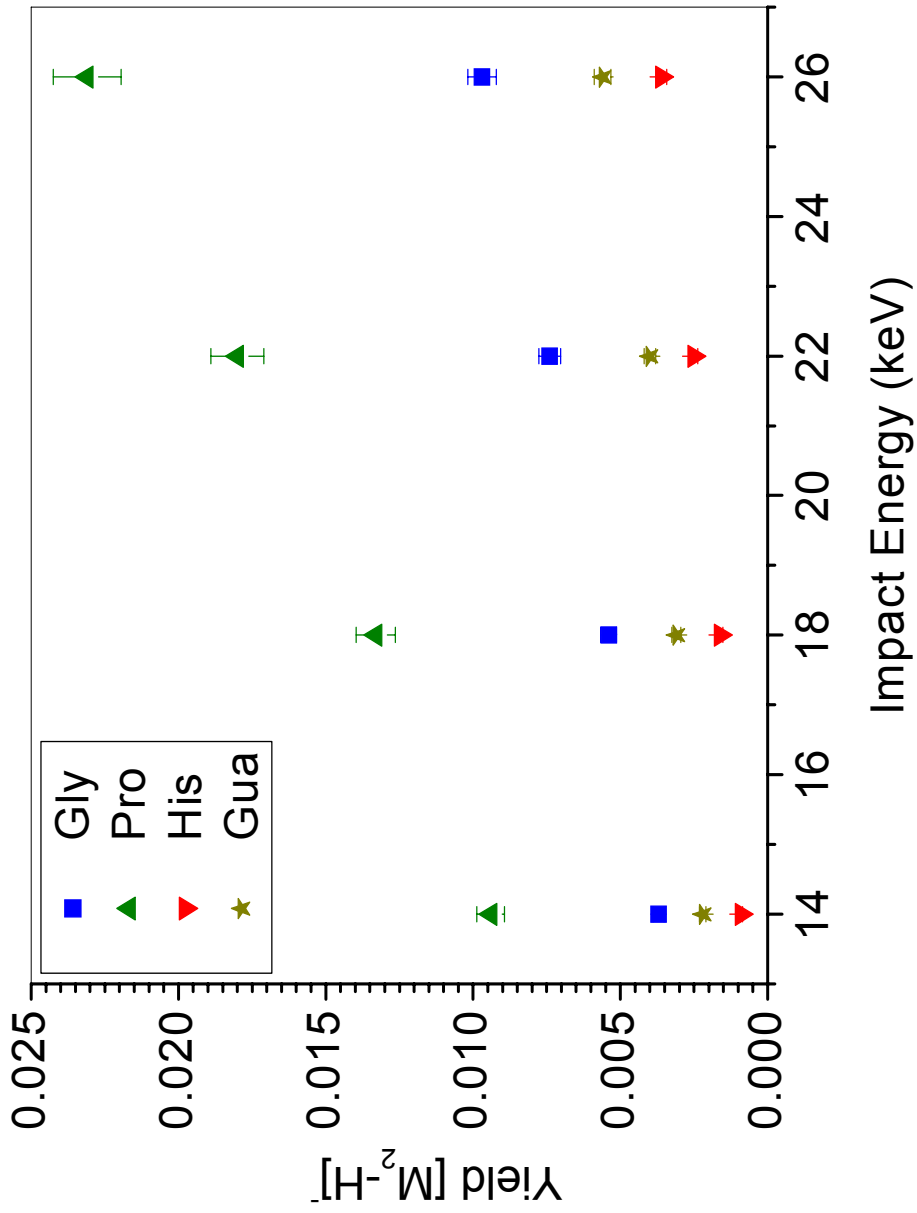

Figure 6-4: The yield of $[M_2\text{-}H]^-$ as a function of the C_{60}^+ impact energy. Error bars are 6% relative error. For points where error bars are not seen, the symbol is larger than the error bar.

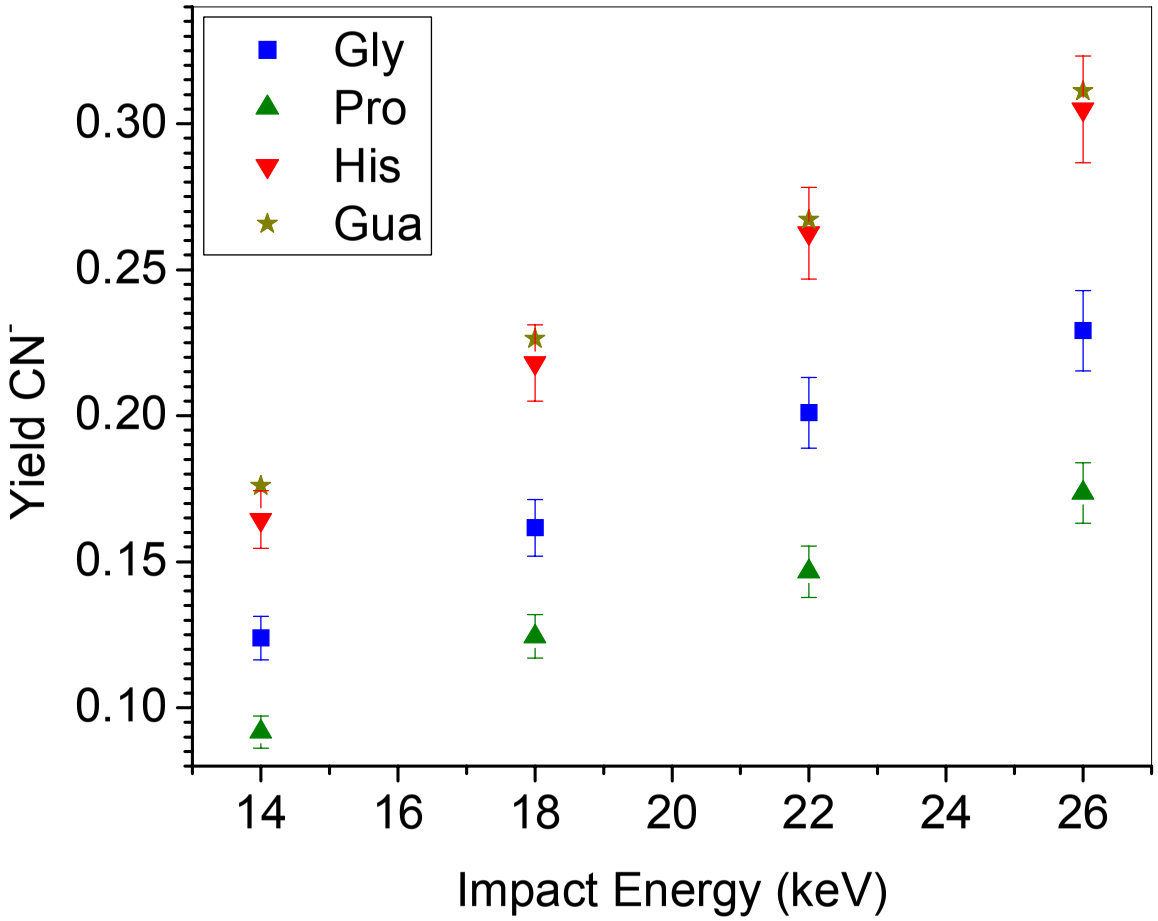

Figure 6-5: The yield of CN^- as a function of the C_{60}^+ impact energy. Error bars are 6% relative error. The error bars for Gua have been removed for aesthetic purposes.

examined with yields ranging from ~ 9 - 32 percent. The order of the CN^- yield is different than the order observed from the orders of the $[M-H]^-$ or $[M_2-H]^-$ yields (Figs. 6-3 and 6-4). The difference observed in the order of the CN^- yield can be attributed to the availability of nitrogen and carbon in the emission volume to produce CN^-. The number of nitrogen atoms available for CN^- production from Gly, Pro, His, and Gua molecules is 1, 1, 3, and 5 respectively. Table 6-2 approximates the number of nitrogen available in desorption volume based the following criteria: the desorption volume is a half-sphere 10 nm in diameter; the density of the samples is 1.45 g/cm^3, which is based on the known densities of other amino acids, which range from 1.3 - 1.6 g/cm^3 [116]; and the number of nitrogen atoms contain within the chemical structure of each sample. Table 6-3 shows the ratios of the estimated CN^- based on nitrogen availability and the ratios of the experimental yields of CN^-. If the ratios of the estimated and experimental CN^- yields are similar and/or some similar trend is observed within the ratios (e.g., the percent difference between the Gua/Pro ratio and the His/Pro ratio being similar for the estimated and experimental CN^- yields), then this would suggest that nitrogen availability is the only factor affecting CN^- emission. However, similar ratios and/or trends are not observed. Therefore, it is necessary to consider other factors that may affect CN^- emission such as molecular structure. The structural characteristics of the sample were examined for insight (Fig 6-2). The nitrogen atoms contained within the molecules are a mixture of primary, secondary, and tertiary amines. One can ask if CN^- emission is dependent on the type of amine the nitrogen atoms originate from. There is no apparent trend in the CN^- yield with the nature of the amine. The ratio of carbon

Table 6-2: The estimated number of molecules and available nitrogen atoms in a half-sphere desorption volume of 10 nm in diameter (numbers in parentheses represent 10% error). The experimental yields of CN^- produced by 26 keV C_{60}^+ impacts, normalized to the nitrogen available in the desorption volume. The ratio of carbon to nitrogen in the molecules.

Sample	Mass	~Molecules	~ Nitrogens	Norm. Yield CN-	Carbon / Nitrogen Ratio
Gly	75.07	3400 (340)	3400 (340)	0.1209	2
Pro	115.13	2000 (200)	2000 (200)	0.1541	5
His	155.15	1450 (145)	4350 (435)	0.1252	2
Gua	151.13	1500 (150)	7500 (750)	0.0743	1

Table 6-3: The ratio of estimated number of nitrogen atoms in a half-sphere desorption volume of 10 nm in diameter. The ratio of experimental yields of CN^- produced by 26 keV C_{60}^+ impacts.

Sample	Ratio of Est. Nitrogen	Ratio Yields of CN-
Pro/Pro	1.0	1.00
Gly/Pro	1.7	1.33
His /Pro	2.2	1.77
Gua/Pro	3.8	1.81

atoms to nitrogen atoms in the molecules can also be examined as a possible parameter affecting CN^- emission. In this regard, it must first be noted that nitrogen availability does affect CN^- emission and therefore must be accounted for to establish any trend associated with carbon. With this in mind, the experimental CN^- yield was normalized to the nitrogen availability in the desorption volume. The normalized CN^- yield as a function of the carbon/nitrogen ratio of several samples produced by 23 keV C_{60}^+ is shown in Figure 6-6. The overlap of the Gly and His points as well as the proline and gramicidin S points, given the respective size and structural differences of the samples, supports the notion that the carbon content influences CN^- emission. All the samples except Arg-Phe fall along the trend line. The exception may be the result of the unique structure of the arginine side group, which has a single carbon bound to three nitrogen atoms.

The emission of CN^- was examined to determine the type of emission (direct and/or rearrangement/recombination) produced by massive carbon-based projectiles. Previous studies have reported rearrangement/recombination in SIMS experiments. The bombardment of $NaBF_4$ produced the rearrangement/recombination ion series: $Na(NaF)_n^+$ in the positive mode [117] and $(NaF)_nF^-$ in the negative mode [66]. Guillermier, et al. examined rearrangement/recombination of CN^- from isotopically labeled glycine using Au_n^m (n = 1-400, m = 1-4). The study found a maximum of 45% of CN^- produced was the result of the recombination of carbon and nitrogen from different molecules [118].

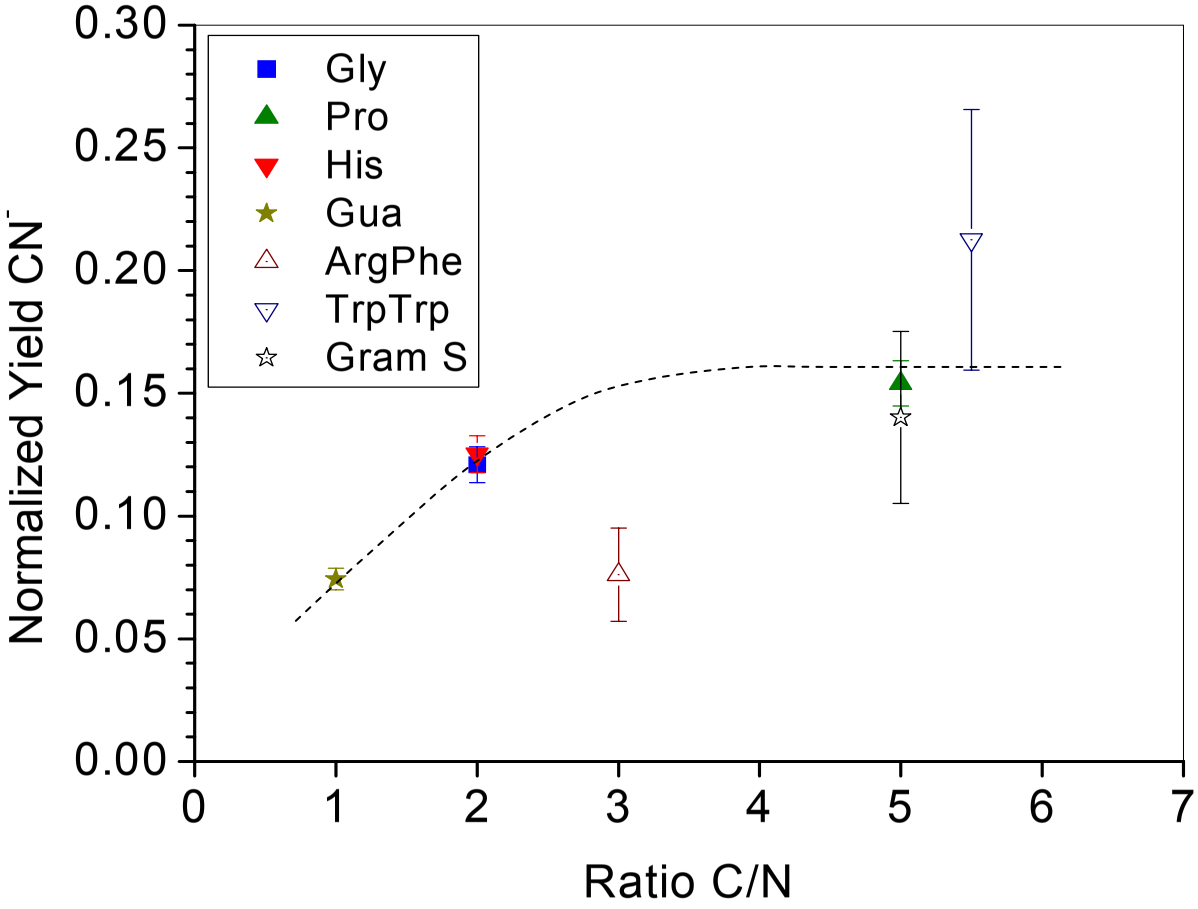

Figure 6-6: The yield of CN^- normalized to the nitrogen available in the desorption volume as a function of the ratio of carbon atoms to nitrogen atoms in the molecule. Solid symbols represent samples that are vapor deposited (error bars are 6% relative error). The hollow symbols represent samples that are solution deposited (error bars are 25 % relative error).

A similar isotopic study was performed using carbon-based projectiles. Vapor deposited samples of Gly-^{15}N, Gly-^{13}C, and a 50/50 mixture of Gly-^{15}N/Gly-^{13}C were bombarded with carbon-based projectiles to determine the percentage of CN^- that results from recombination. This percentage is termed the recombination rate.

If rearrangement/recombination does occur under keV bombardment of a 50/50 mixture of Gly-^{15}N/Gly-^{13}C, the expected products would include CN^- in the forms: $^{12}C^{14}N^-$, $^{13}C^{14}N^-$, $^{12}C^{15}N^-$, and $^{13}C^{15}N^-$. Recombination does occur as is evidenced by the appearance of m/z 28 in Figure 6-7 C. These isotopic forms of CN^- should produce a binomial distribution centered at m/z 27. In the absence of recombination, the yields of m/z 26, m/z 27, and m/z 28 from a 50/50 mixture of Gly-^{15}N/Gly-^{13}C should be an average of the yields from pure samples of Gly-^{15}N and Gly-^{13}C, which show no indication of recombination (i.e., a composite of both species). Therefore, the recombination rate can be found from the differences in yields of m/z 26, m/z 27, and m/z 28 from the composite and an actual 50/50 mixture of Gly-^{15}N/Gly-^{13}C.

The ratio of Gly-^{15}N to Gly-^{13}C in the mixture is assessed by comparing the peak areas of the respective [M-H] ions to produce accurate composite yields. For these experiments, the Gly-^{15}N/Gly-^{13}C mixture was a 50/50 mix within accuracy of the measurements. One concern with a mixture of this type is homogeneity. Figure 6-8 shows the mass spectra of the glycine mixture. The inset shows the molecular dimer region. The binomial distribution of dimer indicates that the two labeled glycine species are homogeneously mixed.

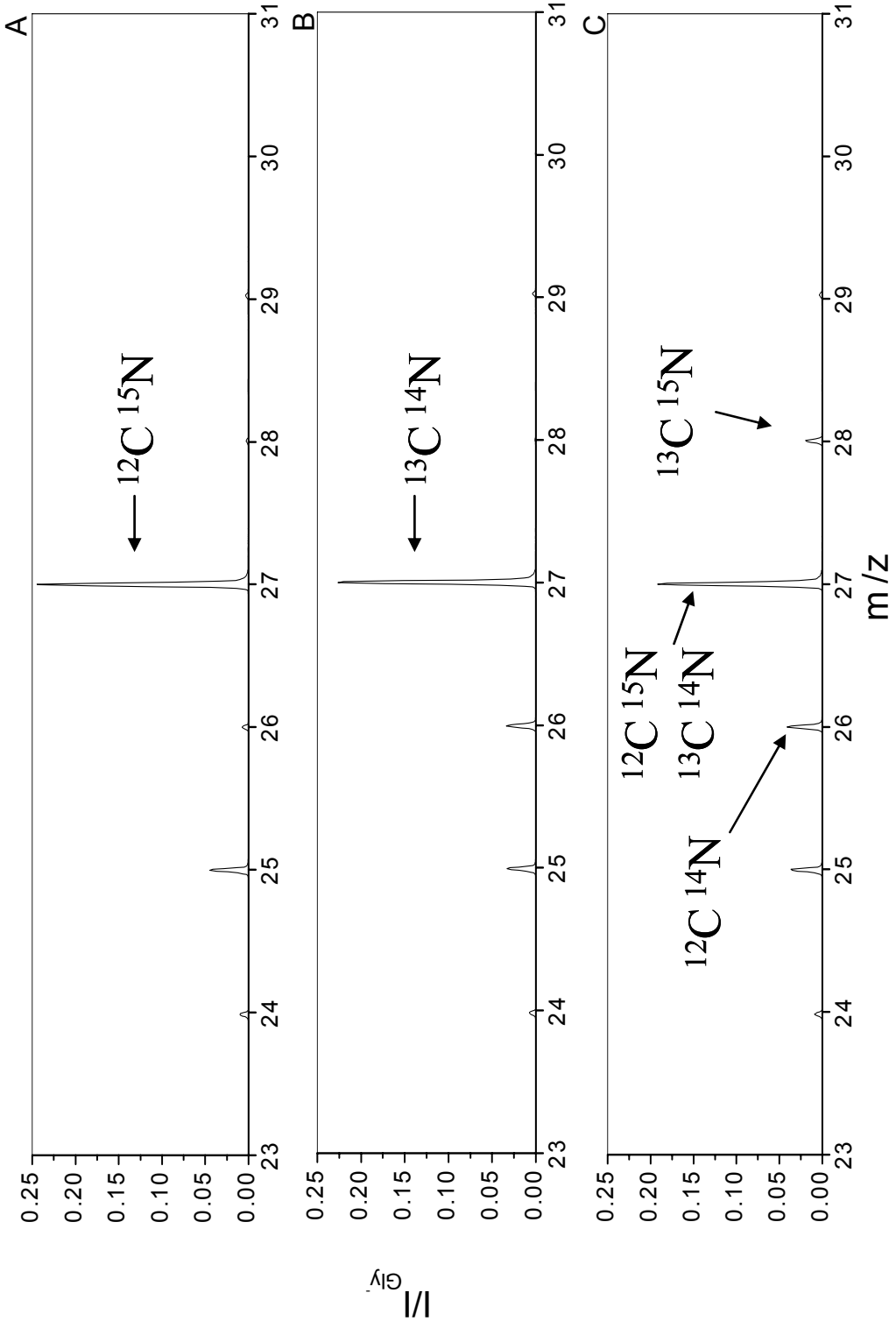

Figure 6-7: The CN^- region produced by 26 keV C_{60}^+ bombardment of a vapor deposited (A) Gly-^{15}N, (B) Gly-^{13}C, and (C) 50/50 Gly-^{15}N and Gly-^{13}C mixture.

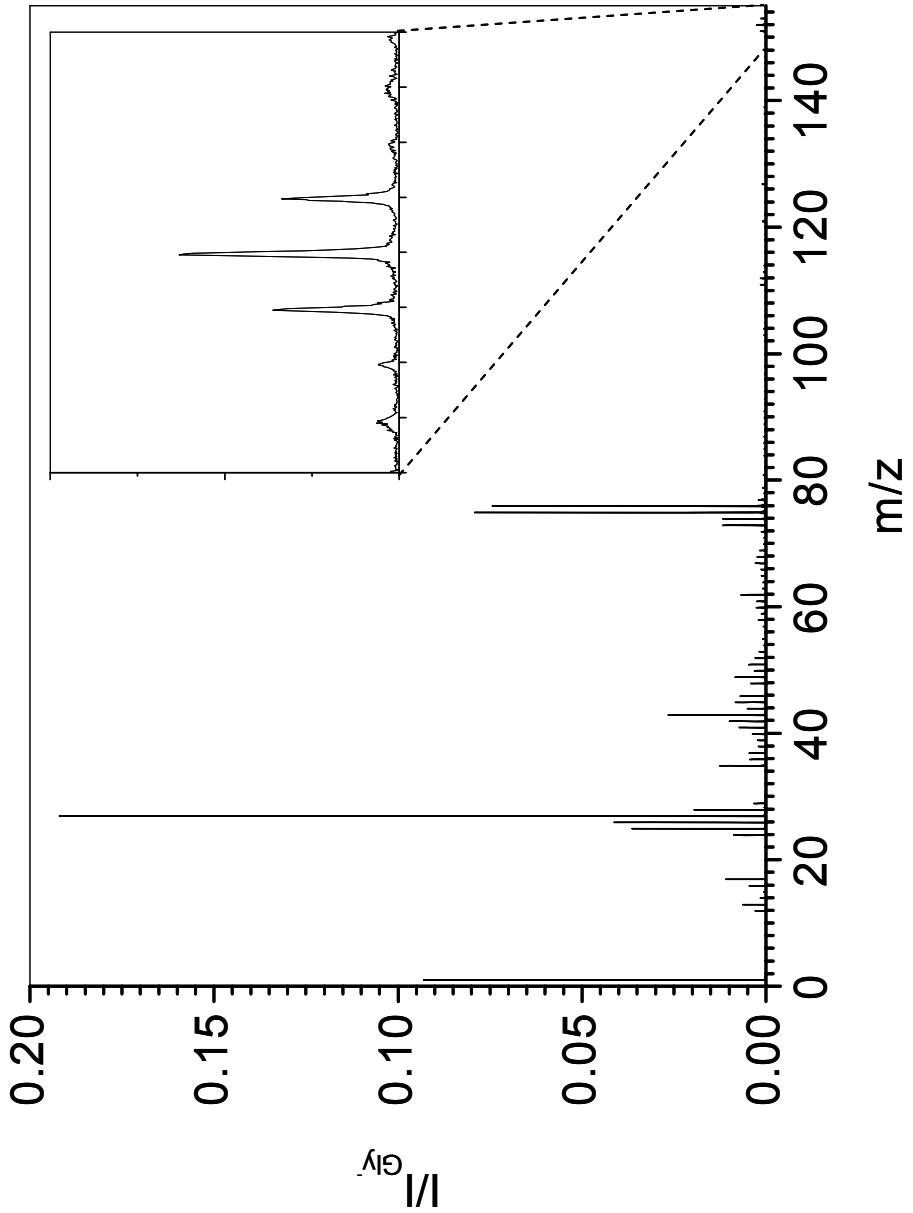

Figure 6-8: Negative secondary ion ToF spectrum produced by 26 keV C_{60}^{+} bombardment on a vapor deposited sample of 50/50 Gly-^{15}N and Gly-^{13}C. The inset shows the dimer region of the sample.

The recombination rate is calculated in a stepwise fashion. First, the difference in yields between the mixture and the composite for m/z 26, m/z 27, and m/z 28 is found by

$$\Delta Y_x = Y_{x,m} - \frac{(Y_{x,n} + Y_{x,c})}{2} \qquad \text{Eq. 6-1}$$

where ΔY_x is the difference in yield between the mixture and the composite for an ion of m/z x (x = 26, 27, or 28), $Y_{x,m}$ is the yield of m/z x from the mixture, $Y_{x,n}$ is the yield of m/z x from Gly-^{15}N, and $Y_{x,c}$ is the yield of m/z x from Gly-^{13}C. The recombination rate is found by

$$\text{recombination rate} = \frac{(\Delta Y_{26} - \Delta Y_{27} + \Delta Y_{28})}{(Y_{27,n} + Y_{27,c})/2} \qquad \text{Eq. 6-2}$$

where ΔY_{26}, ΔY_{27}, and ΔY_{28} are the differences in yield between the mixture and the composite for m/z 26, m/z 27, and m/z 28. $Y_{27,C}$ and $Y_{27,N}$ are the experimental yields of m/z 27 from Gly-^{13}C and Gly-^{15}N respectively. An example of the calculations is shown for 18 keV C_{60}^+ impacts (Table 6-4).

The recombination rate as a function of projectile impact velocity is shown in Figure 6-9. Generally, the recombination rate for all projectiles increases from 14-26 keV, though signs of a plateau region are observed. Given the error of the measurements, higher energy projectiles would be needed to verify that a plateau has in fact been reached. A plateau region is more evident in figure 6-10, which plots the recombination rate as a function of the projectile velocity. A plateau in the recombination rate is likely to occur under carbon cluster bombardment given that a similar phenomenon is observed using Au_n^m (n = 1-400, m = 1-4) projectiles [118]. If a

Table 6-4: Sample data for the calculation of the CN^- recombination rate.

18 keV C_{60}	Yield m/z 26	Yield m/z 27	Yield m/z 28
Gly 15N	0.00435	0.17469	0.00148
Gly 13C	0.02679	0.15897	0.00035
Gly mix	0.02860	0.14506	0.01222
	Difference m/z 26	Difference m/z 27	Difference m/z 28
	0.01303	-0.02177	0.01131
			Recombination Rate
			0.2763

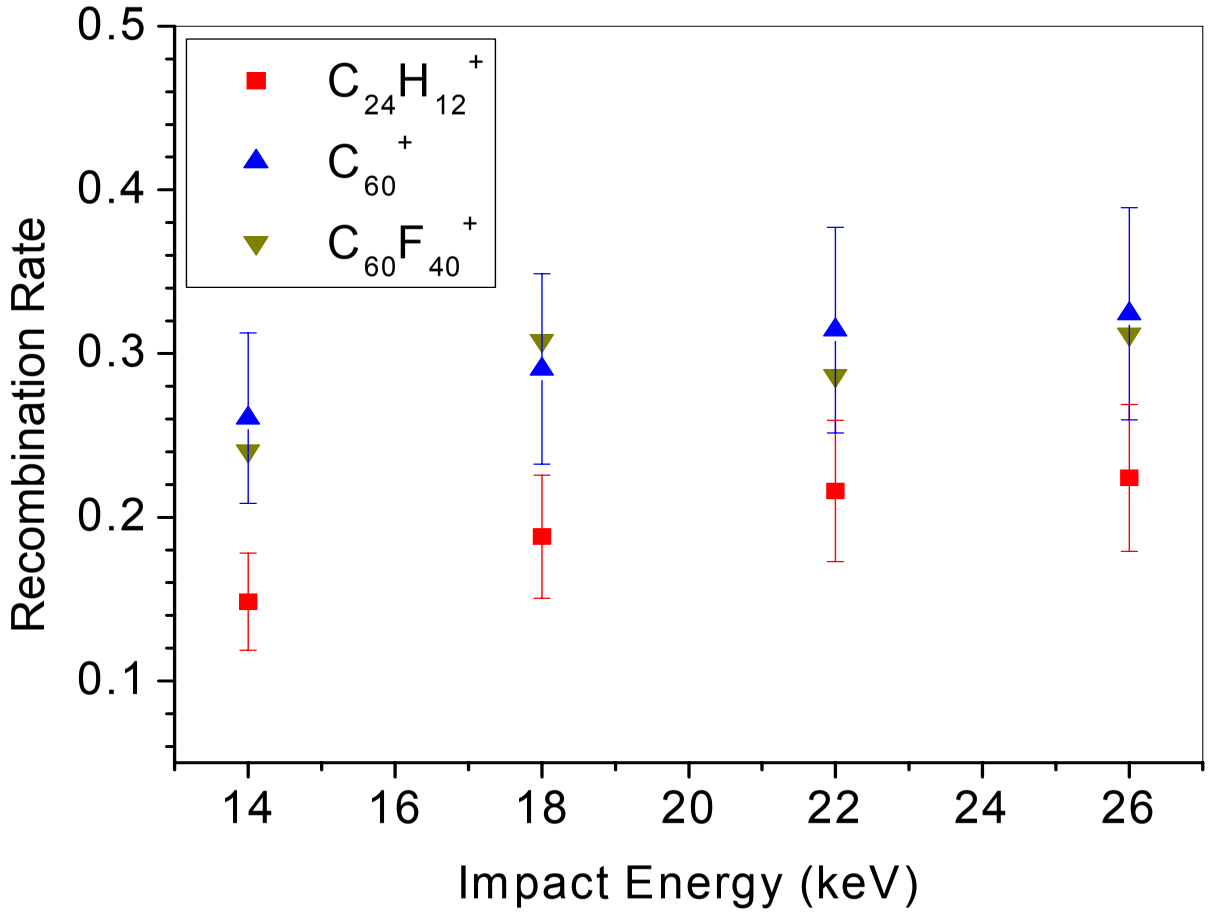

Figure 6-9: The recombination rate of CN^- as a function of projectile impact energy from glycine samples. The relative error is 20% (the error bars for $C_{60}F_{40}^+$ have been removed for aesthetic purposes).

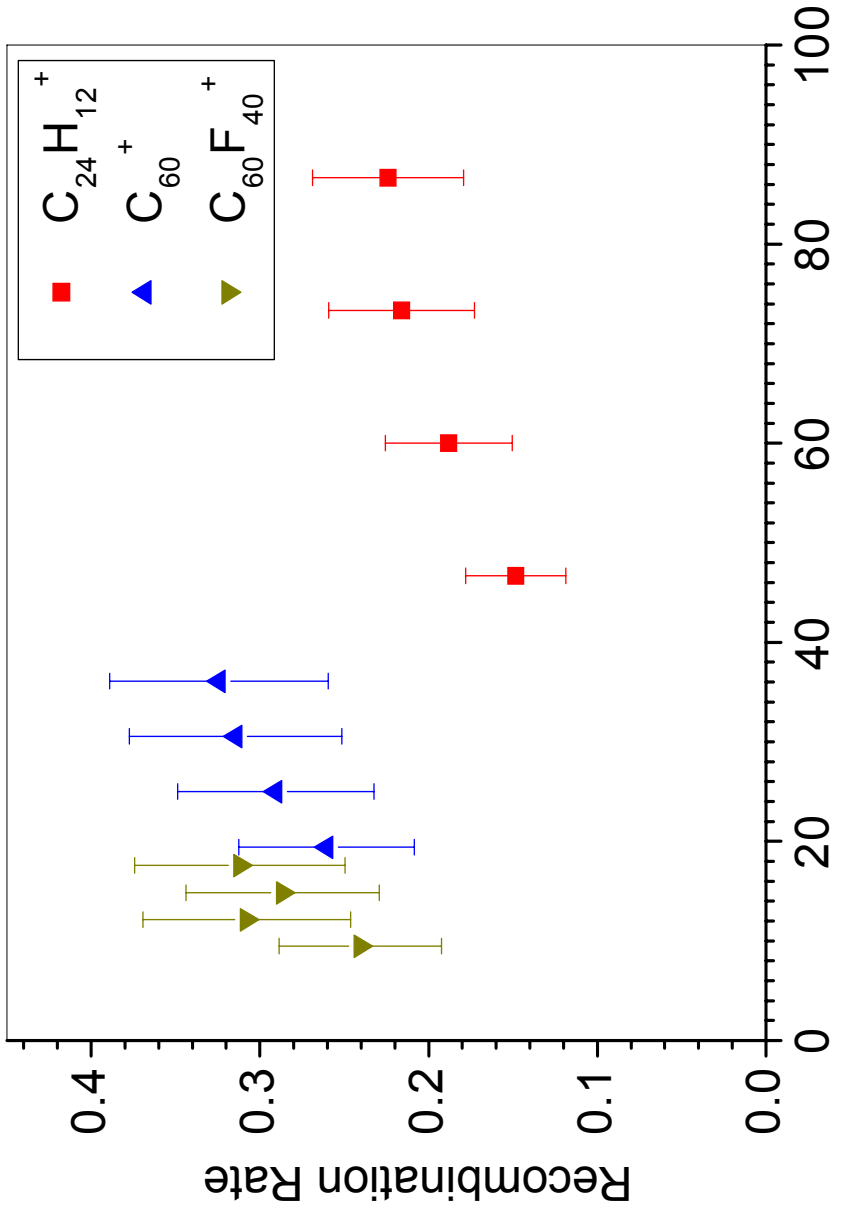

Figure 6-10: The recombination rate of CN^- as a function of the projectile velocity from glycine samples. The relative error is 20% (dashed lines are to guide the eyes).

plateau has been reached, this suggests that a carbon-based projectile of a given size is limited in the amount recombination it can produce. Therefore, the recombination rate is dependent primarily on the number of constituents in the projectile as $C_{24}H_{12}^{+}$ produces recombination rates that are ~50% lower than C_{60}^{+} at equal impact energies, while the recombination rates of C_{60}^{+} and $C_{60}F_{40}^{+}$ are similar at equal impact energies (Fig. 6-8). Additionally, the data suggest a saturation effect for the recombination rate using massive carbon-based projectiles. Once a projectile contains a certain number of constituents (i.e., ~60 constituents), the addition of more constituents does not increase the recombination rate. A similar trend has been observed previously [118].

The efficiency of a cluster projectile constituent to produce recombination is examined in Figure 6-11. The general trend for constituents of $C_{24}H_{12}^{+}$ and C_{60}^{+} is a linear increase with velocity. This suggests the effectiveness of a carbon in $C_{24}H_{12}^{+}$ and C_{60}^{+} is equivalent at equal velocities. The $C_{60}F_{40}^{+}$ series effectiveness is depressed compared to the $C_{24}H_{12}^{+}$ and C_{60}^{+} series. This may be chemical effects from the fluorine atoms of the projectile. The fluorine being highly electronegative may scavenge electrons reducing the number of electrons available for CN ionization, which reduce the production of CN^{-}. As stated earlier, the recombination rate reaches a maximum based on the projectile characteristics. However, the secondary ion yields for the recombination product, $^{13}C^{15}N^{-}$, increases linearly with impact energy (Fig. 6-12). This occurs because the higher energy projectiles perturb more of the surface material, which produces of more recombination products.

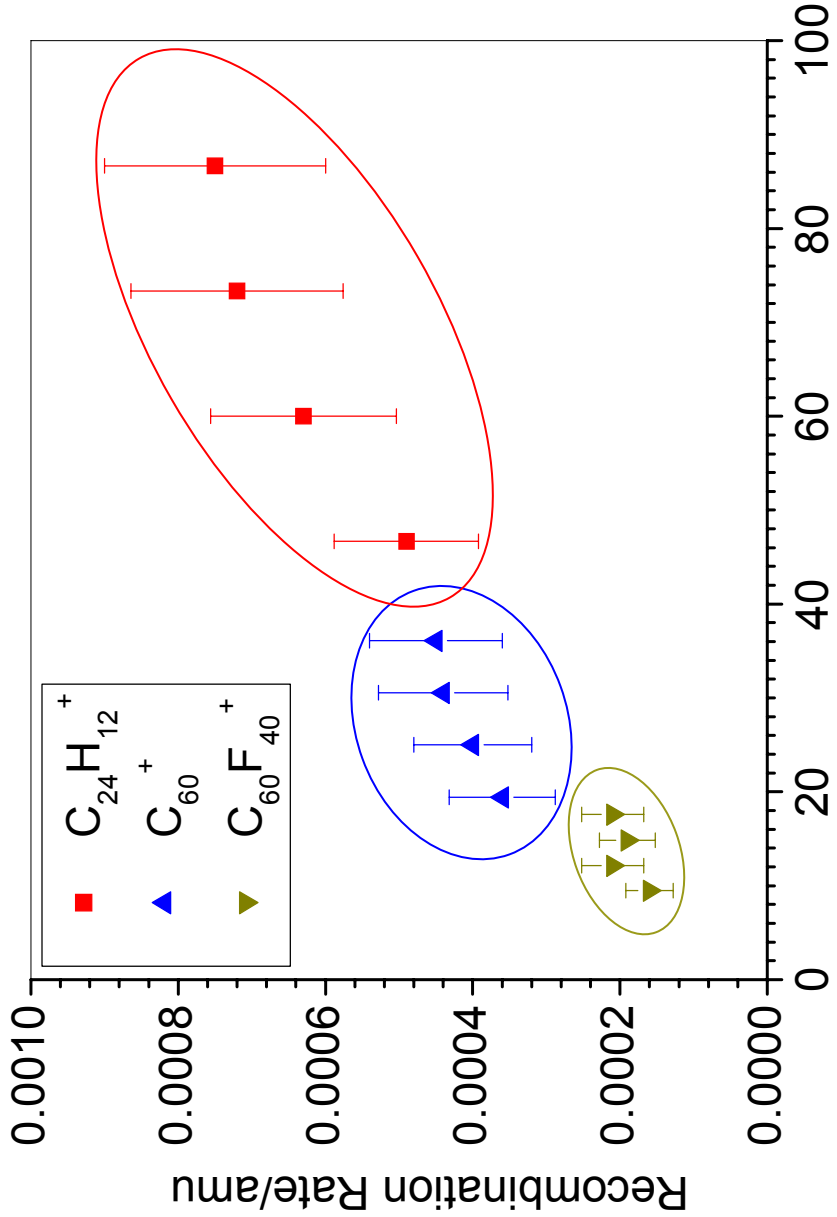

Figure 6-11: The recombination rate of CN^- per amu as a function of the projectile velocity from glycine samples. The relative error is 20%.

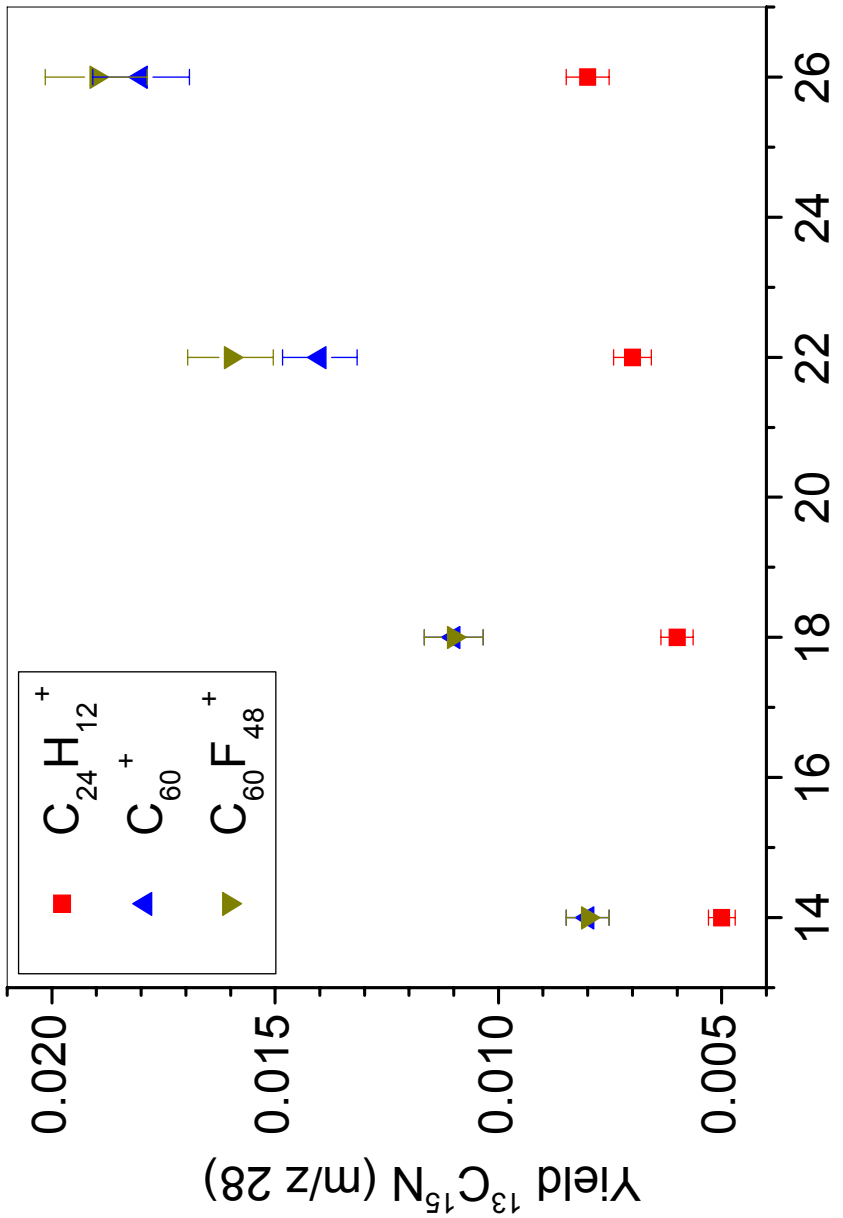

Figure 6-12: The yield of $^{13}C^{15}N^-$ (m/z 28) as a function of projectile impact energy from 50/50 Gly-^{13}C/ Gly-^{15}N sample.

The motivation for studying CN^- was that it could be used as a molecular identifier particularly in biological systems. Parameters affecting CN^- emission: carbon and nitrogen availability and recombination have been discussed. The samples used to illustrate the CN^- emission are idealized samples in comparison to typical biological samples. The question then arises as to how the information obtained on ideal compounds can be applied to more complex biological samples? In order to address this point, the preparation of the biological samples must be considered. In ion microscopy, freeze-drying is a standard practice used to prepare biological samples [4, 112-113, 119]. The removal of water from the cells concentrates the components of the cell leaving samples with similar compositions to those used in this study (i.e., compound primarily composed of C, N, and O atoms). Because of this, the recombination rate in the biological samples should be similar to those measured in our experiments. Therefore, with proper accounting of recombination, accurate detection of a labeled analyte is feasible via CN^- with enhanced sensitivity over what can be obtained with a molecular ion signal.

CHAPTER VII

MATRIX-ENHANCED CLUSTER-SIMS*

Sample preparation techniques are another method used to improve secondary ion yields. These techniques are referred to as matrix-enhanced or matrix-assisted SIMS. Matrix enhancement can be described as any substance added to a sample to improve the secondary ion yield. Over the years various methodologies have been used to produce a matrix enhancement effects. Cooks and co-workers used substrate and salt additives to enhance secondary ion yields by producing cationized species such as $[M+Ag]^+$ [33, 35]. Analyte molecules have been embedded in low molecular weight compounds such as an inorganic salts or organic acid with matrix-to-analyte ratios ranging from 20:1 to 10000:1 [33, 35-44]. Liquid matrices such as glycerol and sulfuric acid have been used in fast atom bombardment/liquid SIMS to improve secondary ion yields [120]. Metallization is a matrix enhancement method that involves the deposition of thin metal films (<5nm thick) on top of samples to increase secondary ion yields [34, 44]. We have examined sample preparation techniques in conjunction with polyatomic ion bombardment as a method to enhance secondary ion yields. Specifically, we have investigated the emission of the gramicidin S $[M-H]^-$ ion embedded in a matrix of sinapic acid.

---

*Reprinted excerpts and figures from Applied Surface Science, J. E. Locklear, C. Guillermier, S. V. Verkhoturov, and E. A. Schweikert, Matrix Enhanced Cluster-SIMS, in press May 2006, Copyright 2006 with permission from Elsevier.

The matrix/analyte ratio was varied to optimize the emission of the gramicidin S [M-H]- from the samples. Figures 7-1 A and 7-1 B are the mass spectra of neat gramicidin S and a 10:1 sinapic acid:gramicidin S mixture, respectively, under 23 keV C_{60}^{+} bombardment. The gramicidin S $[M-H]^-$ is clearly enhanced at the 10:1 matrix/analyte ratio.

The secondary ion yield is, again, described by the following equation

$$Y_{\text{exp}} = (I_{SI} / N_{PI}) \qquad \text{Eq. 7-1}$$

where I_{SI} is the experimental ion yield minus background, and N_{PI} is the number of primary ion impacts. The corrected secondary ion yield ($Y_{\text{cor exp}}$) is expressed as follows:

$$Y_{\text{cor exp}} = [I_{SI})/N_{PI}]/F_M \qquad \text{Eq. 7-2}$$

where F_M is the mole fraction of the surface film with respect to the ion of interest (i.e., at 10:1 sinapic acid:gramicidin S ratio, the F_M for CN would be 0.09). The percent relative error, E_r, is described as follows:

$$E_{\text{r}} = (\left|Y_{\text{exp}} - Y_{avg}\right| / Y_{avg}) * 100 \qquad \text{Eq. 7-3}$$

where Y_{exp} is the experimental yield of a given ion, and Y_{avg} is the average yield of a given ion.

The dependence of the gramicidin S $[M-H]^-$ yield as a function of the matrix/analyte ratio (neat gramicidin S (i.e., 0) to 100:1 matrix/analyte) is shown in Figure 7-2. There is a sharp rise in the gramicidin S $[M-H]^-$ with the maximum

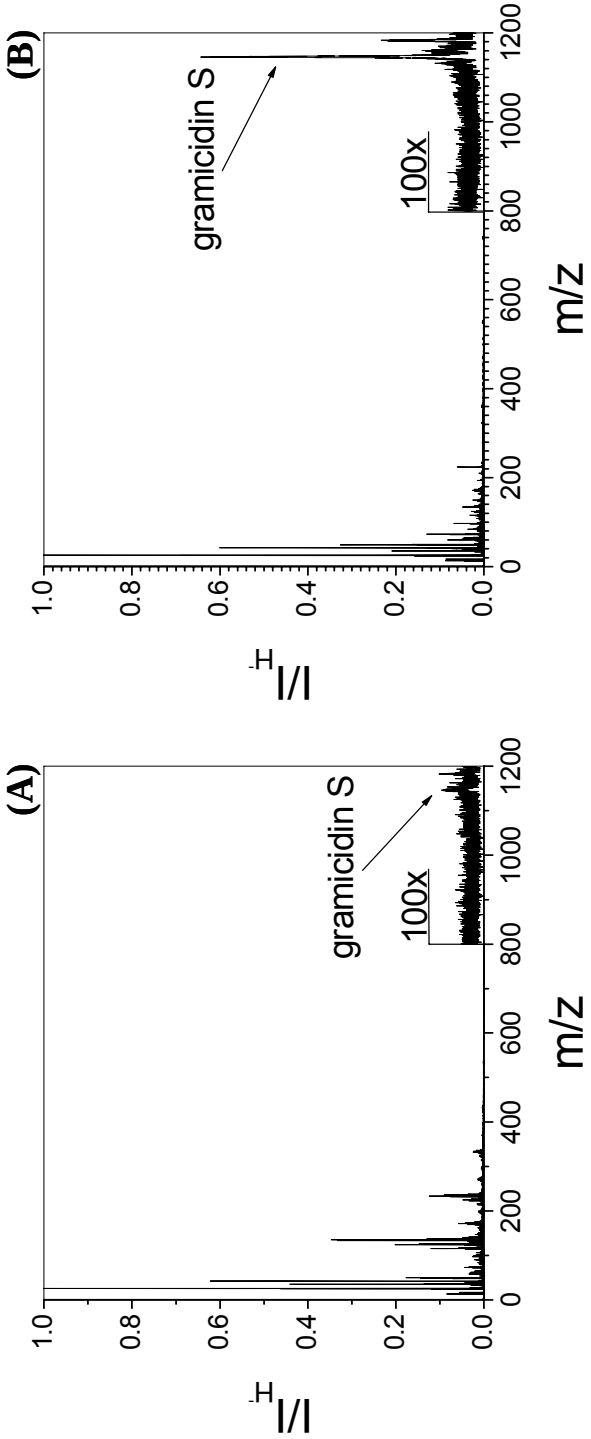

Figure 7-1: Negative secondary ion ToF spectra produced by 23 keV C_{60}^+ bombardment on (A) neat gramicidin S, (B) 10:1 sinapic acid:gramicidin S mixture. The region from 800 to 1200 m/z has been multiplied by a factor of 50 so that the gramicidin S peak may be seen.

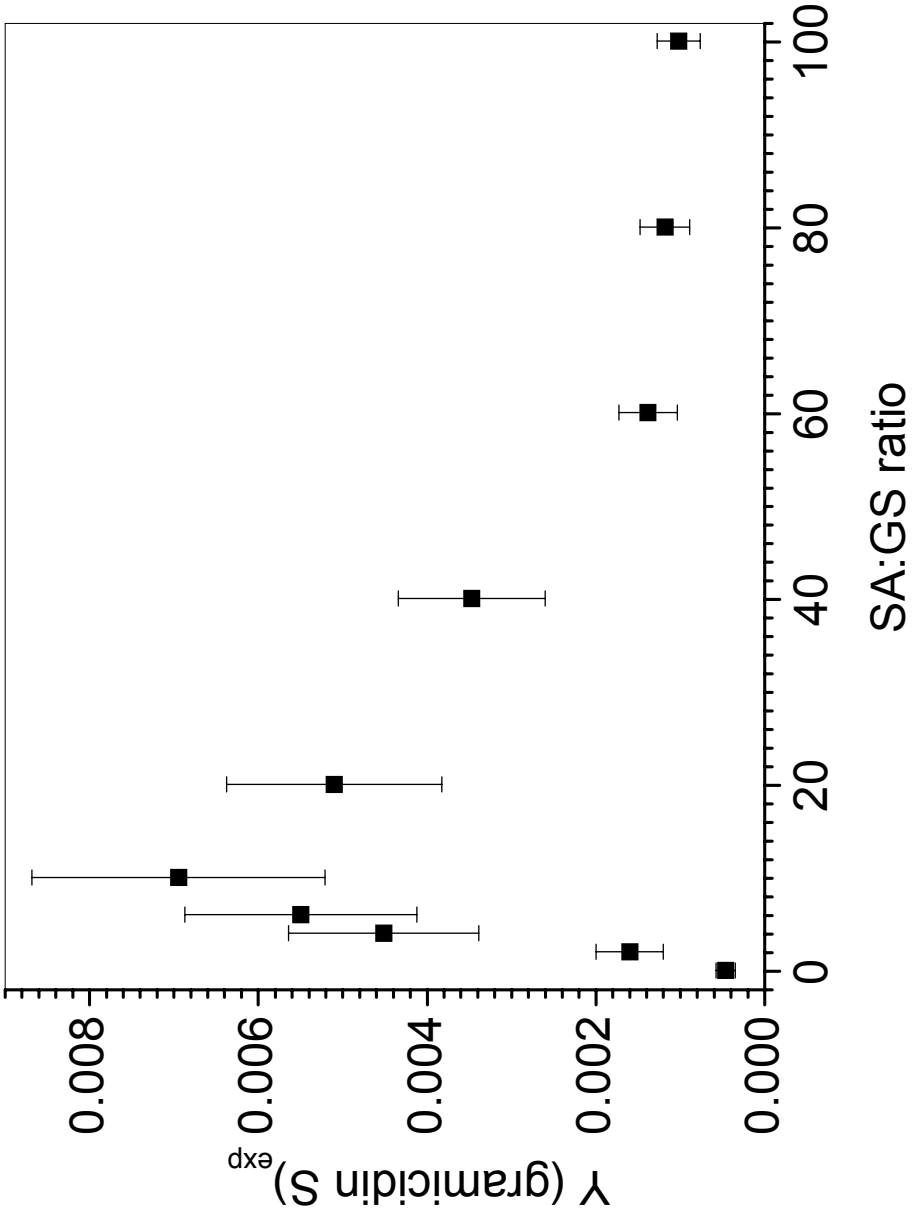

Figure 7-2: The yield of gramicidin S as a function of the matrix/analyte ratio produced by 23 keV C_{60}^{+} impacts. The error bars represent 25% relative error (the dashed line is meant to guide the eye).

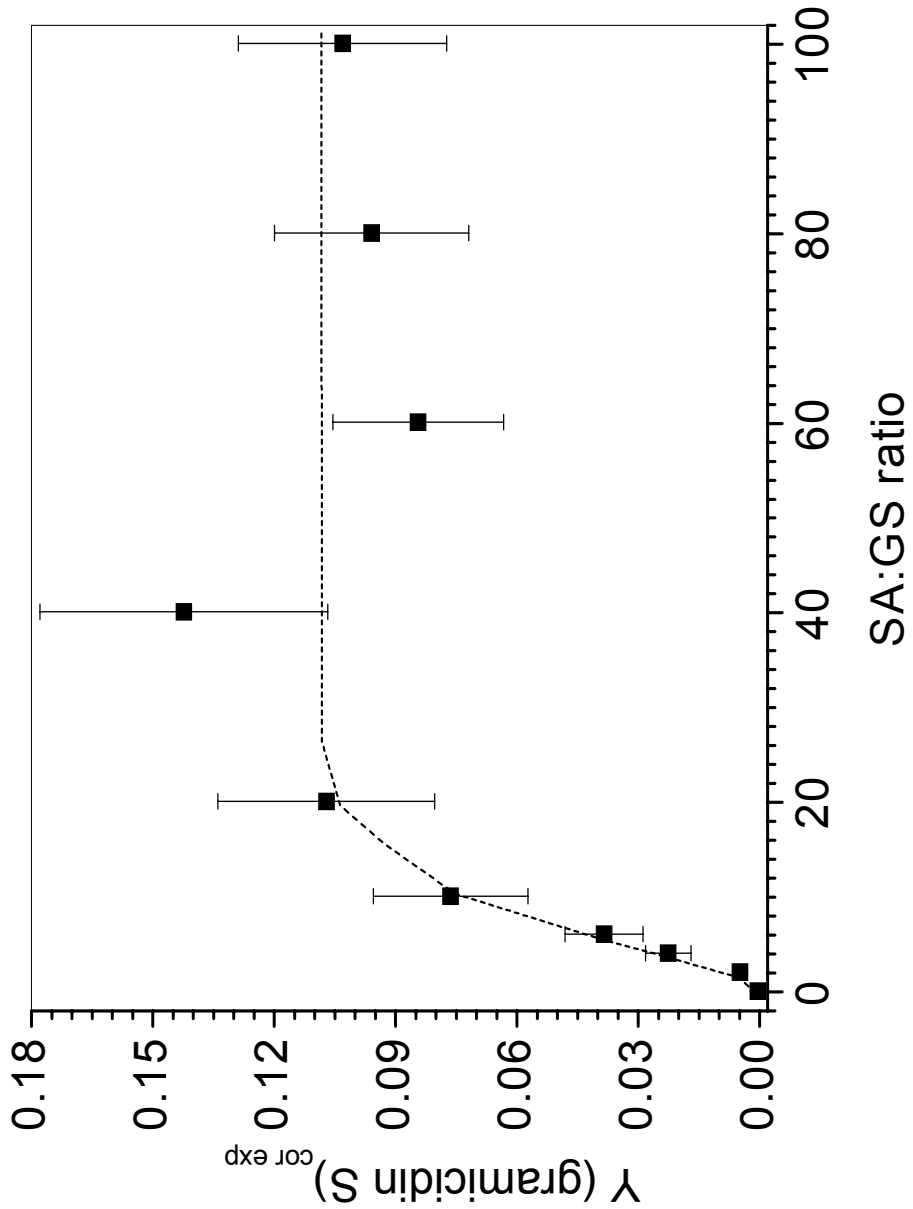

Figure 7-3: The corrected yield of gramicidin S as a function of the matrix/analyte ratio produced by 23 keV C_{60}^{+} impacts. The error bars represent 25% relative error (the dashed line is meant to guide the eye).

occurring at 10:1 matrix/analyte ratio followed by a slow decrease. The gramicidin S $[M-H]^-$ yield at the maximum is approximately 15 times higher for the 10:1 mixture than the neat gramicidin S. The shape of this curve can be explained by the isolation and encapsulation of gramicidin S molecules by matrix molecules. It is not experimentally possible to directly observe if the 10:1 ratio is the most effective ratio for gramicidin S $[M-H]^-$ emission independent of dilution effects. However, using the mole fractions of the analyte and matrix in the film (i.e., the number of molecules available for ionization in the desorption volume), corrections can be made to account for dilution effects.

The results of this correction are shown in Figure 7-3. The trend observed suggests that the matrix continues to increase its efficiency to produce gramicidin S $[M-H]^-$ beyond the 10:1 ratio observed in Figure 7-2, and that the maximum observed in Figure 7-2 is primarily the result of analyte dilution. The plateau occurring after the 20:1 maximum in Figure 7-3 indicates that the addition of more matrix beyond this point does not increase its effectiveness.

Further investigation into a possible mechanism was examined by observing the trends of co-emitted ions from single ion impacts. The relative yield of co-emission is described by

$$\text{Relative Yield of Co-Emission} = \frac{Y(A^-, B^-)}{Y(A^-) * Y(B^-)} \qquad \text{Eq. 7-4}$$

where $Y(A^-,B^-)$ is the yield of A^- co-emitted with B^-, $Y(A^-)$ is the yield of A^-, and $Y(B^-)$ is the yield of B^-.

The impact region can be described as two overlapping regions (fragmentation region and molecular emission region) in a decaying energy gradient originating at the exact impact point of the projectile on the surface. The effective size of the fragmentation region can be controlled by the addition of matrix to an analyte. This can occur in an encapsulation model, in which the matrix increasingly surrounds the analyte as the matrix/analyte ratio increases. In this model, the matrix increases the analyte $[M-H]^-$ production by cooling analyte $[M-H]^-$ in the gas phase via evaporation of attached matrix molecules [33, 35].

The relative yield of CN^- co-emitted with the sinapic acid has a variable trend (Fig. 7-4 A). Initially, a declining trend is observed because gramicidin S is surviving more due to matrix cooling and is becoming more dilute. (i.e., a large effective fragmentation volume). The inflection at 20:1 marks the point were matrix cooling is maximized (complete analyte encapsulation) and with a minimum amount of matrix available. Since gramicidin S emission is maximized, the fragment, CN, is seen minimally. After reaching a minimum at 20:1, an ascending trend is observed. This occurs even though the matrix cooling is maximized because the matrix is becoming more abundant. Therefore, any CN^- produced in fragmentation volume is more likely to be observed with a matrix ion (i.e., small effective fragmentation volume). The inflection point at 20:1 in Figures 7-4 A and B correspond to the inflection point observed in the corrected gramicidin S yield (Fig. 7-3) adding further evidence for an encapsulation model.

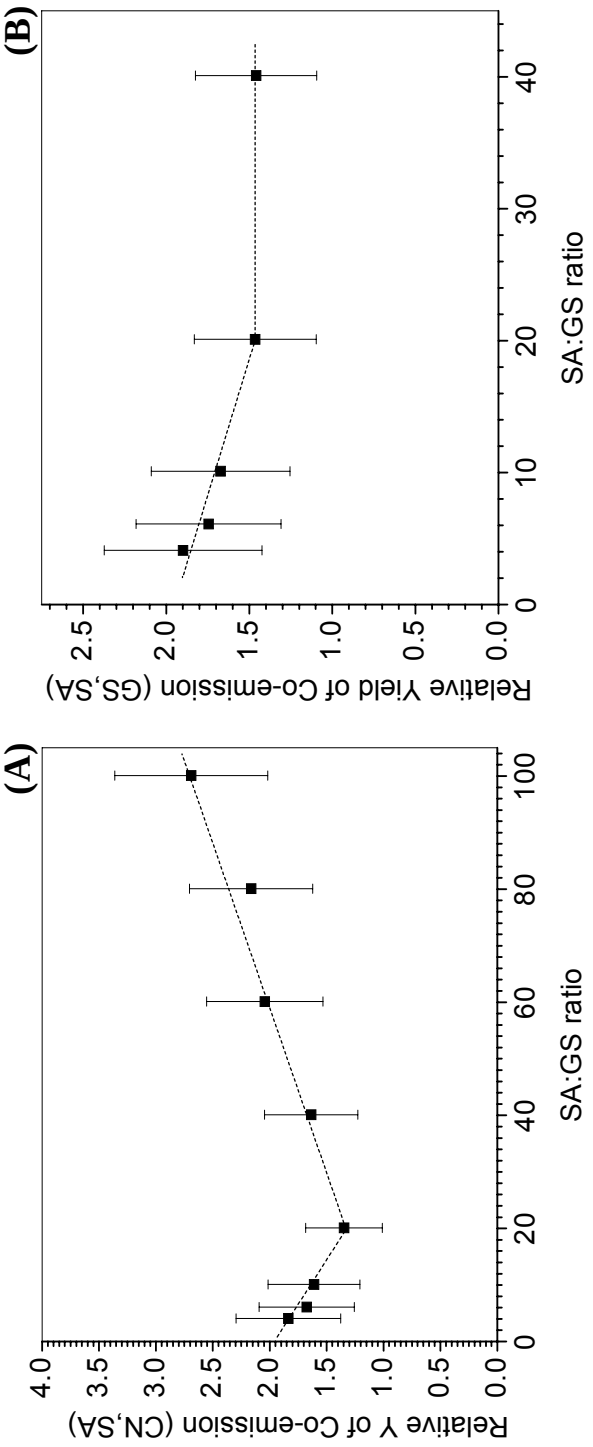

Figure 7-4: Relative yield of co-emission as a function of the matrix/analyte ratio produced by 23 keV C_{60}^+ bombardment (A) CN^- co-emitted with sinapic acid , (B) gramicidin S co-emitted with sinapic acid. The error bars represent 25% relative error (the dashed line is meant to guide the eye).

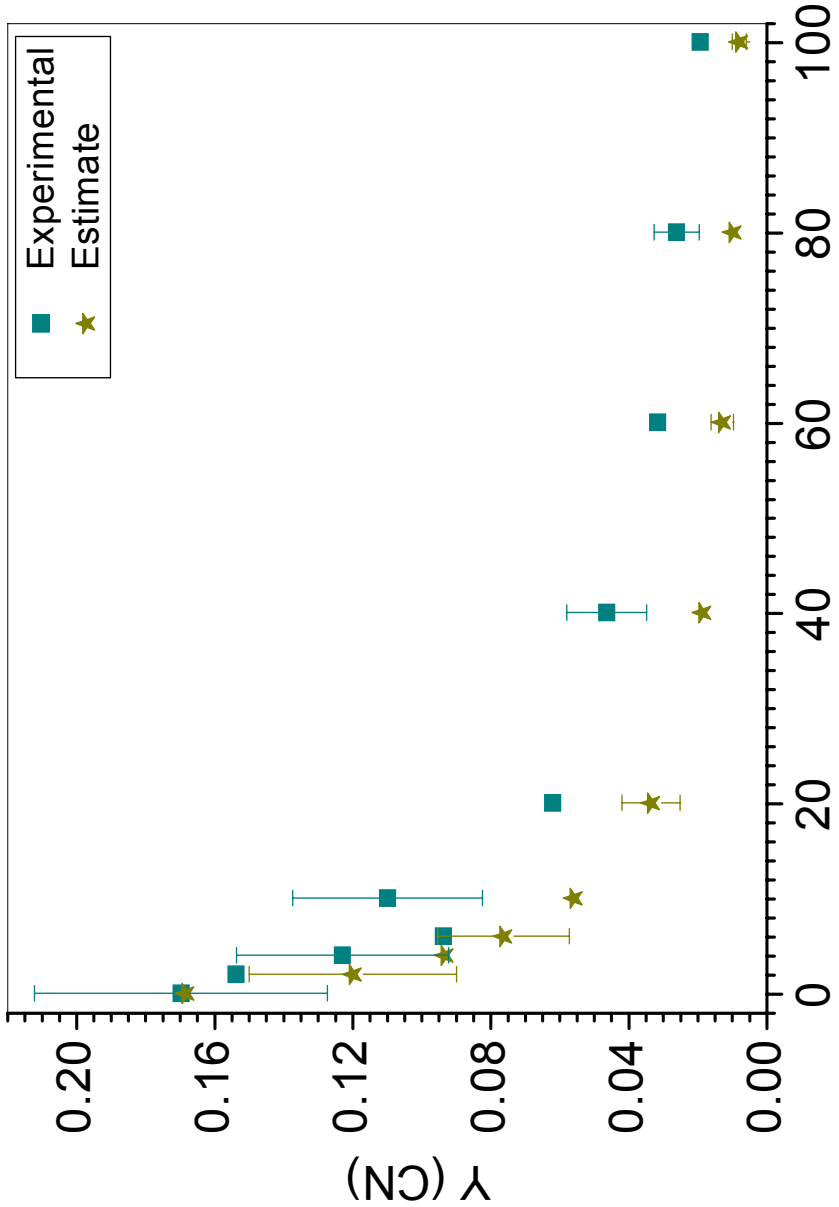

Figure 7-5: Experimental and estimated yields of CN^- as a function of the matrix/analyte ratio. The experimental yields were produced by 23 keV C_{60}^+ impacts. The error bars represent 25% relative error (note: alternating error bars in each series have been omitted for aesthetic purposes).

The yield of CN^- which originates from gramicidin S was also examined. CN^- originates in the fragmentation region, i.e., the impact region where atomization and fragmentation predominate. Given that a matrix effect is observed with gramicidin S, the question arises, if a similar phenomenon occurs for CN^-. In order to achieve a comparison, an estimate of the CN^- yields independent of matrix effects was preformed. The estimate is based on the following criteria: (a) ionization occurs in a half-sphere desorption volume that is ~10 nm in diameter and ~5 nm deep, (b) gramicidin S and sinapic acid have densities of approximately 1 g/cc, and (c) 0.01% of the desorbed CN are detected as ionized species. Using these criteria on a pure gramicidin S sample, a single C_{60} impact would interact with a volume containing ~140 gram S molecules, each containing 12 CN groups. This would produce ~0.16 CN^- per impact. The result of the estimated CN^- yields is shown in Figure 7-5. The experimental and estimated CN^- yields exhibit a similar trend as the matrix/analyte ratio increases suggesting that the matrix has minimal affect on the emission of CN^-.

In addition to monitoring the peaks associated with the analyte, the sinapic acid $[M-H]^-$ was also monitored as a function of the matrix/analyte ratio (Fig. 7-6). The sinapic acid $[M-H]^-$ also experiences an enhancement of approximately 2 times. This increase is observed at higher matrix/analyte ratios than with gramicidin S $[M-H]^-$ suggesting differences in the emission mechanism. The experimental yield and corrected yield of sinapic acid as a function of the matrix/analyte ratio are compared in Figure 7-7. There is no significant difference between the corrected and experimental yields of sinapic acid. The corrected and experimental yields rise to a maximum at a

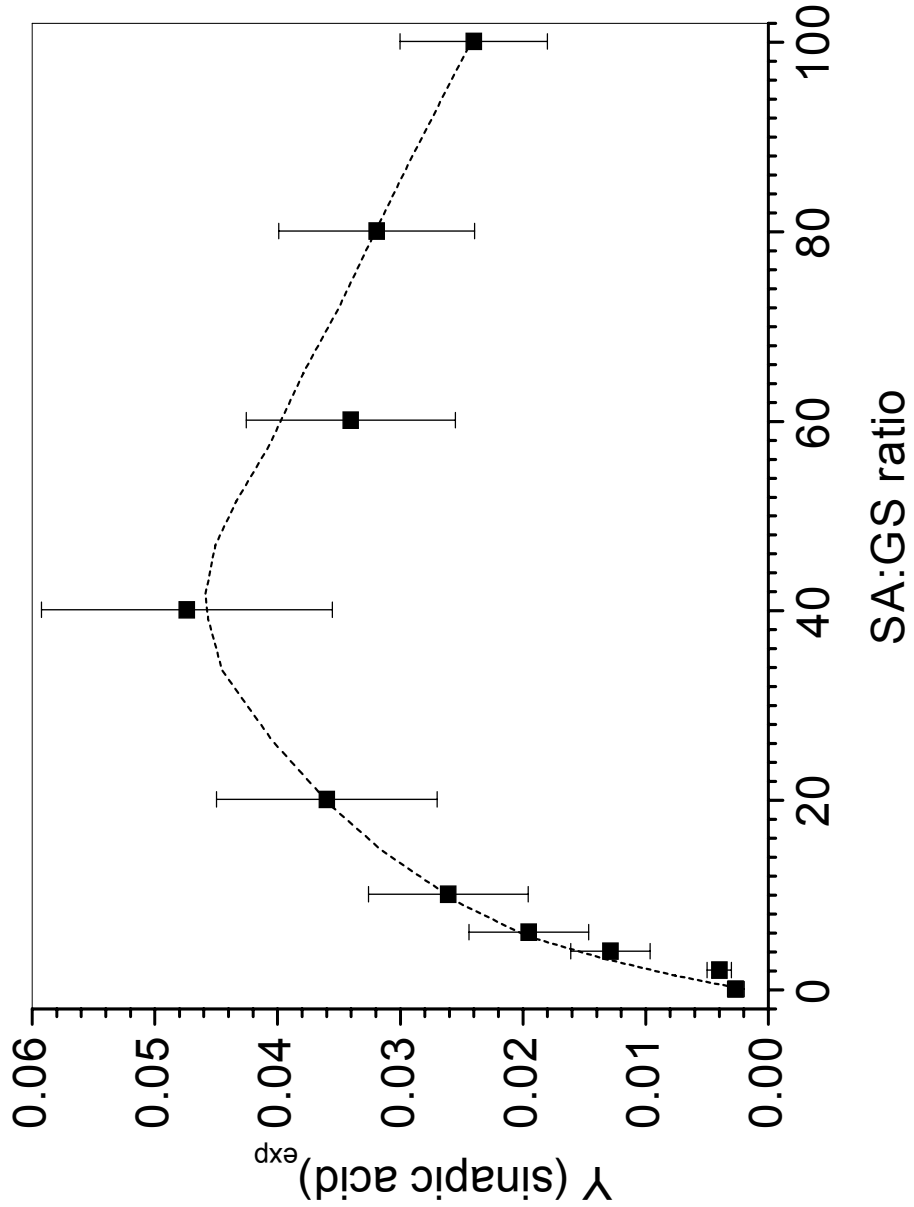

Figure 7-6: The yield of sinapic acid as a function of the matrix/analyte ratio produced by 23 keV C_{60}^{+} impacts. The error bars represent 25% relative error (the dashed line is meant to guide the eye).

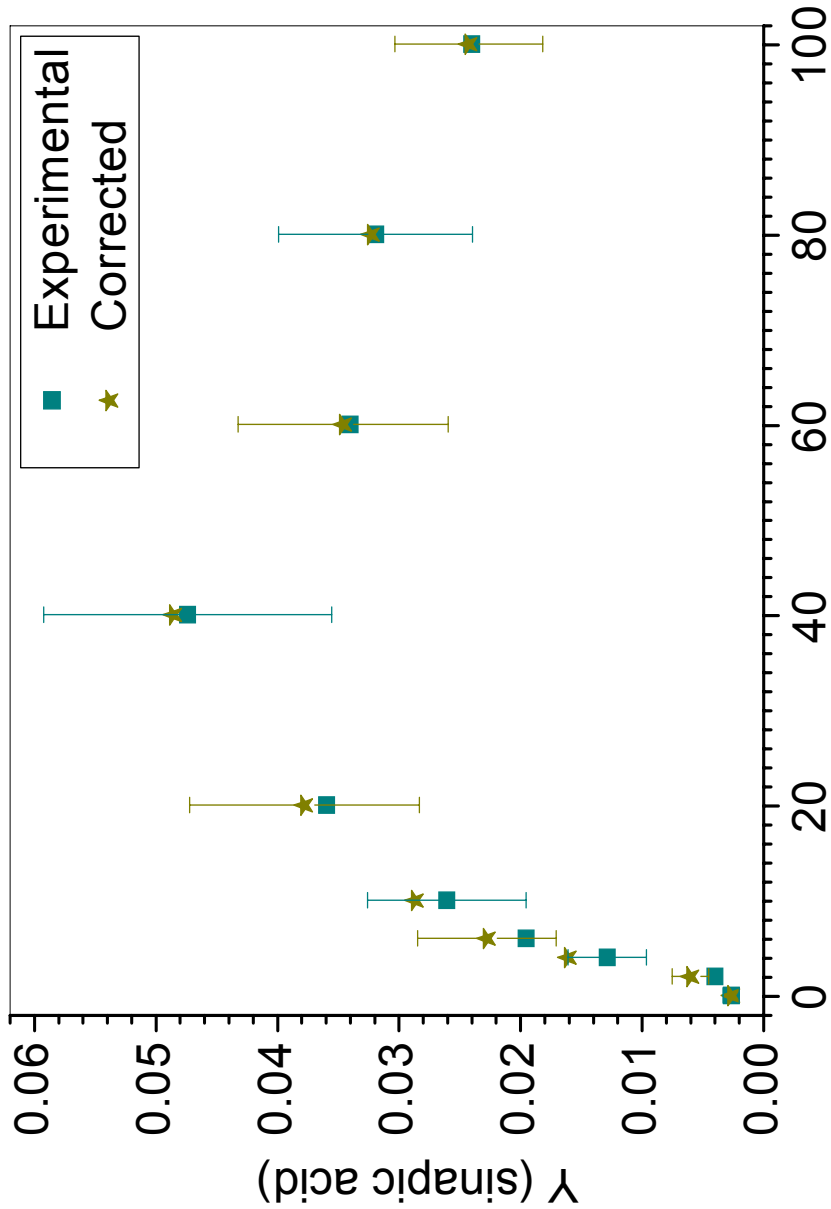

Figure 7-7: Experimental and corrected yields of sinapic acid as a function of the matrix/analyte ratio produced by 23 keV C_{60}^{+} impacts. The error bars represent 25% relative error (note: alternating error bars in each series have been omitted for aesthetic purposes).

matrix-to-analyte ratio of 40:1 followed by a decline to ~50% of the maximum with increasing matrix-to-analyte ratios. This contrasts to the corrected and experimental yields of gramicidin S (Figs. 7-2 and 7-3) in which the experimental yields of gramicidin S rise to a maximum at a matrix-to-analyte ratio of 10:1 followed by a decline to ~15% of the maximum at 100:1 matrix-to-analyte ratio, while the corrected yields of gramicidin S reach a plateau at a matrix-to-analyte ratio of 20:1 and remain constant at matrix-to-analyte ratios up to 100:1. This suggests that the enhancement observed with sinapic acid is produced by segregation and not a combination of segregation and ionization effects. Between 10:1 and 100:1 matrix/analyte ratio, the desorption volume contains ≥ 75% sinapic acid. Because of this high concentration, it is unlikely that the ionization probability of sinapic acid changes significantly in this range.

CHAPTER VIII

RE-EMITTED PROJECTILE IONS

An important question in cluster-solid interactions is the "fate" of the projectile atoms upon impact with a surface. There are theoretical and experimental reports describing emission of projectile constituents back into the vacuum [50, 51, 106, 121-122]. Our experimental method is uniquely suited for comparisons to molecular dynamics (MD) simulations because each uses a single projectile impact to investigate particle emission from surfaces. As stated earlier, MD simulations examine sputtered neutral particles, while event-by-event experiments examine secondary ions. It is assumed that for a given projectile-target combination, a reproducible fraction of the ejecta is ionized. Even with this distinction, similarities in trends are observed between event-by-event experiments and MD simulations.

Diehnelt, et al. conducted experiments using 12-28 keV $(NaF)_nNa^+$ (n = 1, 2, 4) and SF_5^- projectiles to bombard Au, SiO_2, and α-cyano-4-hydroxycinnamic acid surfaces [106]. The yield of recoiled F^- (i.e., F^- originating from the projectile) increased as the number of F atoms in the projectile increased but decreased with increasing impact energies. The yield of recoiled F^- also increased as the atomic weight of the target increased.

Brunelle, et al. carried out experiments examining "splashed" D^- from 2-30 keV projectiles of valine-D_8 and benzoperylene-D_{12} from targets of CsI and Au [50]. The

yield of D^- was found to increase linearly with the projectile impact velocity. D^- was also found to retain a portion of its initial kinetic energy.

A unique set of ions origination from the projectile has been found using 40 - 136 keV Au_n^m (n = 100-400, m = 4) projectiles [79-81, 118, 123]. In these experiments, two distinct series Au_n^- (n= 1-17) and Au_nX^- (n= 1-17, X = components of the target such as CN) were observed. The later series, Au_nX^-, has been termed an adduct series.

In each of the cases, the emission of projectile constituents was found to be a prompt emission, occurring simultaneously with the desorption/ionization process.

MD simulations with cluster projectiles have predicted the emission projectile components back into the vacuum [31, 121]. An inverse energy dependence similar to those found by Diehnelt, et al. have been simulated using $(NaF)_nNa$ (n = 1, 2, 4) projectiles on gold surfaces [121]. The inverse dependence was attributed to increased penetration of the projectile atoms with increasing energy [121]. The differing trends found by Diehnelt, et al. and Brunelle, et al. with F^- and D^-, respectively, were attributed to a variable ionization probability for deuterium with increased impact energy [121]. MD simulations have also predicted the retention of some initial kinetic energy by re-emitted constituents.

Experiments were conducted to identify re-emitted projectile constituents from carbon cluster projectiles. Identification of re-emitted carbon atoms from a C_{60} projectile is difficult since carbon and carbon fragments can originate from multiple sources including the projectile, surface contamination, and the target being examined.

Therefore, $C_{60}F_{40}^+$ was used as a projectile. This projectile provides an isotopically pure signal (F^-) to monitor with negligible interferences.

Targets of Gly, BN, Al_2O_3, NaCl, Cu, Ag, and Au were bombarded by 14-26 keV $C_{60}F_{40}^+$. In each case, a fraction of the projectile fluorine atoms were re-emitted in a prompt in-situ process occurring simultaneously with the desorption/ionization process of the surface upon projectile impact.

Two methods were employed to verify that the peak observed at m/z 19 in the mass spectrum were not the result of pre-implantation from previous $C_{60}F_{40}^+$ projectiles or surface contamination (e.g., Figure 8-1). The secondary ions from a small portion of the full data set can be examined since the experiments are run in event-by-event mode (e.g., secondary ions produced from the first 100 projectiles of a set of one million can be examined). F^- should be present in the mass spectrum immediately if m/z 19 is not the result of pre-implantation. Recall the likelihood of two projectiles impacting the same area of a sample is small under event-by-event conditions. Figure 8-2 B-D shows the evolution of the mass spectrum as a function of the number of incident $C_{60}F_{40}^+$. F^- is visible after ~2100 projectile impacts (Fig 8-2 B) and the yield of F^- is the same as the yield of F^- observed after ~20000 and ~2.1 million projectile impacts, respectively (Fig 8-2 C and D). This clearly indicates F^- is not the result of pre-implantation. Secondly, the mass spectra produced by 26 keV C_{60}^+ and 26 keV $C_{60}F_{40}^+$ were compared to insure m/z 19 is not fragment generally associated with massive carbon-based projectiles. Figure 8-2 A and D verify that m/z 19 is

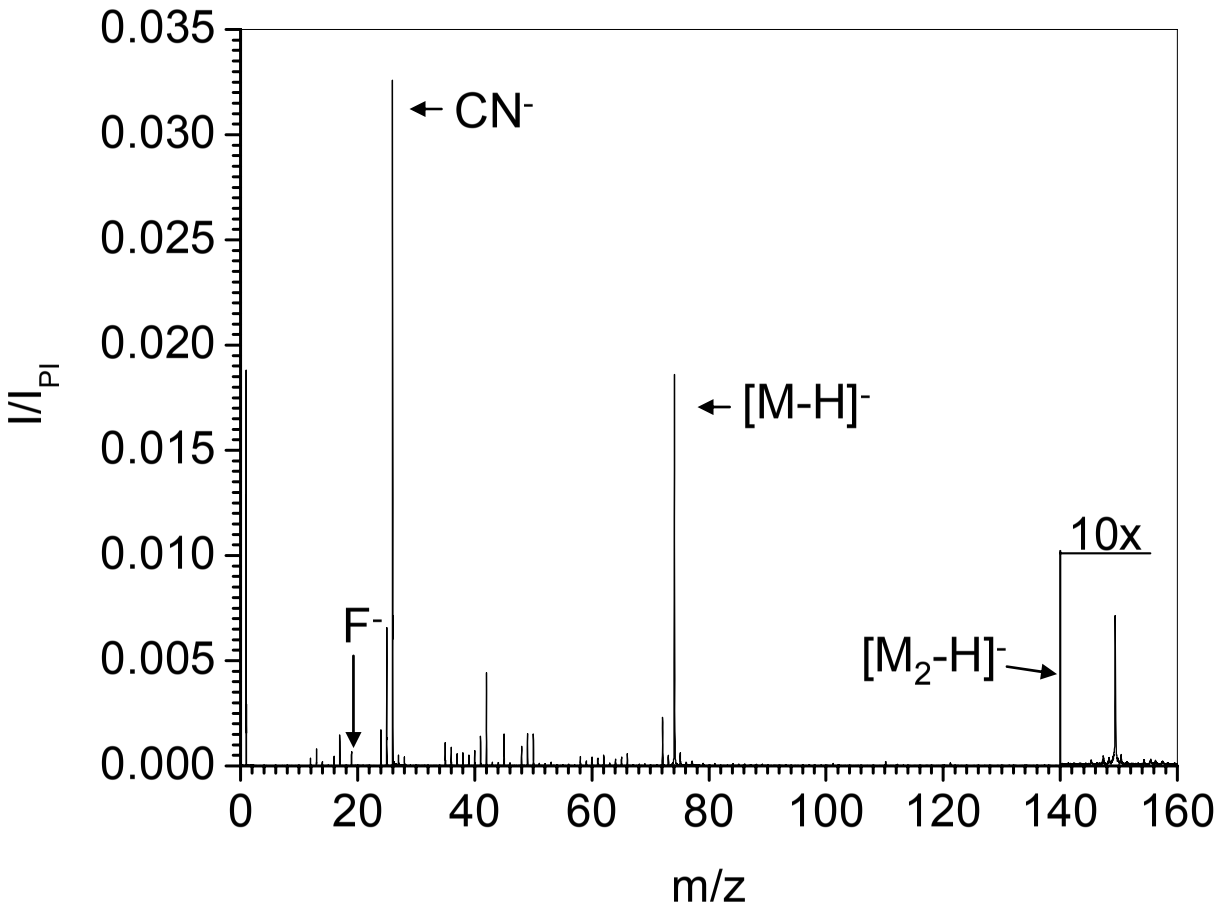

Figure 8-1: Negative secondary ion ToF spectrum produced by 26 keV $C_{60}F_{40}^{+}$ bombardment on a vapor deposited sample of glycine. The dimer region has been multiplied by a factor of 10 so that the dimer peak may be clearly observed.

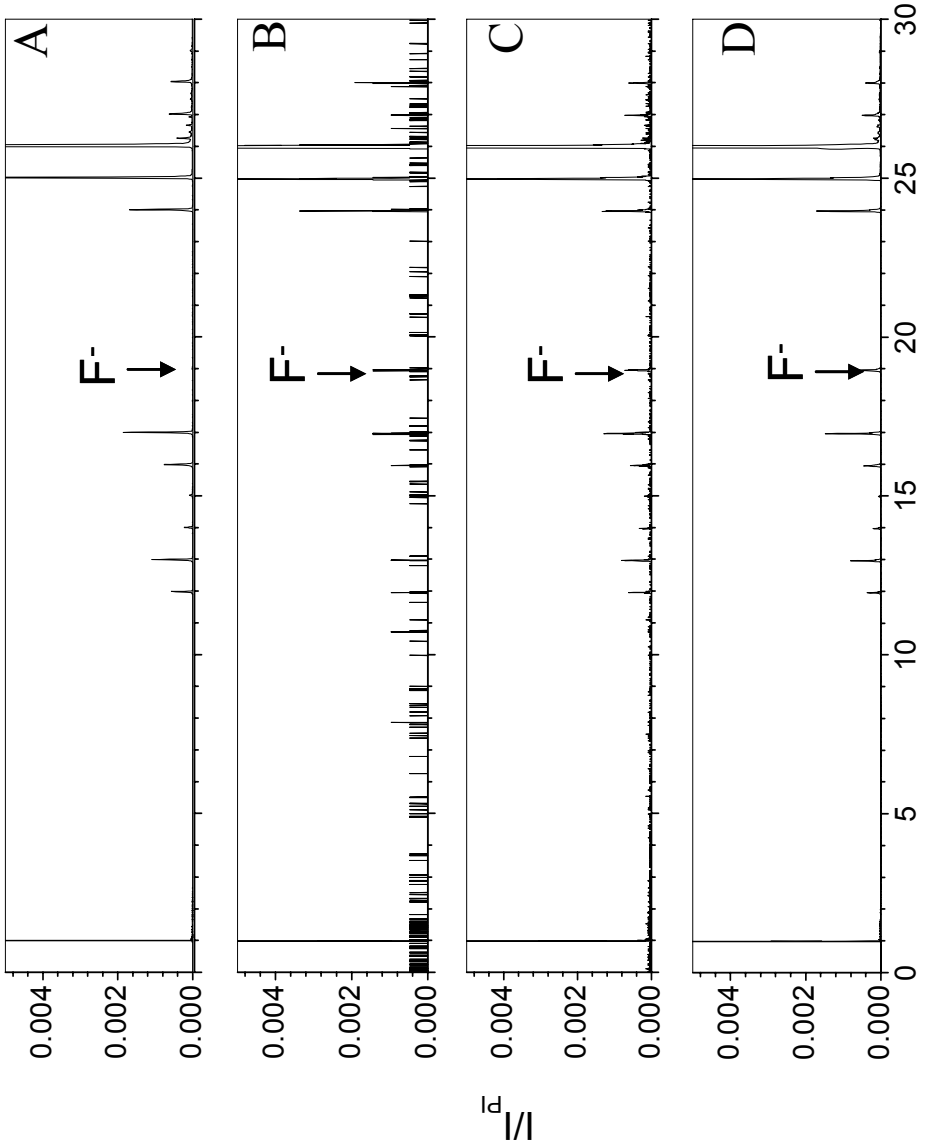

Figure 8-2: Negative secondary ion ToF spectra produced by 26 keV projectile bombardment on vapor deposited glycine samples (A) ~3.3 million C_{60}^+ projectiles, (B) 2080 $C_{60}F_{40}^+$ projectiles, (C) 20984 $C_{60}F_{40}^+$ projectiles, (D) ~2.1 million $C_{60}F_{40}^+$ projectiles

not generally associated with the clusters as m/z 19 in negligible in the 26 keV C_{60}^{+} spectrum.

Before going further, two terms must be defined. Backscattered ions are projectile constituents that are re-emitted on the time-scale of a desorption event with minimal interaction with the surface which results in the retention of a portion of the initial kinetic energy. Prompt ions are projectile constituents that are re-emitted on the time-scale of a desorption event, but the initial kinetic energy of the constituent is deposited into the surface before the ion is ejected.

Figures 8-3 shows the normalized F^- peaks from four targets: Gly, Cu, Ag, and Au. The F^- peaks exhibit characteristics of prompt and backscattered ions. A high energy tail occurs in the F^- peak from targets of Cu, Ag, and Au. The high energy tail indicates conservation of part of the incident energy which suggests a backscattering process.

The F^- peak from a Gly target is approximately symmetric with a negligible high energy tail relative to the F^- peaks from targets of Cu, Ag, and Au. This suggests prompt emission of the F^- from Gly with negligible contribution from backscattering. MD simulations have shown the ejection of fewer projectiles constituents in instances the projectile atoms have the same mass as the target atoms [122].

The proportion of backscattered F^- to prompt F^- varies depending on the atomic mass of the target. Backscattering increases with the atomic mass of the target which is indicated by the increased area under the high energy tail of F^- from targets of Gly, Cu,

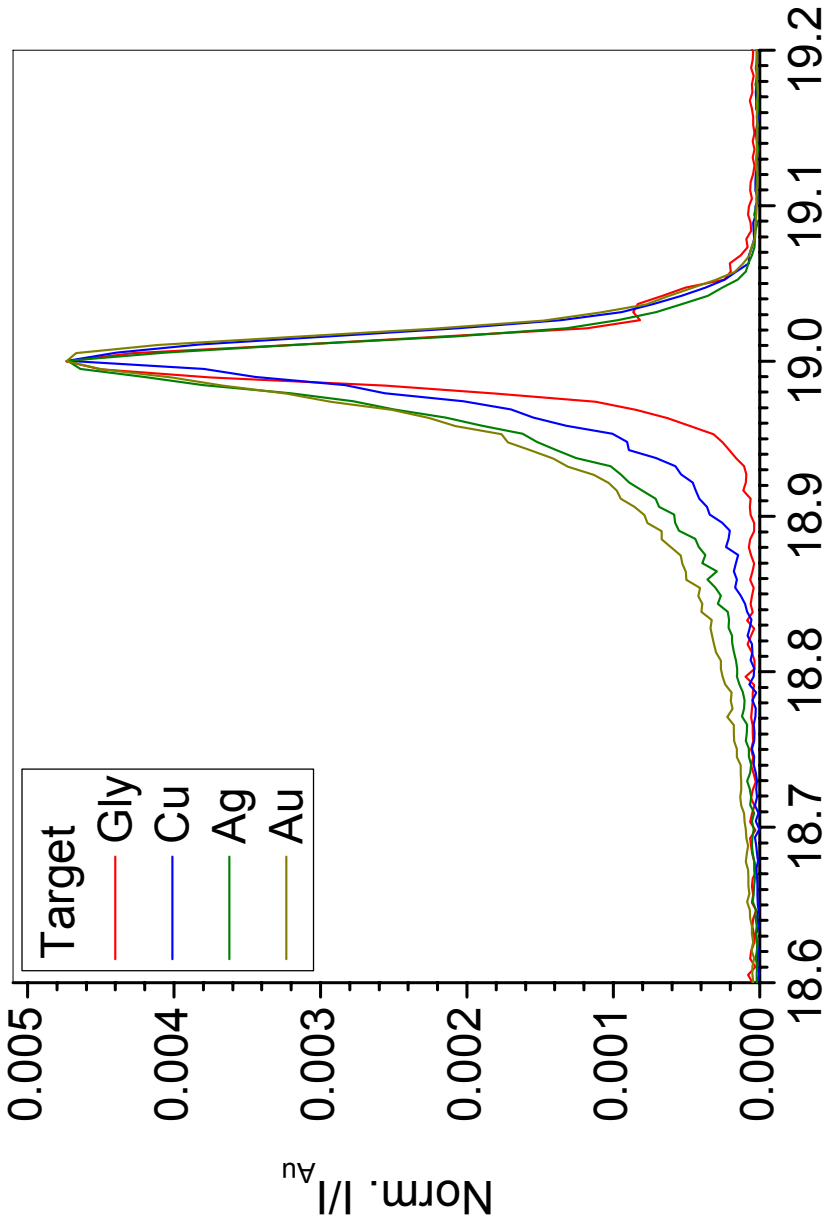

Figure 8-3: An overlay of the F^- regions from various targets produced by 26 keV $C_{60}F_{40}^+$ impacts (all intensities are normalized to F^- from Au).

Ag, and Au (Fig 8-3). A significant portion of the backscattered F^- may not be detected because the radial velocities of the F- ions move the ions out of the detection path.

Figure 8-4 shows the yield of F^-_{total} (backscattered and prompt) as a function of the average target atom weight. Average target atom weight is the atomic weight for homonuclear targets. For heteronuclear targets, it is the weighted average of the individual atomic weights based on the stoichiometry of the target. For example, heteronuclear species, BN, is composed of B (10.811 amu) and N (14.007 amu). Given a 1:1 atomic ratio, the average target atom mass for this target is 12.409 amu. The yield of F^-_{total} increases linearly as the atomic weight of the target atoms increases. A formal deconvolution of the backscattered and prompt emission signals was not performed in this initial study. However, deconvolution of the signals may provide additional insight into fundamental aspects of the desorption process.

The yield of F^- as a function of impact energy from glycine targets is shown in Figure 8-5. The yield of F^- is constant within the energy range examined (14-26 keV). It is expected that a threshold energy exists at which re-emission ceases. However, the instrumental setup did not allow further investigation at lower energies.

As previously mentioned, an adduct series of the nature Au_nX^- (n= 1-17, X = components of the sample such as CN) were observed under Au_n^m (n = 100-400, m = 4) bombardment. Previous studies with smaller clusters also suggested that an adduct series may occur, but an adduct series was not verified due to

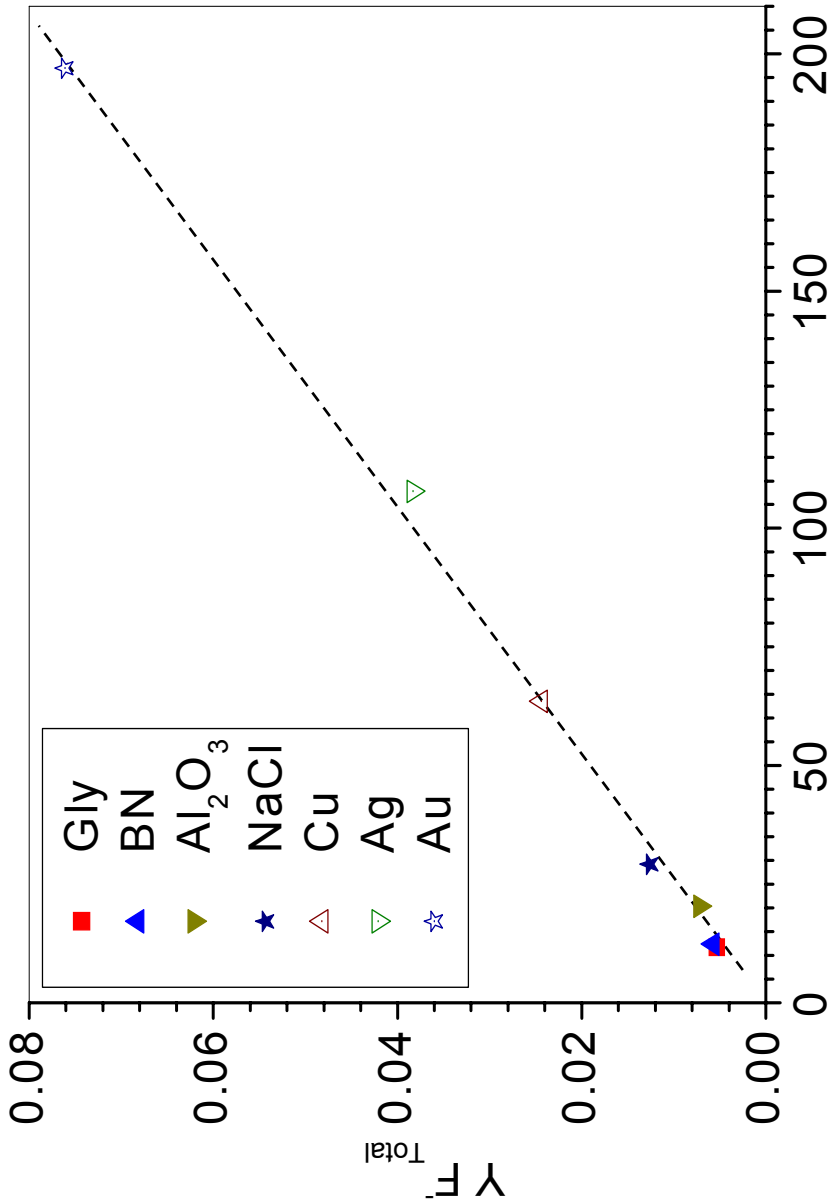

Figure 8-4: The yield of F^- (backscattered and prompt-emission) from 26 keV $C_{60}F_{40}^+$ impacts as a function of the average target atom weight (dashed line is to guide the eye).

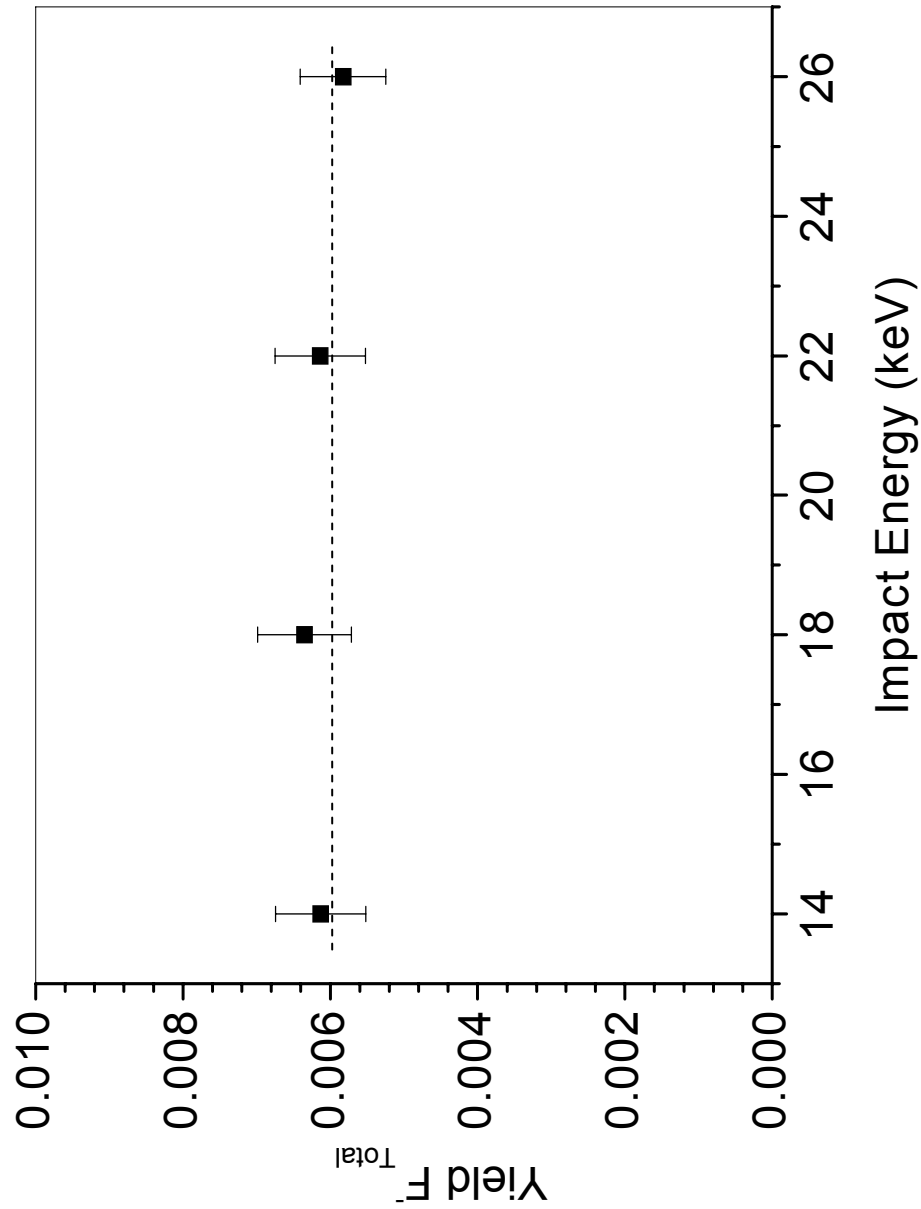

Figure 8-5: The yield of F^- (backscattered and prompt-emission) from a glycine target produced by $C_{60}F_{40}^+$ impacts at various impact energies (dashed line is to guide the eye).

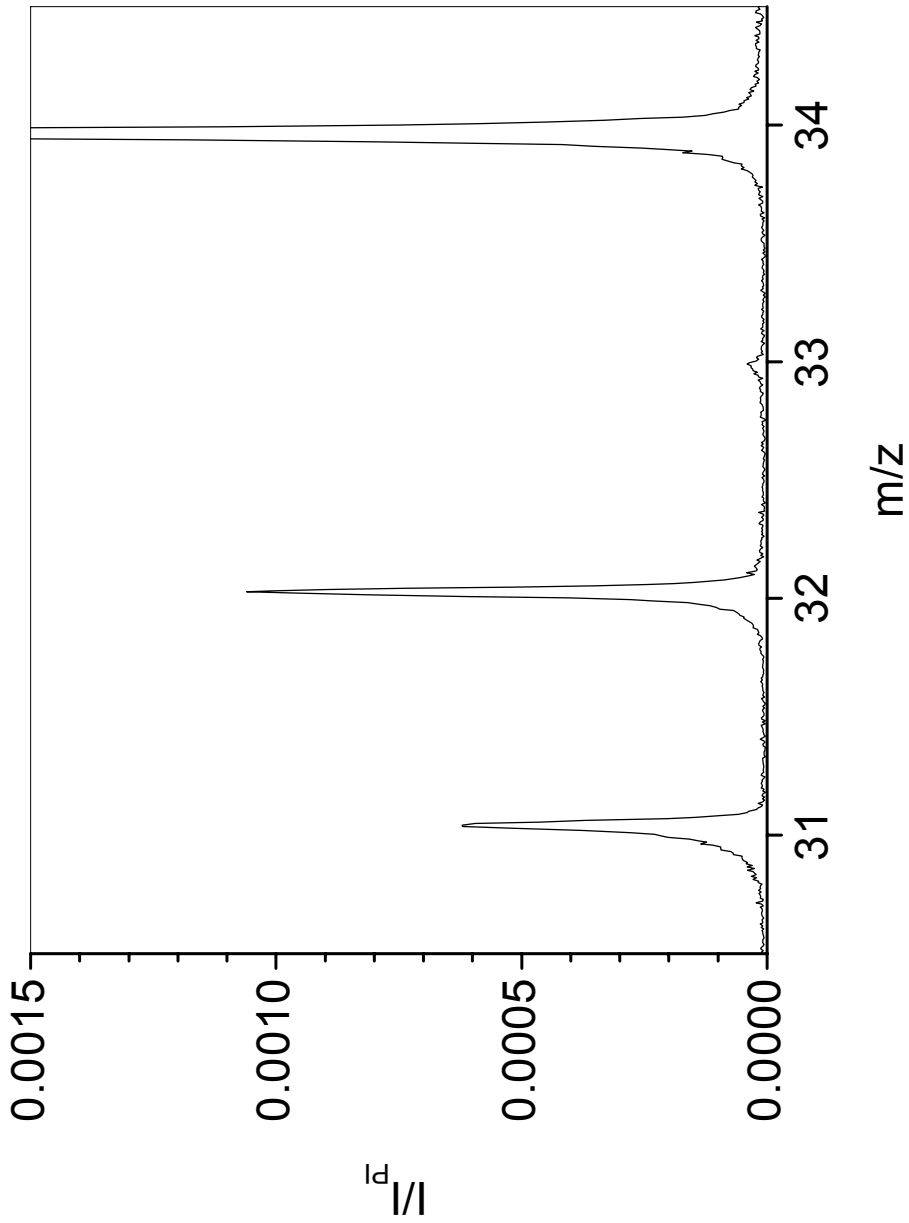

Figure 8-6: The region m/z 30 to m/z 43 produced by 26 keV $C_{60}F_{40}^{+}$ impacts on a Au target.

interferences [50]. Since $C_{60}F_{40}^{+}$ projectile contains a similar number of constituents to the aforementioned Au clusters, targets of Gly, BN, Al_2O_3, NaCl,
Cu, Ag and Au were bombarded by 26 keV $C_{60}F_{40}^{+}$ and examined for an adduct series in the form XF^{-}. Definitive identification of an adduct series was not achieved. However, the peak at m/z 31 emitted from a Au target has a high energy tail similar to that of F^{-} suggesting the adduct, CF^{-}, may be formed (Fig. 8-6).

The absence of an adduct series under $C_{60}F_{40}^{+}$ bombardment compared to the abundant adduct series produced by Au_n^{m} (n = 100-400, m = 4) may be the result of the electron affinities of fluorine (328 kJ/mol) and Au (222.8 kJ/mol) [124]. The higher electron affinity of fluorine may cause preferential acceptance of electrons rather than components of the sample as is seen with Au. If this is the case, a fluorine adduct series (i.e., XF^{+}) may occur in the positive mode. The fluorine atoms may form chemical bonds to accept an electron since free electrons are less likely to be available in positive mode compared to negative mode.

CHAPTER IX

CONCLUSIONS

The purpose of this research was to examine fundamental aspects of carbon cluster-solid interactions relevant to surface analysis. Three goals were set: (1) design and construct an effusion-based primary source capable of producing various carbon cluster projectiles, (2) evaluate secondary ion emission from various surfaces under carbon cluster bombardment, and (3) explore sample preparation to increase molecular ion yields under cluster bombardment.

The effusion-based primary source built for this project has two major advantages over the ^{252}Cf system previously used for carbon cluster production. The duty cycle of the ^{252}Cf system decreases over time because of radioactive decay. The effusion-based system produces primary ions via electron impact from a hot filament. Therefore, when the duty cycle decreases because of filament contamination, installation of a new filament will restore the system to its original state. The ^{252}Cf system allowed a variety of primary ions to impact a sample. The secondary ions emitted from a primary ion of interest were then extracted from the data set. The effusion-based system pre-selects the primary ions so that only one species of primary ion (e.g., C_{60}^+, $C_{60}F_{40}^+$, etc.) impacts the surface. Primary ion selection increases the duty cycle by removing SI emission from superfluous projectiles.

Multiple ion emission from 26 keV $C_{24}H_{12}^+$, C_{60}^+ and $C_{60}F_{40}^+$ projectiles is similar and varies with impact energy such that higher energies produce more multiple

ion emission. Multiple ion emission of sample representative ions (i.e., CN^- and $[M-H]^-$) have a monotonic decrease as a function of the number of secondary ion emitted per impact, which is similar to the total ion emission trend. Comparisons of Au^+ projectiles to $C_{24}H_{12}^+$, C_{60}^+ and $C_{60}F_{40}^+$ projectiles at equal impact energies show the atomic and cluster projectiles to be equally efficient at producing single ion emission, but clusters are 3-4 times more efficient at producing multiple ion emission compared to Au^+.

Multiple ion emission has been examined as a function of projectile characteristics and as a function of the number of ions emitted per event with $C_{24}H_{12}^+$, C_{60}^+ and gramicidin S^+ projectiles. Supralinear yield enhancements are found in the emission of two Phe $[M-H]^-$ per impact as a function of projectile velocity, which differs from linear increases found in the Phe $[M-H]^-$ yield with respect to projectile velocity. Increased multiple secondary ion emission under carbon cluster bombardment has potential to improve the efficiency of coincidental ion mass spectrometry.

Backscattered F^- and promptly-emitted F^- are present in the mass spectra of the samples bombarded with the $C_{60}F_{40}^+$ projectile. The yield of F^- (backscattered and prompt) increases linearly as the atomic weight of the target atoms increases. A possible fluorine adduct (CF^-) was also found when bombarding a Au target with 26 keV $C_{60}F_{40}^+$ projectiles.

CN^- emission from organic and biological samples as a function of carbon-based projectile characteristics was examined to explore the possibility of using CN^- as a molecular identifier. The yield of CN^- is found to range between ~14-28% in the samples examined, while the corresponding $[M-H]^-$ yields range between ~0.05 - 17%

and decrease with increasing molecular weight. For gramicidin S (M.W. 1141), the yield of CN^- is ~10^2 higher than the gramicidin S $[M-H]^-$ yield. The emission of CN^- is found to be dependent on the availability of nitrogen and carbon in the desorption volume.

The type of CN^- emission (i.e., direct or recombination/rearrangement) was also examined. The CN^- recombination is primarily dependent on the number of constituents in the projectile and weakly dependent on impact energy. The recombination rate reaches plateaus for all projectiles examined with the maximum recombination rates of ~22%, ~32%, and ~31% for 26 keV $C_{24}H_{12}^+$, C_{60}^+ and $C_{60}F_{40}^+$, respectively.

We have demonstrated that the emission of the gramicidin S [M-H]- ion is enhanced by embedding gramicidin S in a matrix of sinapic acid with the yield of gramicidin S $[M-H]^-$ being maximized at a matrix-to-analyte ratio of 10:1. An encapsulation model is used to explain the experimental results. In this model, the matrix increases the gramicidin S $[M-H]^-$ production by cooling gramicidin S $[M-H]^-$ in the gas phase via evaporation of attached matrix molecules [33, 35]. Additionally, CN^- emission is found to occur independent of matrix effects from mixtures of gramicidin S and sinapic acid.

Further studies in the area of carbon cluster bombardment should include instrumentation modifications resulting in the consistent production of multi-charged primary projectiles such as C_{60}^{2+} and C_{60}^{3+}. The production of these ions would increase impact energy of the system 2-3 times with low applied voltages (i.e. 5-20 keV). To accommodate the expected increase in SI production with impact energies in the range

of 25-90 keV, the SI detection scheme should be updated to include pulse amplitude analysis in conjunction with multiple anodes. The 8 anode detector can detect multiple ions of the same m/z if those ions impact different anodes; however, if multiple ions of the same m/z impact the same anode, signal is lost. The pulse amplitude from each anode could be correlated to the number of ions responsible for the signal thereby reducing signal loss.

MD simulations and experiments show crater depths of ~2.5-5 nm in the energy range of these experiments (14-26 keV) [14, 125]. However, the depth of secondary ion emission under carbon cluster bombardment has not been experimentally determined and is therefore a matter of conjecture.

The fundamental nature of matrix enhancement in the negative mode needs to be examined. In the positive mode, matrix increases ionization efficiency by providing H^+ and evaporative cooling to the analyte [33, 35]. The influence of the matrix on negative mode ionization is unclear since a de-protonation process occurs. Additionally, the type of matrices used for ME-SIMS should be examined. Conjugated organic acids, similar to those used in matrix-assisted laser desorption/ionization (MALDI) experiments, are regularly used as matrices in ME-SIMS experiments. However, the UV absorption of a matrix should not be a fundamental limitation for SIMS analysis. Therefore, a larger, potentially more efficient set of matrices may be available for ME-SIMS.

The use of $C_{60}F_{40}^+$ as a projectile in the positive mode needs to be examined. The $C_{60}F_{40}^+$ projectile should increase secondary ion emission since it is a large cluster projectile. Additionally, the introduction of forty electronegative fluorine atoms to

desorption volume may enhance the ionization probability in the positive mode. Studies have shown increased secondary ion emission in the positive mode when the sample was bombarded with electronegative projectiles such as O_2^+ [108-110].

REFERENCES

1. L. Gavioli, M. Padovani, E. Spiller, M. Sancrotti, M.G. Betti, Appl. Surf. Sci. 212-213 (2003) 47.

2. T. Terasawa, K. Akimoto, Y. Mizuno, A. Ichimiya, K. Sumitani, T. Takahashi, X.W. Zhang, H. Sugiyama, H. Kawata, T. Nabatame, A. Toriumi, Appl. Surf. Sci. 244 (2005) 16.

3. C. Ha, J.A. Gardella Jr., Chem. Rev. 105 (2005) 4205.

4. S. Chandra, Appl. Surf. Sci. 231-232 (2004) 462.

5. Y. Lee, S. Han, M. Kwon, Appl. Surf. Sci. 231-232 (2004) 278.

6. F. Kollmer, Appl. Surf. Sci. 231-232 (2004) 153.

7. A.P. Nair, B.J. Tyler, R.E. Peterson, Appl. Surf. Sci. 231-232 (2004) 538.

8. L. Sangely, M. Chaussidon, R. Michels, V. Huault, Appl. Surf. Sci. 231-232 (2004) 179.

9. A. Brunelle, S. Della-Negra, C. Deprun, J. Depauw, P. Håkansson, D. Jacquet, Y. Le Beyec, M. Pautrat, Int. J. Mass Spectrom. Ion Process. 164 (1997) 193.

10. A. Benninghoven, F. Rudenauer, H. Werner, Secondary Ion Mass Spectrometry, Wiley & Sons, New York, 1987.

11. G. Gillen, S. Roberson, Rap. Comm. Mass Spectrom. 12 (1998) 1303.

12. C. Szakal, S. Sun, A. Wucher, N. Winograd, Appl. Surf. Sci. 231-232 (2004) 183.

13. J. Cheng, N. Winograd, Anal. Chem. 77 (2005) 3651.

14. Z. Postawa, B. Czerwinski, M. Szewczyk, E.J. Smiley, N. Winograd, B.J. Garrison, Anal. Chem. 75 (2003) 4402.

15. N. Winograd, J.P. Baxter, F.M. Kimock, Chem. Phys. Lett. 88 (1982) 581.

16. J.B. Pallix, C.H. Becker, K.T. Gillen, Appl. Surf. Sci. 32 (1988) 1.

17. C.H. Becker, S.G. MacKay, D.G. Welkie, J. Vac. Sci. Technol. B 10 (1992) 380.

18. M. Wood, Y. Zhou, C.L. Brummel, N. Winograd, Anal. Chem. 66 (1994) 2425.

19. L.A. Currie, Anal. Chem. 40 (1968) 586.

20. M.G. Blain, S. Della-Negra, J. Joret, Y. Le Beyec, E.A. Schweikert, Phys. Rev. Let. 63 (1989) 1625.

21. D.E. Weibel, N. Lockyer, J.C. Vickerman, Appl. Surf. Sci. 231-232 (2004) 146.

22. A.G. Sostarecz, S. Sun, C. Szakal, A. Wucher, N. Winograd, Appl. Surf. Sci. 231-232 (2004) 1179.

23. A.G. Sostarecz, C.M. McQuaw, A. Wucher, N. Winograd, Anal. Chem. 76 (2004) 6651.

24. S. Sun, A. Wucher, C. Szakal, N. Winograd, Appl. Phy. Lett. 84 (2004) 5177.

25. A. Wucher, S. Sun, C. Szakal, N. Winograd, Anal. Chem. 76 (2004) 7234.

26. A. Wucher, S. Sun, C. Szakal, N. Winograd, Appl. Surf. Sci. 231-232 (2004) 68.

27. J. Xu, C.W. Szakal, S.E. Martin, B.R. Peterson, A. Wucher, N. Winograd, J. Am. Chem. Soc. 126 (2004) 3902.

28. J. Xu, S. Ostrowski, C.W. Szakal, A.G. Ewing, N. Winograd, Appl. Surf. Sci. 231-232 (2004) 159.

29. S. Parry, N. Winograd, Anal. Chem. 77 (2005) 7950.

30. S.G. Ostrowski, C.Szakal, J. Kozole, T.P. Roddy, J. Xu, A.G. Ewing, N. Winograd, Anal. Chem. 77 (2005) 6190.

31. Z. Postawa, B. Czerwinski, M. Szewczyk, E.J. Smiley, N. Winograd, B.J. Garrison, J. Phys. Chem. 108 (2004) 7831.

32. T. Aoki, T. Seki, J. Matsuo, Z. Insepov, I. Yamada, Mat. Chem. Phys. 54 (1998) 139.

33. H. Grade, R.G. Cooks, J. Am. Chem. Soc. 100 (1978) 5615.

34. A. Delcorte, P. Bertrand, Anal. Chem. 77 (2005) 2107.

35. R.G. Cooks, K.L. Busch, Int. J. Mass Spectrom. Ion Phy. 53 (1983) 111.

36. K.L. Busch, B.H. Hsu, Y.X. Xie, R.G.Cooks, Anal. Chem. 55 (1983) 1157.

37. S. Bouchonnet, Y. Hoppilliard, C. Mauriac, Int. J. Mass Spectrom. Ion Process. 126 (1993) 163.

38. K.J. Wu, R.W. Odom, Anal. Chem. 68 (1996) 873.

39. J.F. Blankenship, M.J. Van Stipdonk, E.A. Schweikert, Rap. Comm. Mass Spectrom. 11 (1997) 143.

40. K. Wittmaack, W. Szymczak, G. Hoheisel, W. Tuszynski, J. Am. Soc. Mass Spectrom. 11 (2000) 553.

41. S.L. Luxembourg, L.A. Mcdonnell, M.C. Duursma, X. Guo, R.M.A. Heeren, Anal. Chem. 75 (2003) 2333.

42. T. Schenkel, K.J. Wu, Int. J. Mass Spectom. 229 (2003) 47.

43. S.L. McArthur, M.C. Vendettuoli, B.D. Ratner, D.G. Castner, Langmuir 20 (2004) 3704.

44. L. Adriaensen, F. Vangaever, J. Lenaerts, R. Gijbels, Rap. Comm. Mass Spectrom. 19 (2005) 1017.

45. M.A. Park, K.A. Gibson, L. Quinones, E.A. Schweikert, Science 248 (1990) 988.

46. B.D. Cox, M.A. Park, R.G. Kaercher, E.A. Schweikert, Anal. Chem. 64 (1992) 843.

47. R.D. Rickman, S.V. Verkhoturov, S. Balderas, N. Bestaoui, A. Clearfield, E.A. Schweikert, Appl. Surf. Sci. 231-232 (2004) 106.

48. S.V. Verkhoturov, E.A. Schweikert, Anal. Bioanal. Chem. 373 (2002) 609.

49. R.D. Rickman, S.V. Verkhoturov, E.S. Parilis, E.A. Schweikert, Phys. Rev. Lett. 92 (2004) 047601.

50. A. Brunelle, S. Della-Negra, Y. Le Beyec, Nucl. Instrum. Meth. B 132 (1997) 718.

51. I.S. Bitensky, E.S. Parilis, I.A. Wojciechowski, Nucl. Instrum. Meth. B 67 (1992) 359.

52. C. Guillermier, S.V. Verkhoturov, G.J. Hager, R.D. Rickman, S. Della-Negra, E.A. Schweikert, to be submitted J. Chem. Phys. 2006.

53. Z. Postawa, B. Czerwinski, N. Wiongrad, B.J. Garrison, J. Phys. Chem. 109 (2005) 11973.

54. P.K. Pol, J.M. Fluit, J. Kistemaker, Physica 26 (1960) 1000.

55. F. Grønlund, W.J. Moore, J. Chem. Phys. 32 (1960) 1540.

56. H.H. Andersen, H.L. Bay, J. Appl. Phys. 45 (1974) 953.

57. H.H. Andersen, H.L. Bay, J. Appl. Phys. 46 (1975) 2416.

58. S.S. Johar, D.A. Thompson, Surf. Sci. 90 (1979) 319.

59. A.D. Appelhans, J.E. Delmore, D.A. Dahl, Anal. Chem. 59 (1987) 1685.

60. A.D. Appelhans, J.E. Delmore, Anal. Chem. 61 (1989) 1087.

61. M. Benguerba, A. Brunelle, S. Della-Negra, J. Depauw, H. Joret, Y. Le Beyec, M.G. Blain, E.A. Schweikert, G. Ben Assayag, P. Sudraud, Nucl. Instrum. Meth. B 62 (1991) 8.

62. K. Boussofiane-Baudin, G. Bolback, A. Brunelle, S. Della-Negra, P. Håkansson, Y. Le Beyec, Nucl. Instrum. Meth. B 88 (1994) 160.

63. W. Szymczak, K. Wittmaack, Nato ASI Series, Series B: Physics 269 (1991) 123.

64. M.J. Van Stipdonk, R.D. Harris, E.A. Schweikert, Rap. Comm. Mass Spectrom. 10 (1996) 1987.

65. C.W. Diehnelt, M.J. Van Stipdonk, E.A. Schweikert, Int. J. Mass Spectrom. 207 (2001) 111.

66. M.J. Van Stipdonk, V. Santiago, E.A. Schweikert, J. Mass Spectrom. 34 (1999) 554.

67. R.D. Harris, W.S. Baker, M.J. Van Stipdonk, R.M. Crooks, E.A. Schweikert, Rap. Comm. Mass Spectrom. 13 (1999) 1374.

68. M.J. Van Stipdonk, R.D. English, E.A. Schweikert, J. Phys. Chem. B 103 (1999) 7929.

69. M.J. Van Stipdonk, R.D. English, E.A. Schweikert, Anal. Chem. 72 (2000) 2618.

70. R.D. English, M.J. Van Stipdonk, E.A. Schweikert, Int. J. Mass Spectrom. 209 (2001) 113.

71. G. Gillen, L. King, B. Freibaum, R. Lareau, J. Bennett, F. Chmara, J. Vac. Sci. Technol. A 19 (2001) 568.

72. S.C.C. Wong, R. Hill, P. Blenkinsopp, N.P. Lockyer, D.E. Weibel, J.C. Vickerman, Appl. Surf. Sci. 203-204 (2003) 219.

73. J.F. Mahoney, J. Perel, T.D. Lee, P.A. Martino, P. William, J. Am. Soc. Mass Spectrom. 3 (1992) 311.

74. J.F. Mahoney, E.A. Parilis, T.D. Lee, Nucl. Instrum. Meth. B 88 (1994) 154.

75. R.A. Zubarev, I.S. Bitensky, P.A. Demirev, B.U.R. Sundquist, Nucl. Instrum. Meth. B 88 (1994) 143.

76. J. Axelsson, C.T. Reimann, B.U.R. Sundquist, Nucl. Instrum. Meth. B 88 (1994) 131.

77. C.T. Reimann, A.P. Quist, J. Kopniczky, B.U.R. Sundquist, R. Erlandsson, P. Tengvall, Nucl. Instrum. Meth. B 88 (1994) 29.

78. I. Yamada, Nucl. Instrum. Meth. B 112 (1996) 242.

79. S. Bouneau, S. Della-Negra, J. Depauw, D. Jacquet, Y. Le Beyec, J.P. Mouffron, A. Novikov, M. Pautrat, Nucl. Instrum. Meth. B 225 (2004) 579.

80. A. Tempez, J.A. Schultz, S. Della-Negra, J. Depauw, D Jacquet, A. Novikov, Y. Le Beyec, M. Pautrat, M. Caroff, M. Ugarov, H Bensaoula, M. Gonin, K. Fufrer, A. Woods, Rap. Comm. Mass Spectrom. 18 (2004) 371.

81. A. Novikov, M. Caroff, S. Della-Negra, J. Depauw, M. Fallavier, Y. Le Beyec, M. Pautrat, J.A. Schultz, A. Tempez, A.S. Woods, Rap. Comm. Mass Spectrom. 19 (2005) 1851.

82. P. Sigmund, Phy. Rev. 184 (1969) 184.

83. P. Sigmund, Appl. Phys. Lett. 3 (1974) 169.

84. P. Sigmund, C. Claussen, J. Appl. Phys. 52 (1981) 990.

85. I.S. Bitensky, E.S. Parilis, Nucl. Instrum. Meth. B 21 (1987) 26.

86. R. Zaric, B. Pearson, K.D. Krantzman, B.J. Garrison, Int. J. Mass Spectrom. Ion Process. 174 (1998) 155.

87. R. Webb, M. Kerford, E. Ali, M. Dunn, L. Knowles, K. Lee, J. Mistry, F. Whitefoot, Surf. Interface Anal. 31 (2001) 297.

88. R. Webb, M. Kerford, A. Way, I. Wilson, Nucl. Instrum. Meth. B 153 (1999) 284.

89. A. Delcorte, Phys. Chem. Chem. Phys. 7 (2005) 3395.

90. S.V. Verkhoturov, E.A. Schweikert, N.M. Rizkalla, Langmuir 18 (2002) 8836.

91. R.D. Rickman, S.V. Verkhoturov, G.J. Hager, E.A. Schweikert, J.A. Bennett, Int. J. Mass Spectrom. 241 (2005) 57.

92. R.D. Rickman, S.V. Verkhoturov, G.J. Hager, E.A. Schweikert, Int. J. Mass Spectrom. 245 (2005) 48.

93. R.D. MacFarlane, Anal. Chem. 55 (1983) 1247A.

94. R. Sundquvist, R.D. MacFarlane, Mass Spectrom. Rev. 4 (1985) 421.

95. P. Scheier, B. Dunser, R Wörgötter, M. Lezius, R. Robl, T.D. Mark, Int. J. Mass Spectrm. Ion Process. 138 (1994) 77.

96. M. Sai Baba, T.S. Lakshmi Narasimhan, R. Balasubramanian, C.K. Mathews, Int. J. Mass Spectrom. Ion Process. 130 (1994) L1.

97. T. Hattori, N. Hayashizaki, S. Matsui, H. Tomizawa, T. Yoshida, S.J. Gates, K. Sasa, S. Majima, K. Isokawa, T. Ito, M. Okamura, S. Yamda, Rev. Sci. Instrum. 71 (2000) 1049.

98. J.H. Moore, C.C. Davis, M.A. Coplan, Building Scientific Apparatus: A Practical Guide to Design and Construction 2nd Ed., Perseus Books, Cambridge, Massachusetts 1991.

99. M. Guilhaus, J. Mass Spectrom. 30 (1995) 1532.

100. J.L. Wiza, Nucl. Instr. Meth. 162 (1979) 587.

101. I.S. Gilmore, M.P. Seah, Int. J. Mass Spectrom. 202 (2000) 217.

102. G.J. Hager, Secondary Ion Emission from Massive Gold Cluster Impacts, Diss. TAMU, 2006.

103. R.D. Rickman, Secondary Ion Emission from "Super-Efficient Events: Prospects for Surface Mass Spectrometry", Diss. TAMU, 2004.

104. I.S. Bitensky, D.F. Baroofsky, Phys. Rev. B 56 (1997) 13815, and references therein.

105. P. Sigmund, I.S. Bitensky, J. Jenson, Nucl. Instrum. Meth. B 112 (1996) 1.

106. C.W. Diehnelt, M.J. Van Stipdonk, E.A. Schweikert, Nucl. Instrum. Meth. B 88 (1998) 606.

107. L. Hanley, O. Kornienko, E.T. Ada, E. Fuoco, J.L. Trevor, J. Mass Spectrom. 34 (1999) 705.

108. P. Williams, C.A. Evans Jr., Surf. Sci. 78 (1978) 324.

109. K. Wittmaack, Surf. Sci. 112 (1981) 168.

110. H. Gnaser, Surf. Sci. 138 (1984) 561.

111. C. Guillermier, personal communication, Texas A&M University, 2005.

112. J.L. Guerquin-Kern, M. Coppey, D. Carrez, A.C. Brunet, C.H. Nguyen, C. Rivalle, G. Slodzian, A. Croisy, Micro. Res. Tech. 36 (1997) 287.

113. R. Peteranderl, C. Lechene, J. Am. Soc. Mass Spectrom. 15 (2004) 478.

114. A.M. Kleinfeld, J.P. Kampf, C. Lechene, J. Am. Soc. Mass Spectrom. 15 (2004) 1572.

115. J.M. Chabala, K.K. Soni, J. Li, K.L. Gavrilov, R. Levi-Setti, Int. J. Mass Spectrom. Ion Process. 143 (1995) 191.

116. National Institute for Standards and Technology, URL: http://webbook.nist.gov/, accessed April, 2006.

117. J.A. Taylor, J.W. Rabalais, Surf. Sci. 74 (1978) 229.

118. C. Guillermier, E.A. Schweikert, to be submitted Phys. Rev. Lett. 2006.

119. S. Chandra, Euro. J. Cell Biol. 84 (2005) 783.

120. M. Barber, R.S. Bordoli, G.J. Elliott, R.D. Sedgwick, A.N. Tyler, Anal. Chem. 54 (1982) 645A.

121. A.M. Childs, M.H. Shapiro, T.A. Tombrello, Nucl. Instrum. Meth. B 143 (1998) 298.

122. M.H. Shapiro, T.A. Tombrello, Nucl. Instrum. Meth. B 58 (1991) 161.

123. G.J. Hager, C. Guillermier, S.V. Verkhoturov, E.A. Schweikert, Appl. Surf. Sci. in press, 2006.

124. Webelements Ltd, UK. URL: http://www.webelements.com/webelements/ elements/text/periodic-table/ionz.html, accessed April 2006.

125. T. Seki, T. Aoki, M. Tanomura, J. Matsuo, I. Yamada, Mater. Chem. Phys. 54 (1998) 143.

VITA

Name:	Jay Edward Locklear
Address:	$^{C}/_{O}$ Professor Emile A. Schweikert Center for Chemical Characterization and Analysis, Mail Stop 3144 TAMU, College Station, TX 77843-3144
Email:	Jay_Locklear@yahoo.com
Education:	B.S., Chemistry, Southwestern Oklahoma State University, 2000 PhD., Chemistry, Texas A&M University, 2006